MAGNETIC THIN FILMS WITH HIGH PERPENDICULAR ANISOTROPY FOR MAGNETIC RECORDING MEDIA APPLICATIONS

A DISSERTATION
SUBMITTED TO THE FACULTY OF THE GRADUATE SCHOOL
OF THE UNIVERSITY OF MINNESOTA
BY

HAIBAO ZHAO

IN PARTIAL FULFILLMENT OF THE REQUIREMENTS
FOR THE DEGREE OF
DOCTOR OF PHILOSOPHY

JIAN-PING WANG, ADVISOR

Aug, 2014

Acknowledgements

I would like to take this opportunity to thank those people who supported and helped me throughout my Ph.D. study at the University of Minnesota. First and foremost, I would like to thank my advisor, Professor Jian-Ping Wang, for his guidance, care, and patience on my thesis projects and thesis writing.

I appreciate various support from the professors of the Center for Micromagnetic and Information Technologies (MINT), including Randall Victora, Beth Stadler, Chris Leighton, and Jack Judy. During my work and stay in the department of Electrical Engineering, I received generous help from them through course studies, Journal Club activities, kind permissions for the use of their lab equipments, etc.

This thesis work was partially supported by Western Digital (on ECC FePt thin film projects), and Seagate Technology and Information Storage Industry Consortium Extremely High Density Recording (EHDR) Program (on $SmCo_5$ thin film projects). I thank the useful discussions with Dr. Hua Yuan from Western Digital and Dr. Chengjun Sun from Argonne National Lab. Parts of the thesis work were carried out in the Characterization Facility, which receives partial support from NSF through the NSF Minnesota MRSEC Program under Award Number DMR-0819885 and NNIN program. Especially I would like to thank Dr. Ozan Ugurlu (Charfac) for his support on HRTEM EDS and HAADF analysis.

It has been a memorable experience with the past and current members in Professor Wang's research group, including but not limited to Dr. Xiaoqi Liu, Dr. Hao Wang, Dr. Bin Ma, Dr. Jingzhi Han, Dr. Weikang Shen, Dr. Jiaoming Qiu, Dr. Yunhao Xu, Dr. Xiaofeng Yao, Dr. Jianmin Bai, Mr. Shaoqian Yin, Ms. Meiyin Yang, and Mr. Xuan Li. I sincerely thank them for their valuable discussions and collaborations with me.

Dedication

With gratitude to my family:
Mom, Jing, Cindy, and Sara.

Abstract

In order to meet the basic thermal stability requirement in future extremely high density magnetic recording, magnetic materials with high magnetocrystalline anisotropy constant (Ku) are needed. In this thesis work, the two most-promising candidates of high Ku materials, i.e. $CaCu_5$-type $Sm(Co, Cu)_5$ and $L1_0$-type FePt thin films, have been systematically studied.

$SmCo_5$ has the highest Ku among practical magnetic materials. Prior studies on $SmCo_5$-based thin films for magnetic recording media applications is reviewed. $SmCo_5$ thin films with good perpendicular magnetic anisotropy were only grown on Cu underlayer. However, the uncontrollable Cu diffusion from the Cu underlayer and the relatively large Cu grain size make it not suitable for magnetic recording applications. In this study, polycrystalline Sm–Co–Cu films consisting mainly of highly (0001) textured $Sm(Co, Cu)_5$ grains have been successfully fabricated on non-Cu containing underlayers (Ru or Ru(Cr)) on glass substrates. Strong perpendicular magnetic anisotropy of $Sm(Co, Cu)_5$ thin films was achieved. It was found that increasing Cu is like increasing deposition temperature - both could improve the $SmCo_5$ phase formation and the crystallinity of $Sm(Co, Cu)_5$ (0001) films. The median composition of nanocrystalline $Sm(Co, Cu)_5$ grains estimated from structural unit volume and Curie temperature matches reasonably well with each other. In-plane compressive strain in $Sm(Co, Cu)_5$ films is inferred from the differences of lattice constants between the thin film and bulk material. The use of Ru(Cr) underlayer with a proper Cr doping could improve the perpendicular anisotropy of $Sm(Co, Cu)_5$ films.

Microstructure of $Sm(Co, Cu)_5$ thin films was studied using SEM, AFM, and TEM analysis. The grain size of Ru underlayer is about 10-30 nm, much smaller than that of Cu underlayer (~200 nm) reported in the literature. Magnetization reversal in $Sm(Co, Cu)_5$ thin films is dominated by the domain wall pinning mechanism. Many types of pinning sites are found: voids, grain/matrix boundaries (or crystalline/amorphous boundaries), grain boundaries between crystalline grains, and the composition inhomogeneity in grains. The key finding of TEM elemental mapping analysis is that Cu

atoms were found to be rich in the inner part of $Sm(Co, Cu)_5$ grains or particles, instead of the outer part, such as grain boundaries or edges of voids. Cu served as an alloying element in $Sm(Co, Cu)_5$ grains, not as a doping element to form Cu-rich grain boundaries. A model of $Sm(Co, Cu)_5$ films with in-plane graded anisotropy due to composition/crystallization variation can explain the huge difference between the Hc and H_K as well as the angular dependences of coercivity and remanence coercivity. A simple analytical expression of the angular dependence of switching field for graded media has been derived and shown to match well with experimental results.

Chemical stability of $Sm(Co, Cu)_5$ thin films has been studied. Ta-capped $Sm(Co, Cu)_5$ thin films are stable in terms of structural and magnetic properties in a normal laboratory environment (25 °C) over 3 years, but they did not pass the accelerated corrosion test (130°C, 95%RH, 6 hours). A capping layer consisting of a hcp-phased CoPt-alloy layer and carbon overcoat should help $Sm(Co, Cu)_5$ thin films meet the requirements for future high-density magnetic recording applications.

$L1_0$-type FePt thin films were studied as perpendicular ECC media with potentially high gain factor due to domain-wall assisted magnetic switching. Ultra-thin exchange-coupled-composite (ECC) FePt granular recording media with different soft layer anisotropy were fabricated by controlling the soft layer deposition temperature. The structural and magnetic properties of soft layers ($FePt-SiO_2$) confirmed the feasibility of controlling the soft layer anisotropy by changing its deposition temperature. The effect of soft layer anisotropy field on the coercivity (H_c) and the remanent coercivity (H_{cr}) of ECC FePt thin films showed a "V" shape relationship, with the minimums at T_{Soft} of 200 °C. It is consistent with the theoretical prediction based on domain wall assisted magnetization reversal mechanism. The ECC FePt thin film with T_{Soft} of 200 °C may achieve a gain factor larger than 2.

Table of contents

List of Tables

List of Figures

Chapter 1. **Introduction**

1.1 **Brief Introduction of Magnetic Recording**

Nowadays, there is a saying that we are living in the information era. One reason is that the development of the Internet makes digitized information easily accessible to people. The growth of the Internet triggers the explosive increase of the amount of digital information. At the same time, the development and progress in high density hard disk drives (HDD) make it possible that the storage of digital information can keep pace with its fast-increasing volume. Magnetic recording is a key technology inside a hard disk drive.

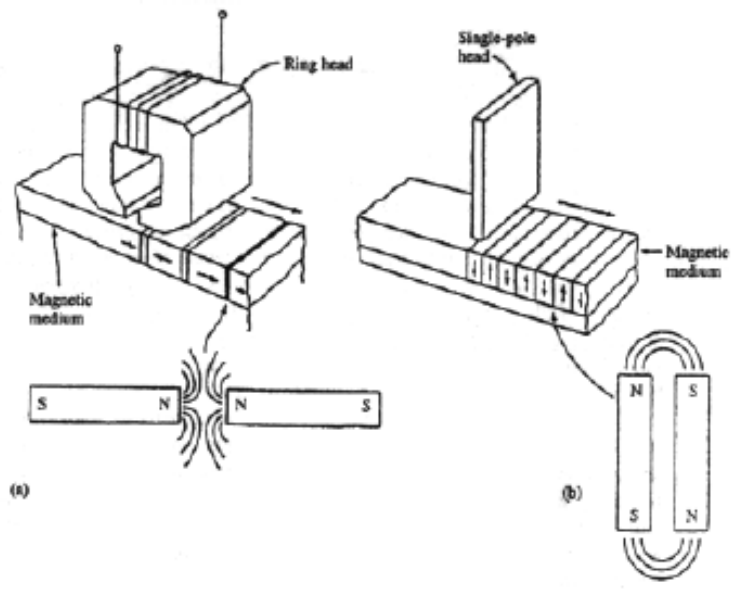

Figure 1.1 Schematic drawing of the principle of magnetic recording: (a) Longitudinal Magnetic Recording, (b) Perpendicular Magnetic Recording [Ashar 1996]

Fig. 1.1 shows the schematic drawing of the principle of magnetic recording (Ashar 1996). The digital information is stored in the magnetic medium which consists of sections with opposed magnetization. The binary digital information of 1 or 0 is

corresponding to the position where there is or isn't a transition of the magnetization in the medium. The principle is that the magnetic field above the transition is different from where there is no transition as shown in the figure. The recorded information can be read out by a Reader element (not shown here) which is sensitive to the change of a magnetic field due to either GMR (Giant Magnetoresistance) effect (e.g. Baibich et al. 1988 and Binasch et al. 1989) or TMR (Tunneling Magnetoresistance) effect (e.g. Moodera et al. 1995 and Miyazaki et al. 1995). Depending on the alignment of the magnetization of each section with respect to the magnetic medium (thin film), the digital information can be recorded by either (a) a Ring head in longitudinal recording where the magnetization of each section is in the film plane or (b) a Single-pole head in perpendicular recording where the magnetization of each section is normal to the film plane. Longitudinal magnetic recording technology was gradually replaced by perpendicular magnetic recording technology in around 2005~2006 when the areal density is above 200 Gbits/inch^2, due to the superparamagnetic effect and the requirement of higher writing field for higher density (http://en.wikipedia.org/wiki/Perpendicular_recording).

1.2 Limiting Factors to the Areal Density of Magnetic Recording

In a hard disk drive, the data is written as circular tracks. The number of tracks per inch along the radial direction is called track density (tracks/inch). Many bits are written in a single track. The number of bits per inch in the track direction is called linear density (bits/inch). The areal density is defined as follows:

$$\text{Areal density} = \text{linear density} \times \text{track density}.$$

The areal density in recent (Jan 2014) commercial new HDD products is about 700 Gbits/inch^2, with a linear density of about 2000 kBPI (kilo-bits per inch), a track density of about 350 kTPI (kilo tracks per inch) and a track pitch of about 70 nm. It is expected that the current perpendicular recording technology can achieve up to 1.1 Tbits/inch^2.

Chapter 1. Introduction

There are three fundamental requirements for magnetic recording designs: signal to noise ratio (SNR), thermal stability, and writability. The relationship between each other is known as the magnetic recording "trilemma", as shown in Fig. 1.2, since they may not be satisfied simultaneously in the extremely high density recording of future. They are the limiting factors affecting the areal density of magnetic recording. Media SNR is largely determined by the average number of grains per bit. With the progress of signal processing technique, this value may be reduced to about 20-30 grains per bit (Victora et al. 2002). Media thermal stability is determined by KuV. One major path to future extremely high density recording is to reduce the grain size (V) and increase the anisotropy constant (Ku). However, this will result in a very high coercivity in the media. The media coercivity may exceed the writing field that can be achieved by the high-Ms materials, and magnetic grains might not be fully switched. Very high coercivity will degrade the overall recording performance and fail at extremely high densities.

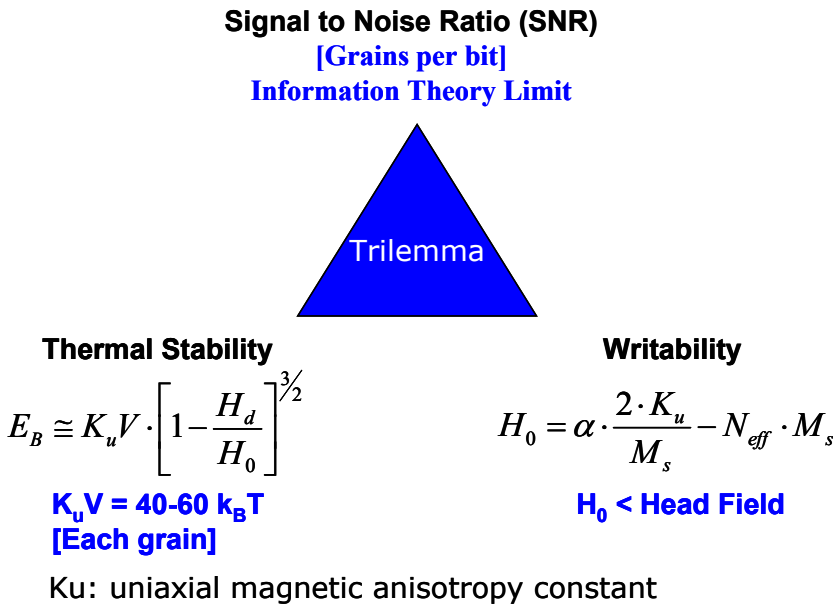

Figure 1.2 The trilemma in magnetic recording

Among the three factors, the media SNR issue can be largely solved if patterned media technology is mature, and the writability issue can be alleviated if any energy assisted magnetic recording is successful. The thermal stability factor determines the ultimate areal density can be achieved by any method. Since the grain size, V, is directly related to the areal density and cannot be reduced much, a large anisotropy constant, Ku, is the key to obtaining the highest possible areal density.

1.3 Current and Future Magnetic Recording Technologies for Higher Areal Density

In the order of maturity of technology, the current and future magnetic recording technologies for higher areal density are introduced as follows.

1.3.1 Exchange-coupled-composite (ECC) and anisotropy graded media

Exchange-coupled-composite (ECC) media was experimentally demonstrated by Wang et al. (2005) and theoretically proved in micro-magnetic simulation by Victora (2005) to provide higher thermal stability and lower writing field, compared to conventional perpendicular media with a single hard layer. ECC media consist of at least one magnetic hard layer, one magnetic soft layer, and one exchange coupling control layer in between, as shown in Fig. 1.3 (Shen 2006).

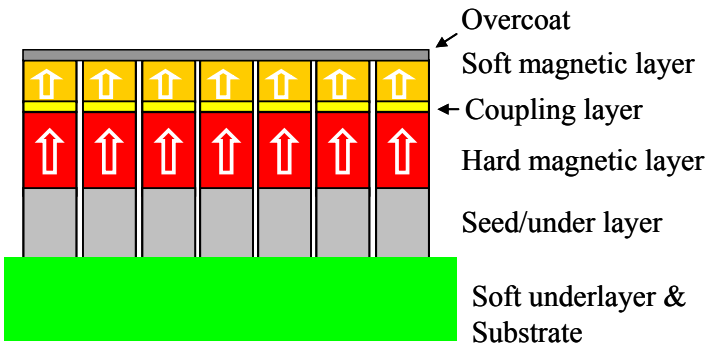

Figure 1.3 Basic structure of exchange-coupled-composite media. [Shen 2006]

In ECC media, the gain factor, which can be defined as $\xi \equiv 2\Delta E/(Hs \bullet Ms \bullet V)$ (Victora et al. 2005), determines the potential of the media. The initial theoretical calculations based on the two-layer approximation of ECC structure (Victora et al. 2005) suggested that the gain factor has a maximum value of 2. Further studies on ECC structure showed that the gain factor can be larger than 2 if the magnetization reversal mechanism is domain wall assisted switching (Robin et al. 2006 and Suess et al. 2008).

The ECC media structure was such a success that the HDD industry adopted the design soon after it was published, and the variants of this concept, e.g. anisotropy graded media that have three or more magnetic recording layers with gradual change of magnetic anisotropy, continued to be the focus of development of current commercial perpendicular recording media.

1.3.2 **Shingled magnetic recording (SMR)**

Shingled Magnetic Recording (SMR) was named after roof shingles (see HGST online website 1). It was first proposed by Kasiraj and Williams in their patent (US Patent 6967810 B2). With SMR, data is written to a hard disk drive using shingled writing scheme, i.e. each data track is partially overwritten when the next adjacent data track is written, as seen in Fig. 1.4 (Greaves et al. 2009).

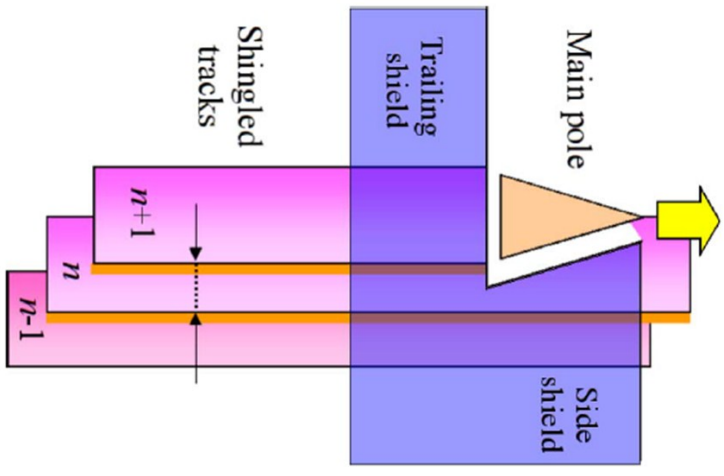

Figure 1.4 Shingled writing scheme. Written tracks and the arrangement of the main pole, side shield and trailing shield. [Greaves et al. 2009]

According to the simulation results of Greaves et al. (2009), areal densities of 2-3 Tbits/in^2 are predicted for shingled magnetic recording with a combination of continuous ECC media, an optimized single pole writer head, and other optimized parameters. Seagate expects to be the first to introduce the world's first SMR drive in 2014, which can improve areal densities by 25% in their first-generation product (see Seagate online website 1).

1.3.3 Two-dimensional magnetic recording (TDMR)

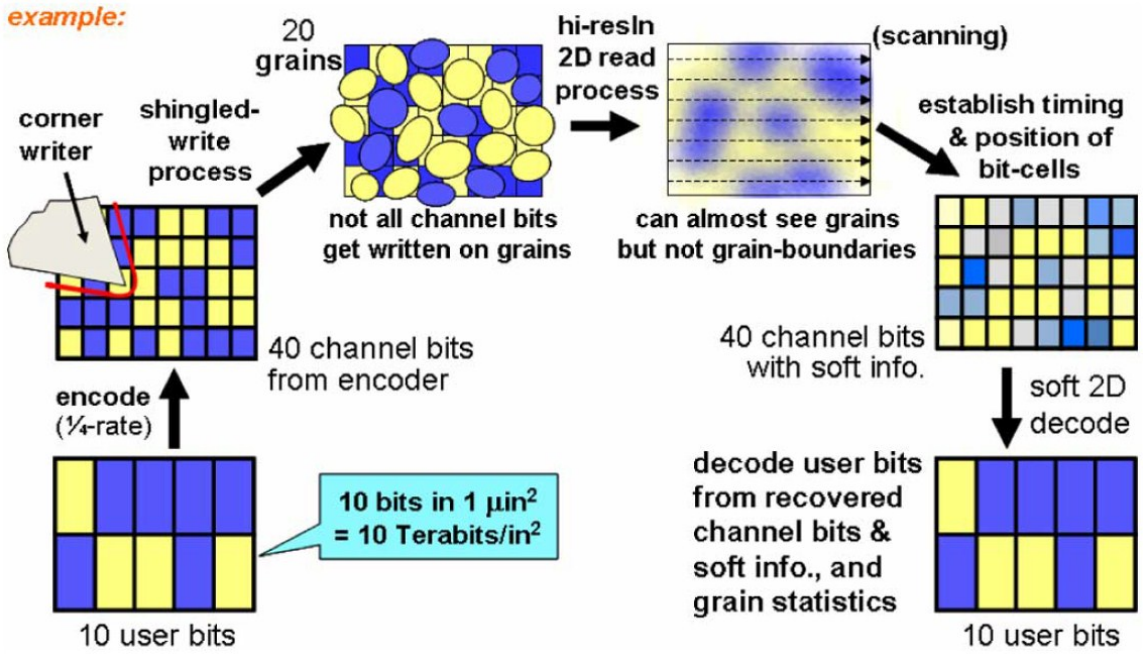

Figure 1.5 Toy example illustrating two-dimensional magnetic recording (TDMR). Note that Readback is accomplished using information gathered from several immediately adjacent tracks, either from successive scans or from an array head. A powerful two-dimensional soft decoder is needed to recover the user data. [Wood et al. 2009]

Wood et al. (2009) proposed a new magnetic recording scheme based on the SMR, which is called TDMR (two-dimensional magnetic recording), as shown in Fig. 1.5. With TDMR, All the signal-processing power that enables us to work with very high levels of intersymbol interference (ISI) can be equally applied to combat the inter-track interference. Two-dimensional signal-processing implies that we have available reasonably high-resolution information in the cross-track dimension as well as the down-

track dimension. Such information might be obtained using either an array of closely spaced sensors or by building up similar information in memory using several passes of a single head. Theoretically, areal-densities of the order of 10 Terabits per square inch may be achievable.

1.3.4 Heat-assisted magnetic recording (HAMR) or Energy-assisted magnetic recording (EAMR)

Both SMR and TDMR have no distinctly different requirements to the magnetic recording media from conventional perpendicular media, so as to obtain the benefit of these new technologies. This makes them relatively easier for the HDD industry to adopt, and new products with these technologies are soon to come alive.

One disruptive new technology called either EAMR or HAMR (same technology but named differently by different people) claimed to provide one order of magnitude higher areal density over traditional perpendicular recording (Kryder et al. 2008)

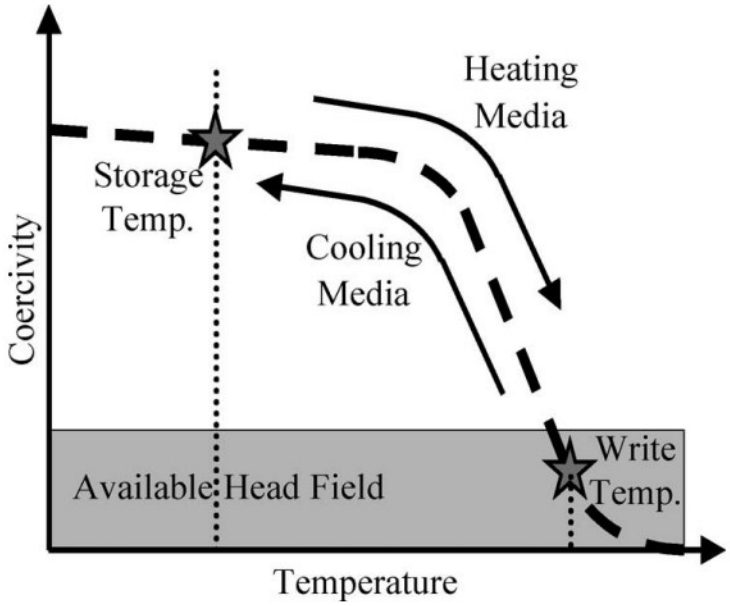

Figure 1.6 A schematic diagram of the HAMR write process is shown. [Kryder et al. 2008]

In this technology, a laser is used to momentarily heat the recording area of the medium to reduce its coercivity below that of the applied magnetic field from the recording head, as illustrated in Fig. 1.6. The recording materials in such system can have a very high magnetic anisotropy, which is essential for the thermal stability of the magnetization of the extremely small grains in the recording medium. This technology involves new recording physics, new approaches to near-field optics, a recording head that integrates optics and magnetics, new recording materials, lubricants that can withstand extremely high temperatures, and new approaches to the recording channel design. Many engineering challenges need to be solved before it is commercially applicable. Even though, prototype drives of HAMR capable of read/write operation for a short period had been demonstrated in Aug 2012 and Nov 2013, by Seagate and Western Digital respectively.

1.3.5 **Bit-patterned magnetic recording (BPMR)**

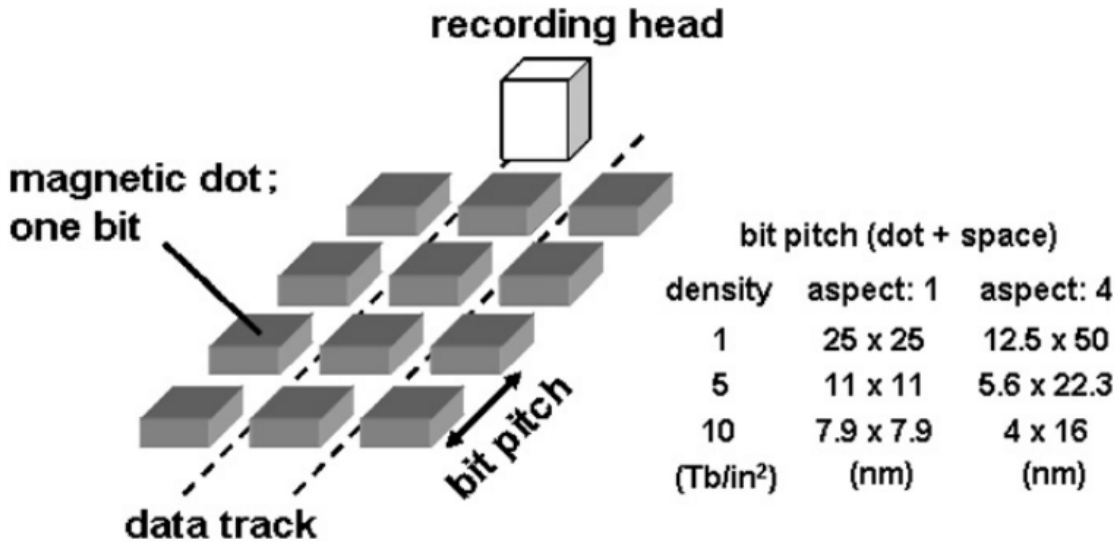

Figure 1.7 Schematic view of the bit patterned media and typical size of the bit for 1, 5, and 10 Tbit/in^2. [Kikitsu 2009]

As mentioned earlier in Section 1.2, BPMR technology uses one bit per magnetic grain or dot so that ideally traditional media DC noise due to multiple grains in one bit is

removed. Fig. 1.7 gives a schematic view of the bit patterned media and typical size of the bit for 1, 5, and 10 Tbit/in^2.

Although the idea of patterned media has already been proposed in the 1990s (Nakatani et al. 1989 and White et al. 1997), it is yet to be realized. The technology to fabricate such patterned media with high throughput and low-cost needs to be developed, and requires innovative solutions such as self-assembly and nanoimprinting, along with improved magnetic thin films for high anisotropy and narrow switching field distributions (Terris 2009).

1.4 Magnetic Materials for Magnetic Recording Media Application

Table 1.1 High Ku materials for potential magnetic recording media

type	material	K_u (10^7erg/cm^3)	M_s (emu/cm^3)	H_k (kOe)	T_c (K)	D_p (nm)
Co alloys	CoCrPt	0.20	298	13.7	--	10.4
	Co	0.45	1400	6.4	1401	8.0
	Co_3Pt	2.0	1100	35	--	4.8
$L1_0$ alloys	FePd	1.8	1100	33	760	5.0
	FePt	6.6-10	1140	116	750	3.3-2.8
	CoPt	4.9	800	123	840	3.6
	MnAl	1.7	560	69	650	5.1
RE-TM	$Fe_{14}Nd_2B$	4.6	1270	73	585	3.7
	$SmCo_5$	11-20	910	240-400	1000	2.7-2.2

(D_p is the minimum stable grain size in cubic shape) $D_p = (60\ k_B T/K_u)^{1/3}$ (τ=10 years)

Table 1.1 summarized high Ku materials for potential magnetic recording media (Weller et al. 2000). All the materials fall into three categories: Co alloys, $L1_0$ phase alloy, and rare-earth transition metal alloy. The easy axis orientation of all of these materials can be aligned along the out-of-plane direction for perpendicular recording, provided that

the right choice of substrates and underlayer/seed layer structures and proper deposition conditions are used.

Co alloys have the lowest Ku values in the above table. However, in hard disk drive industry, Co alloys or their composites have played a dominant role, and are often called as conventional magnetic recording media. For example, CoCrPtB thin films had been used as the advanced longitudinal recording media for a long time. CoPt-oxides are being used in the magnetic thin films of perpendicular recording media, which was commercially available since 2006 and remained as the only materials in current commercial HDDs of using perpendicular recording. In the foreseeable future, the highest areal density with conventional media can be achieved up to 1.1 Tbits/inch^2. New magnetic recording technologies with same conventional media may further increase the areal density. For example, HDD industry is currently developing the Shingled Magnetic Recording (SMR), which may provide a 30-50% higher areal density over the traditional perpendicular magnetic recording. Bit-patterned magnetic recording (BPMR) has an even larger promise in areal density increase, but it is also much more difficult to succeed.

All $L1_0$ phase alloys as shown in Table 1.1 have very high Ku values. Among them, $L1_0$ FePt was the highest one, with a Ku of 6.6-10 $\times$ 10^7 erg/cm^3 and a minimum stable grain size of 3.0 nm. $L1_0$ phase alloys have a face-centered tetragonal structure with a lattice ratio c/a less than 1.0. The easy axis is along *c* lattice direction. In order to apply this type of alloys in perpendicular magnetic recording, (001) texture is required. This texture can be realized through the epitaxial growth of (001) $L1_0$ FePt on right underlayers or substrates. Much work have been on the (001) textured $L1_0$ FePt thin films since it is considered to be the most-preferable candidate to replace the Co alloys for future perpendicular media up to 10 Tbits/inch^2 (e.g. Xu et al. 2007). A good review on the study of $L1_0$ FePt thin films as magnetic recording media can be seen in Wang (2013). In this thesis, there is also a chapter covering part of our study on $L1_0$ FePt thin films.

Rare-earth (RE) transition metal (TM) alloys like $SmCo_5$ and NdFeB are used in permanent magnet applications, such as in generators and motors. RE-TM alloys not only have very high energy products, but also have extremely high anisotropies, especially for

$SmCo_5$, whose Ku value can be up to 2×10^8 erg/cm^3, i.e. ten times of the highest Ku of $L1_0$ FePt. Using this Ku value, it can be found that the minimum stable grain size is around 2.2 nm. Hence, $SmCo_5$ thin films would have the highest magnetic recording density if media thermal stability is the only limiting factor. The main focus of this thesis is on the development of $SmCo_5$ based thin films as potential magnetic recording materials.

1.5 Experimental

1.5.1 Sputtering system

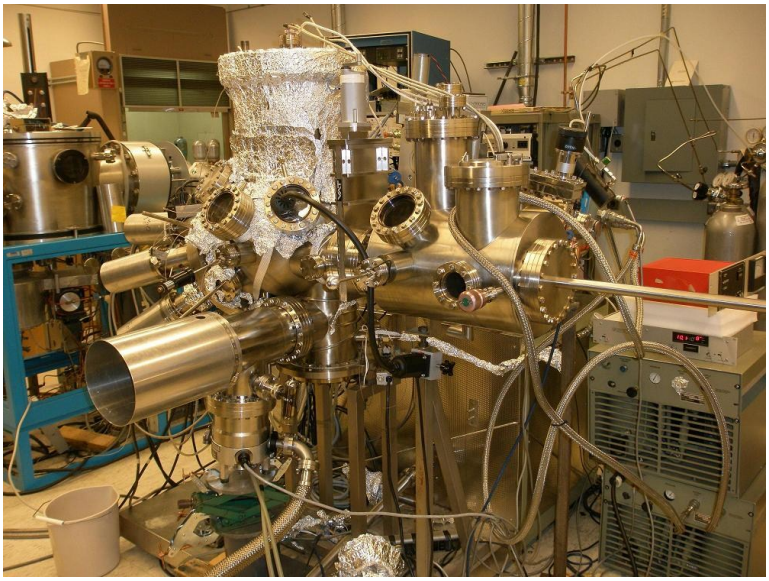

Figure 1.8 8-target magnetron sputtering

In this thesis work, an eight-target magnetron sputtering system modified from an MBE system, shown in Fig. 1.8, is used to fabricate all thin film samples. Eight cathodes of this system enable us to prepare samples with complex layer structures or multiple alloys with controlled compositions. One or two cathodes can be used for RF sputtering, so that non-conductive target/materials can also be used in thin film fabrication, e.g. the

SiO_2 doping in FePt layer as discussed in Chapter 6. The best vacuum of the sputtering chamber can be achieved is lower than $2x10^{-8}$ Torr, which is usually obtained after extended baking for two days at a chamber surface temperature of ~ 200 °C (heated by resistive belt wrapped around the main chamber) and pre-sputtering of all targets. Usually, the working gas is pure Ar, but O_2 or H_2 gas also can be mixed into Ar to form oxidative / reductive environment.

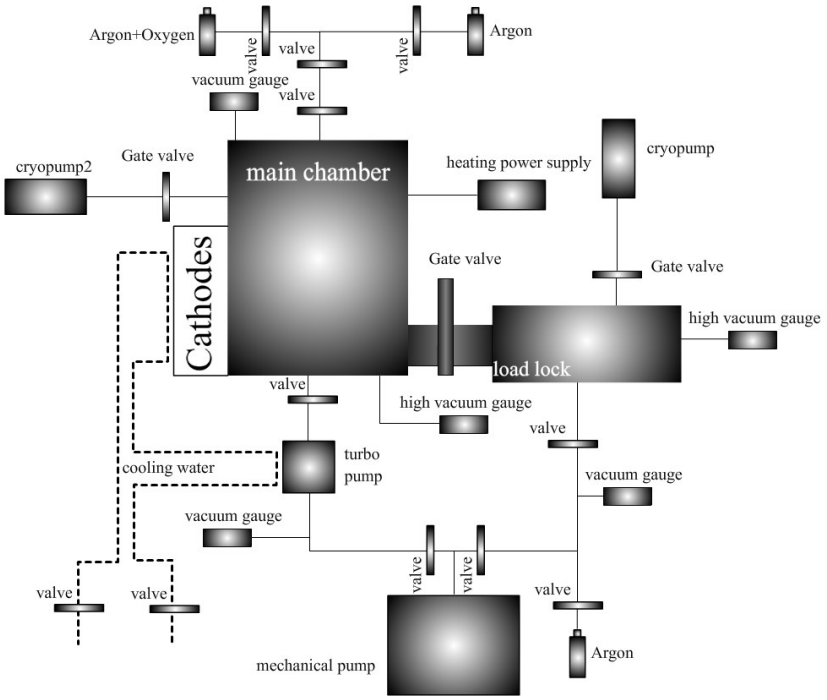

Figure 1.9 The schematic drawing of the 8-target magnetron sputtering system. [Wang 2013]

A schematic drawing of the system is shown in Fig. 1.9 (Wang 2013). This sputtering system contains two vacuum chambers. On the right is the load-lock chamber, which can store 5 substrate holders, for substrate loading and sample unloading. The biggest one in the center is the main chamber which connects the eight magnetron sputtering guns (cathodes) and is used for thin film deposition. The load-lock chamber is pumped by a cryopump (or a backup turbopump). The main chamber is pumped down by

a cryopump and a turbo pump, which is backed by a mechanical rotary pump. During sputtering, the main chamber is only pumped by the turbo pump, and the working pressure is controlled by adjusting the valve between turbo pump and main chamber. The mechanical pump is also used to pump down both chambers from atmosphere pressure to low vacuum in cases that the whole system is open for maintenance.

A heater is equipped in the main chamber and placed at the back side of the substrate holder. It can be used to not only heat the substrate before and during sputtering, but also anneal samples. The maximum temperature of safe operation (for several hours continuously) is around 450 ^{o}C.

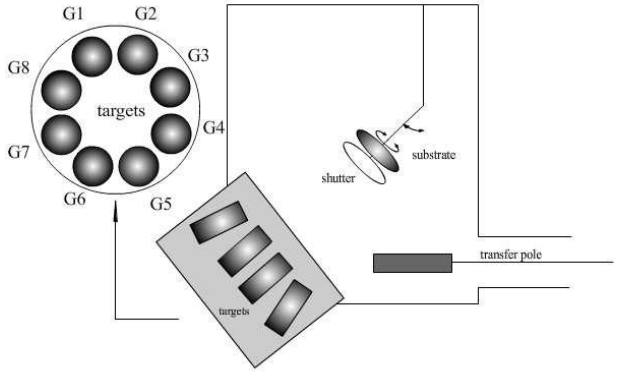

Figure 1.10 Schematic drawing of the sputtering configuration of the eight-target sputtering system. [Wang 2013]

Fig. 1.10 shows the schematic drawing of the sputtering configuration of the eight-target sputtering system. Eight magnetron sputtering guns are equally spaced on a circle. The substrate holder and its shutter are placed on a rotational stage, which is at the confocal point of the eight sputtering guns.

1.5.2 **Thin film characterizations**

The thickness of a thin film is usually measured by a surface profiler such as P-16 on pre-made steps. Other characterizations of the properties of a thin film are explained as follows.

Chapter 1. Introduction

A. Structural properties

Structural properties of thin films are characterized by X-ray diffraction (XRD). Normal θ-2θ scan and in-plane scan are used to determine phases and lattice constants of the thin films in this study. The X-ray Diffractometer, "Bruker‑AXS (Siemens) D5005", is used for normal θ-2θ scan, while the "Panalytical X'Pert Pro" is used for both normal θ-2θ scan and in-plane scan. Cu source is employed in both diffractometers.

B. Magnetic properties

Magnetic properties of thin films are characterized by Vibrating Sample Magnetometer (VSM) and magnetometer with a superconducting quantum interference device (SQUID). Princeton Measurements Micro-VSM is used to measured the magnetic properties of thin films at room and hot temperature (for Curie temperature measurement), up to about 18 kOe. A Quantum Design XL7 SQUID with a 7T field platform is used for high field measurement.

C. Surface analysis

Surface properties of thin films are characterized by Atomic Force Microscopy (AFM) and Scanning Electron Microscopy (SEM). In particular, a Bruker Nanoscope V Multimode 8 SPM and a Field Emission Gun–Scanning Electron Microscope (FEG‑SEM) – JEOL 6700 are used in this study.

D. Composition analysis

Film composition can be determined experimentally by Rutherford backscattering spectrometry (RBS). The MAS 1700 Pelletron Tandem Ion Accelerator (5SDH) equipped with charge exchange RF plasma source by National Electrostatics Corporation (NEC), located in the Characterization Facility, is used in this study. The accuracy of film composition determined by RBS depends on the uniformity and layer structure of the analyzed film. A freeware "QUARK" is used for RBS simulation.

E. Microstructure and micro-composition analysis

Microstructure and micro-composition of a thin film are usually investigated by a Transmission Electron Microscope (TEM). In this study, an FEI Tecnai T12 and an FEI Tecnai G2 30 with EDS are used for plane view and cross-section view TEM images and elemental mapping analysis.

1.6 Scope of this thesis

In this thesis work, a thorough review on the history and latest progress of studies on $SmCo_5$-based thin films for magnetic recording media applications is first presented. Future research and development focuses of $SmCo_5$-based thin films for magnetic recording media applications are also discussed.

With the highest bulk magneto-crystalline anisotropy constant at room temperature, $SmCo_5$ thin film is a promising candidate for extremely high areal density recording media. We will discuss how and why highly (0001) textured $Sm(Co, Cu)_5$ thin films can be obtained on Ru (0002) underlayer which is grown on a Ta seed layer. The effects of deposition temperature, film composition, layer thickness, and Cr-doped underlayer are investigated and discussed. Magnetization reversal mechanism of $Sm(Co, Cu)_5$ (0001) thin films is determined to be domain wall pinning dominant. Microstructure of various pinning sites and pinning mechanisms are studied by SEM, AFM, cross-sectional TEM, and planar TEM with HAADF and elemental mapping. A model assuming in-plane graded anisotropy in $Sm(Co, Cu)_5$ films due to composition/crystallization variation is introduced to explain the huge difference between the Hc and $H_{K,}$ as well as the angular dependences of coercivity and remanence coercivity. The simple analytical expression of the angular dependence of switching field for anisotropy-graded media, which was obtained from empirical fittings but matched well with experimental results, will be derived from the model. Chemical stability of our $Sm(Co, Cu)_5$ thin films is also investigated, and a proposal of solving the corrosion issue is discussed.

$L1_0$-type FePt thin film, the other promising candidate for future high-density magnetic recording, is also studied for potential applications as perpendicular ECC media with a high gain factor. Both the hard and the soft magnetic layers use FePt, but the soft layer with smaller anisotropy, which can be controlled by SiO_2 doping and deposition temperature. Based on domain-wall assisted magnetic switching theory, there should be an optimum anisotropy in the soft layer, which will give the largest gain factor. Our

Chapter 2. Review of Studies on $SmCo_5$-Based Thin Films for Magnetic Recording Media Applications

2.1 Introduction

In the future extremely high density magnetic recording, the center to center distance between magnetic grains of hard disk media is required to be shrunk continuously to support higher and higher recording areal density, while the magnetic anisotropy of these grains is still kept thermally stable, so the stored data will not lose over the time (typically >= 10 years) under normal environment. $SmCo_5$ ($CaCu_5$-type), which has the highest uniaxial magnetic anisotropies (1.1 - 2.0 × 10^8 erg/cm^3) at room temperature among current magnetic materials, can be considered as the ultimate material for future recording media. Purely based on the bulk properties, $SmCo_5$ should have the smallest grains (as small as 2 nm) that are still thermally stable for magnetic recording application. While the structural and magnetic properties of materials in the form of nanocrystalline or thin film may have some unique characteristics, they are closely related to the bulk properties of the same material.

In this chapter, the phase diagram and crystal structures of Sm-Co alloys and the origin of large magnetic anisotropy in $SmCo_5$ will be reviewed firstly, and then followed by the progress on the study of $SmCo_5$-based thin films for magnetic recording media application, according to the timeline each study, which transited from early amorphous Sm-Co films and Cr buffered $SmCo_5$ films with in-plane anisotropy to first $SmCo_5$ films with perpendicular anisotropy by using Cu underlayer with elevated substrate temperature at around 350 °C. Microstructure and composition analysis of Cu buffered $SmCo_5$ films revealed the importance of Cu diffusion into the $SmCo_5$ films from the Cu underlayer in lowering the crystallization temperature and developing the $SmCo_5$ (0001) texture and perpendicular anisotropy. This finding leads to later studies with direct Cu doping in $SmCo_5$ films, and the use of Ru underlayer, in order to eliminate the uncontrolled Cu diffusion and achieve smaller grain size in the underlayer. The bulk

properties of $Sm(Co, Cu)_5$ magnet is reviewed, before continued with the progress on the study of $Sm(Co, Cu)_5$ thin films formed directly by co-deposition of Sm, Co, and Cu.

Some relatively smaller topics are also covered. First is a unique bi-crystalline structure observed in $SmCo_5$ (0001) thin films grown on α-Al_2O_3 (0001) single-crystal substrate, due to two types of possible epitaxial orientation relationships between $SmCo_5$ (0001) and the buffer layers (Cu(111) or Ru(0001)), or α-Al_2O_3 (0001) substrate (rotating around film normal by 30 degrees). Secondly, there are some relatively new reports that $SmCo_5$ thin film with perpendicular anisotropy can be grown on a NiW underlayer, without the assistance of Cu. However, higher substrate temperature (>= 500 °C) during $SmCo_5$ deposition is needed for this new underlayer. The studies on the oxidation and corrosion protection of $SmCo_5$-based thin films with perpendicular anisotropy are also introduced, and followed by a briefing on the preliminary investigations of recording characteristics of $SmCo_5$-based recording media with perpendicular anisotropy.

At last, future development of $SmCo_5$-based thin films as potential magnetic recording materials is discussed, in terms of key requirements for different future recording technologies. Challenges in various aspects of the requirements are identified, and possible solutions are proposed and discussed.

2.2 Sm-Co Alloys: Phase Diagram and Crystal Structures

The Sm-Co binary alloy system has been studied extensively in experiments and also by theoretical calculations using thermodynamic functions, especially on the Co-rich side because two phases ($SmCo_5$ and Sm_2Co_{17}) on this side are the basis of two important families of permanent magnets. Okamoto (2011) reviewed related phase studies on Sm-Co alloys and gave the latest Sm-Co phase diagram as shown in Fig. 2.1. The Co-rich region (< 30 at.% Sm) of this phase diagram is mainly based on latest experimental results by de Campos and Landgraf (2000), while the uncertainty on the stability of $SmCo_5$ below 810 °C (the dashed line on the chart) indicates the unresolved disagreement between the work of Cataldo et al. (1996) and other works before it that found $SmCo_5$

phase is not thermodynamically stable below 810 °C. Other regions of the phase diagram are mainly based on the experimental works of Ge et al. (1993) and Yuan et al. (2010). Yuan et al. (2010) reinvestigated the Sm-rich side (< 40 at.% Co) by means of DTA (Differential Thermal Analysis) and X-ray diffraction analysis, and confirmed that Sm_9Co_4 should be replaced by Sm_5Co_2, as claimed by Moreau and Paccard (1976).

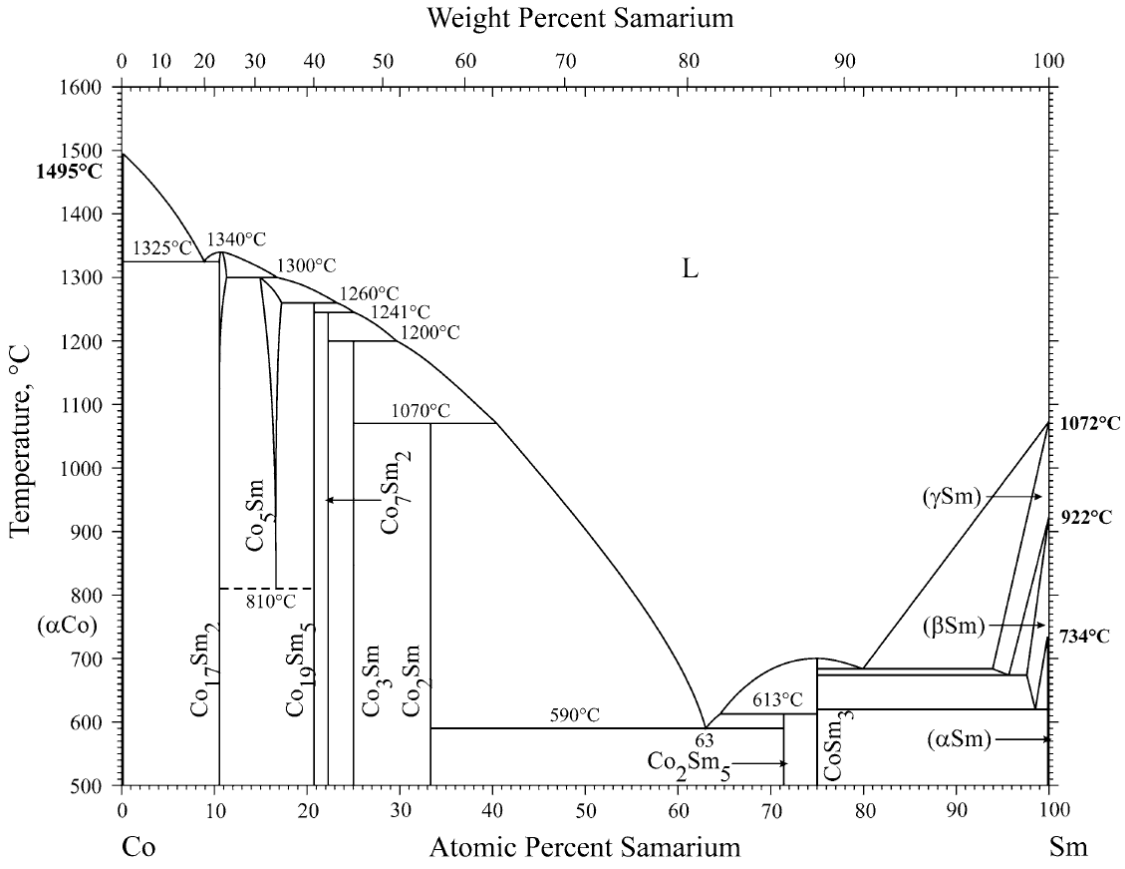

Figure 2.1 The latest Sm-Co phase diagram. [Okamoto 2011]

The latest theoretically calculated Sm-Co phase diagram by Yuan et al. (2011) agreed well with the Fig. 2.1. There are eight compounds in the Sm-Co system. Based on an analysis of experimental data and the crystal structures of the phases, $SmCo_5$ was modeled as $(Co, Va)_{0.833333}(Co2, Sm)_{0.166667}$ and Sm_2Co_{17} as $(Co)_{0.833333}(Sm)_{0.111111}(Co2, Sm)_{0.055556}$ in this study. These formulas indicate, in $SmCo_5$, some Sm sites can be

substituted by Co2 (a dumbell Co pair as visualized later in the crystal structure of Sm_2Co_{17}, Fig. 2.5), and some Co sites can be vacancies; while in Sm_2Co_{17}, 1/3 of Sm sites can be substituted by Co2. The remaining six intermetallic phases, Sm_3Co, Sm_9Co_4, $SmCo_2$, $SmCo_3$, Sm_2Co_7, and Sm_5Co_{19}, were treated as stoichiometric compounds. Calculations based on these parameters can reproduce most of the experimental data very well.

Table 2.1 Crystal structure data and Curie temperatures of Sm-Co phases.

Phase	Space group (Symbol, No.)	Prototype	Pearson symbol	Lattice Constant[a] (Å)	T_c (K)
Sm_2Co_{17}	*R*$\bar{3}$ *m*, 166	Th_2Zn_{17}	*hR*57	a = 8.395 c = 12.216	1173[b]
	P6$_3$*/mmc*, 194	Th_2Ni_{17}	*hP*38	a = 8.360 c = 8.515	
$SmCo_5$	*P6/mmm*, 191	$CaCu_5$	*hP*6	a = 5.001 c = 3.966	955[b]
Sm_5Co_{19}	*R*$\bar{3}$ *m*, 166	Ce_5Co_{19}	*hR*72	a = 5.031 c = 48.402[c]	786[b]
Sm_2Co_7	*R*$\bar{3}$ *m*, 166	Gd_2Co_7	*hR*54	a = 5.061 c = 36.504[d]	705[b]
	P6$_3$*/mmc*, 194	Ce_2Ni_7	*hP*36	a = 5.041 c = 24.327	
$SmCo_3$	*R*$\bar{3}$ *m*, 166	$GdCo_3$	*hR*36	a = 5.050 c = 24.590	533[b]
$SmCo_2$	*Fd*$\bar{3}$ *m*, 227	$MgCu_2$	*cF*24	a = 7.260	204[e]
Sm_5Co_2	*C2/c*, 15	Mn_5C_2	*mC*28	a = 16.282 b = 6.392 c = 7.061 β = 96.6° [f]	-
Sm_3Co	*Pnma*, 62	Fe_3C	*oP*16	a = 7.090 b = 9.625 c = 6.342	78[g]

Sources: (a) Buschow (1968), (b) de Campos (2000), (c) Khan (1974b), (d) Khan (1974a), (e) Burzo (1990), (f) Moreau (1976), (g) Sato (1994). Lattice constants are from (a) unless specified.

Chapter 2. Review of Studies on $SmCo_5$-Based Thin Films for Magnetic Recording

Table 2.1 shows the Curie temperatures (T_c) and crystal structure data of Sm-Co phases. It is seen that only phases with the Co content more than $SmCo_3$ have T_c higher than room temperature, i.e. ferromagnetic at room temperature; and T_c increases generally with higher Co content. This is one of the key reasons that Sm_2Co_{17} and $SmCo_5$ are widely studied for high-temperature permanent magnet applications (other reasons include large uniaxial magneto-crystalline anisotropy, and high energy product, (*BH*)max).

The crystal structures of Sm-Co phases on the Co-rich side can be better understood by dividing them into two groups according to the Sm/Co ratio, in which $SmCo_5$ phase serves as a boundary. In the first group, all Sm-Co phases between 1:2 and 1:5 stoichiometries can be described by the formula $Sm_{n+2}Co_{5n+4}$ (Cromer 1959 and de Campos 2000). This formula shows clearly the commonality of these phases that they consist of layers with two different crystallographic structures. One layer is of 1:2 type (Sm_2Co_4), following the fcc structure ($MgCu_2$ prototype). The other is of 1:5 type (Sm_nCo_{5n}), following the hexagonal structure ($CaCu_5$ prototype). The second group includes $SmCo_5$, Sm_2Co_{17}, and the phases between 1:5 and 2:17 stoichiometries by the formula $Sm_{1-x}Co_{5+2x}$. For example, this formula describes the disordered $SmCo_7$ ($TbCu_7$-type structure, metastable, not shown in the Sm-Co phase diagram) as a derivative of the ordered $SmCo_5$ ($CaCu_5$-type structure) whose Sm sites (1a site, in terms of Wyckoff positions) are randomly substituted by Co-Co dumbbells with a ratio (x) of 2/9 (Buschow and Van der Goot 1971, Li et al. 2010). Sm_2Co_{17} phase corresponds to $x = 1/3$, where one third of Sm atoms in the basal plane are orderly substituted with a dumbbell pair of Co atoms.

The program VESTA 3 (Momma and Izumi 2011) is used to visualize the crystal structures of various phases discussed in this thesis. Atom coordinates of each phase are taken from standardized crystallographic data based on published crystallographic data, as given by The Landolt-Bornstein Database of Springer Materials (http://www.springermaterials.com/).

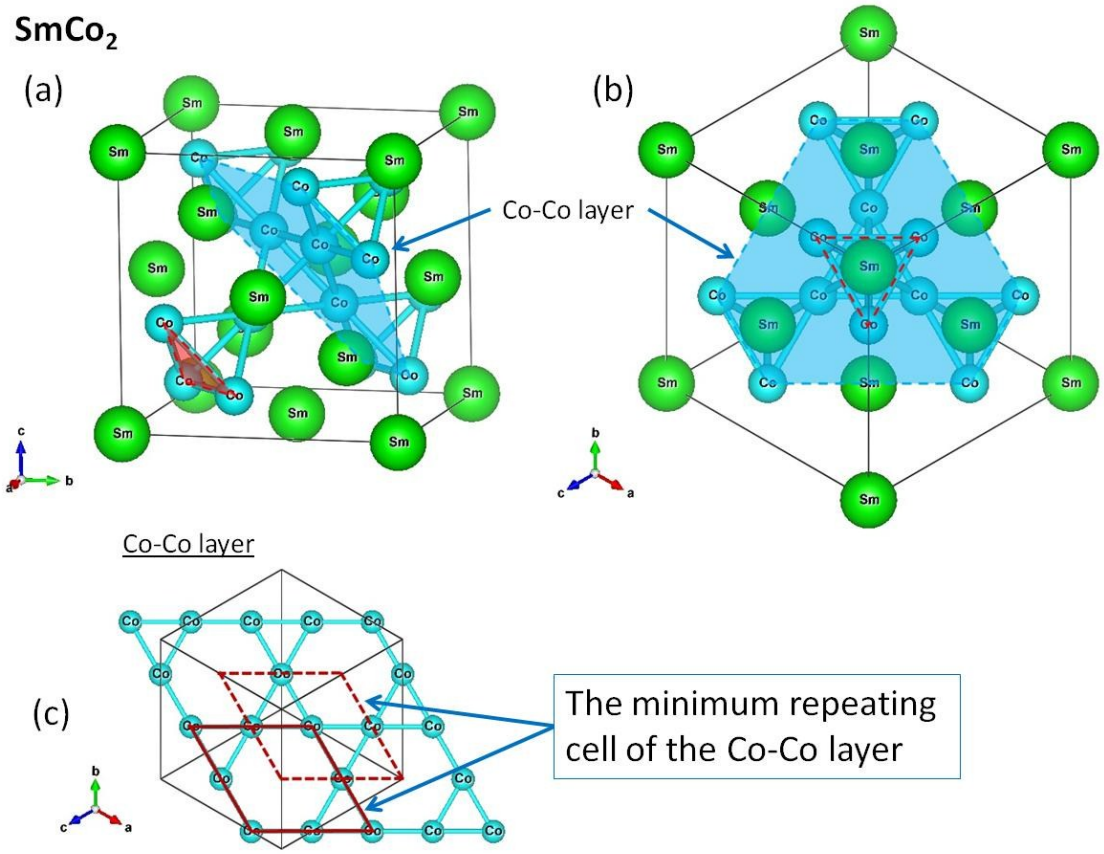

Figure 2.2 (a) and (b) The crystal structure of $SmCo_2$ at different view angles of the unit cell; and (c) the minimum repeating cell of the Co-Co layer. (Structural images are generated by VESTA 3, a program developed by Momma and Izumi 2011).

Fig. 2.2 and 2.3 show the crystal structures of $SmCo_2$ and $SmCo_5$, respectively, at different view angles, and the minimum repeating cells of the Co-Co layer (so-called "welding layer" by Parthe and Lemaire 1975). It is clearly seen that the Co-Co layers of the two phases have the same structure and close atomic distances. The atoms between the Co-Co layers can be regarded as an intermediate layer which is Sm-rich.

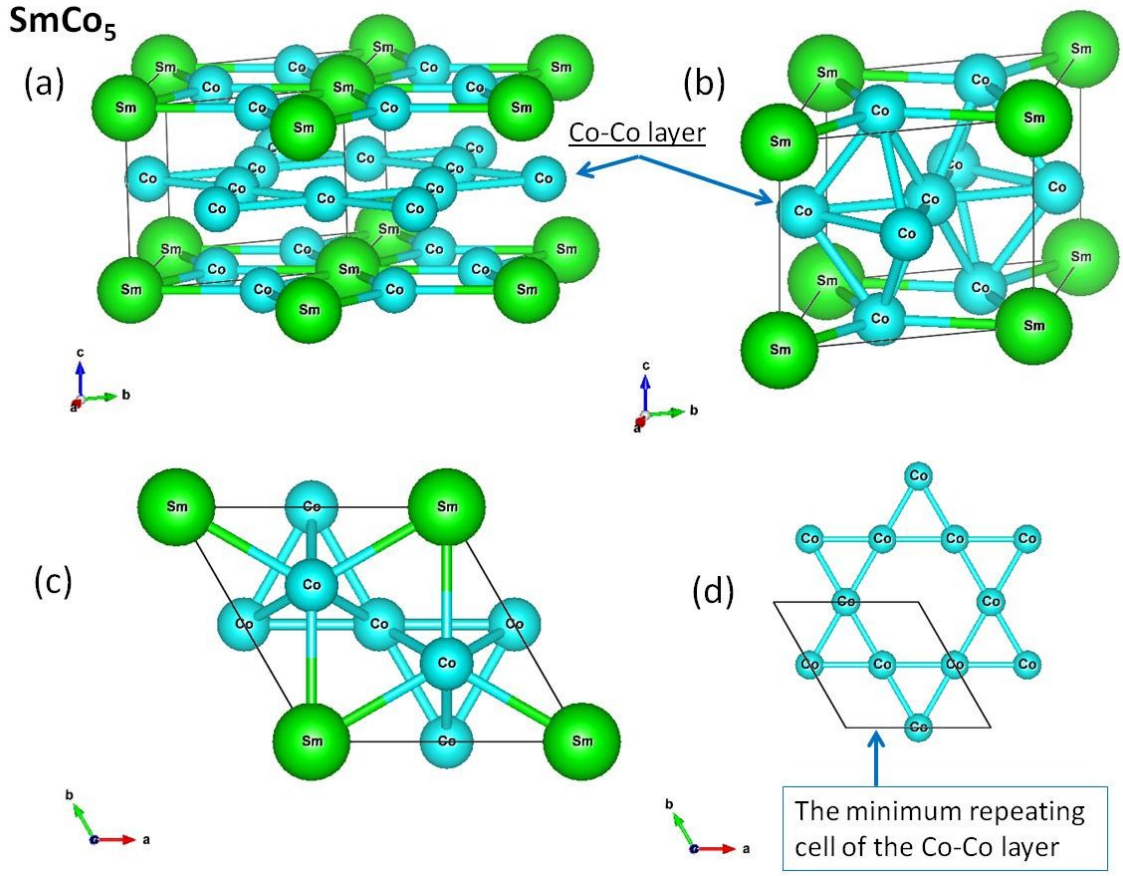

Figure 2.3 (a) The crystal structure of $SmCo_5$ unit cell; (b) and (c) the crystal structure of $SmCo_5$ primary cell at different view angles; and (d) the minimum repeating cell of the Co-Co layer. (Structural images generated by VESTA 3)

Parthe and Lemaire (1975) provided a good schematic drawing of the structure blocks (Sm_2Co_4 and $SmCo_5$) in $SmCo_2$ and $SmCo_5$ phases, which showed clearly the similarity and differences in their intermediate layers, as shown in Fig. 2.4. The Sm/Co ratio in the intermediate layer of $SmCo_2$ is 2:1, while it is 1:2 in that of $SmCo_5$. The larger Sm/Co ratio in $SmCo_2$ causes the up/down displacements of Sm atoms along the c-axis away from the center plane where Co atoms stay.

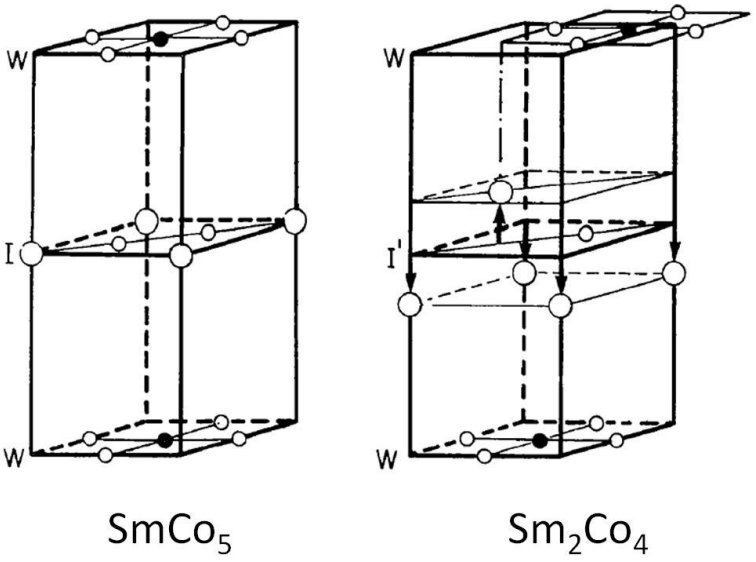

Figure 2.4 Schematic drawing of the structure blocks of $SmCo_5$ and Sm_2Co_4, where for reasons of clear presentation, the *c/a* ratio is three times larger than the real one. Co atoms are shown as small circles, Sm atoms as large circles. W and I (I') represent the welding layer and the intermediate layer, respectively. (Adapted from Parthe and Lemaire 1975)

Fig. 2.5 shows how $SmCo_2$, $SmCo_5$, and the phases between them can be described by stacking of Sm_2Co_4 and $SmCo_5$ structure blocks (after Cromer and Larson 1959, Parthe and Lemaire 1975). This series of phases, $SmCo_2$, $SmCo_3$, Sm_2Co_7, Sm_5Co_{19}, and $SmCo_5$ correspond to n = 0, 1, 2, 3, ∞, respectively, in the $Sm_{n+2}Co_{5n+4}$ structure series. A close relationship between two types of crystal structure (hexagonal and rhombohedral), due to different stacking orientations, is clearly revealed. It is noted that, for Sm_2Co_7, the coexistence of both allotropic forms, hexagonal (Ce_2Ni_7 prototype) and rhombohedral (Gd_2Co_7 prototype), has been observed; while, for Sm_5Co_{19}, there is doubt about the stability of the hexagonal phase or coexistence of the hexagonal and rhombohedral 5:19 allotropic forms, according to de Campos and Landgraf (2000).

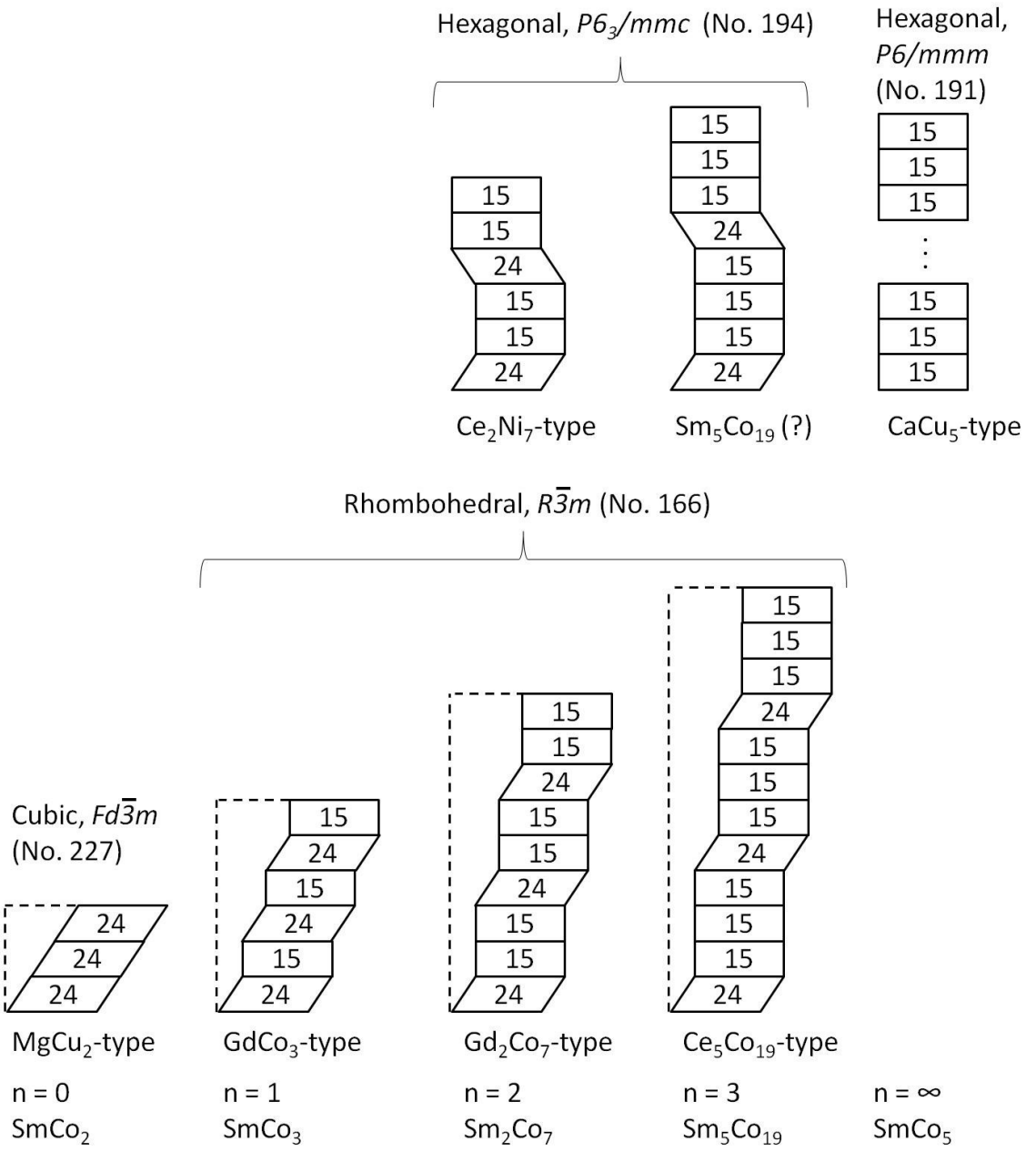

Figure 2.5 The crystal structure types of $SmCo_2$, $SmCo_5$, and the phases between them described by stacking of Sm_2Co_4 and $SmCo_5$ structure blocks. 24 denotes a Sm_2Co_4 block and 15 a $SmCo_5$ block.

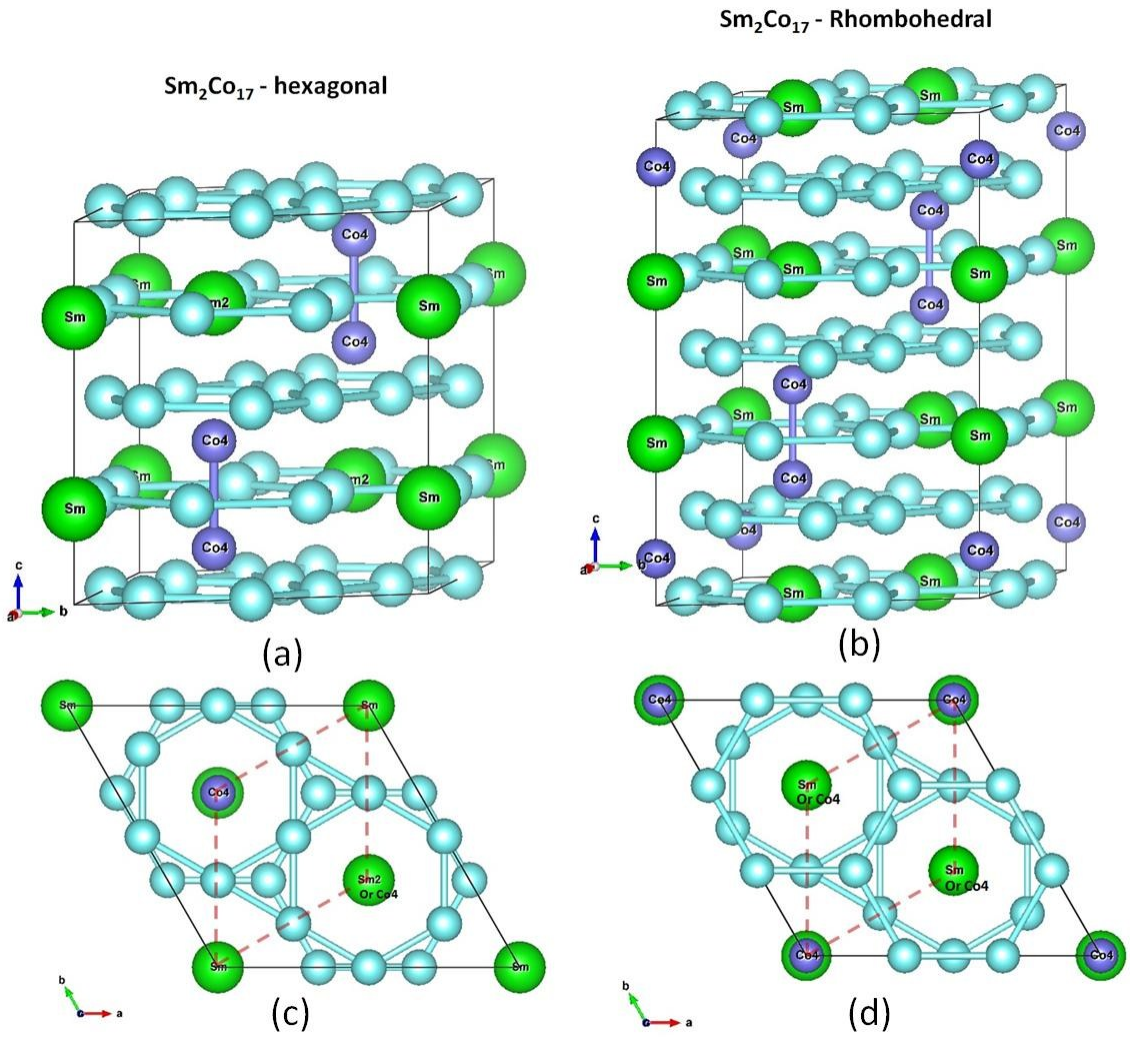

Figure 2.6 The crystal structures of Sm_2Co_{17} unit cells: (a) and (c) hexagonal, and (b) and (d) rhombohedral. (Structural images generated by VESTA 3)

It is easy to understand the crystal structures of the second group of Sm-Co phases, by looking at the crystal structures of Sm_2Co_{17} phases as shown in Fig. 2.6. Two variants of Sm_2Co_{17} (hexagonal and rhombohedral phases) are formed due to different stacking schemes of the substituting Co-Co dumbbells (Co4 atoms in Fig. 2.6). In the Hexagonal structure, there are two kinds of Sm sites: one (Sm2 in Fig. 2.6) is partially and periodically substituted by Co-Co dumbbells, the other is not. But in the Rhombohedral structure, all Sm sites are equally and periodically substituted by Co-Co dumb-bells. For

the disordered and metastable phases between 1:5 and 2:17 stoichiometries by the formula $Sm_{1-x}Co_{5+2x}$ (such as the disordered $SmCo_7$ phase), the Sm sites are substituted randomly by Co-Co dumbbells.

The above discussion on the crystal structures of $SmCo_5$ and phases near it shows the close relationship between them: on the Sm-rich side, a whole series of $Sm_{n+2}Co_{5n+4}$ structures (Sm_5Co_{19}, Sm_2Co_7, etc.) can be formed with the addition of periodical Sm_2Co_4 blocks; on the Co-rich side, another series of $Sm_{1-x}Co_{5+2x}$ structures ($SmCo_7$ and Sm_2Co_{17}) are readily formed by the periodical or random substitution of Sm with Co-Co dumbbells. This close relationship helps understand the decomposition of $SmCo_5$ into Sm_5Co_{19} and Sm_2Co_{17} as shown in the Sm-Co binary phase diagram.

2.3 Origin of the Large Magnetocrystalline Anisotropy of $SmCo_5$ Alloy

The uniaxial structure together with the orbital angular moment of the R species (R stands for rare earth elements) is the source of the magnetocrystalline anisotropy of the RCo_5 system (O'Handley 2000). It is generally understood that the main source of the large magnetic anisotropy energy (MAE) in $SmCo_5$ and other Sm-Co magnets is large magnetic single-site anisotropy of the Sm *f* shell (e.g. Steinbeck et al. 2001, Hummler and Fähnle 1996, and Richter et al. 1992). In simple terms, as described by Larson et al. (2003), this means the strong spin-orbit coupling tries to align the Sm *f* shell with the magnetic field, causing the *f* shell to rotate with the field. Sm atoms in a lattice interact with the crystal electric field, and the energy of this interaction depends on the orientation of the Sm *f* shell in the lattice. This spin-orbit coupling is the leading contribution to the MAE. Note that if the crystal electric field is too small, the *f* shell rotates freely with the magnetic field, producing no MAE, while if the spin-orbit coupling is too small, the orbital moment is quenched and again no MAE appears.

Larson et al. (2003) calculated the MAE of $SmCo_5$ based on first-principles theory using density functional theory (DFT) in which the Sm *f* bands were treated within the

LDA + U formalism. The calculations confirmed that the large MAE comes mostly from the Sm *f*-shell anisotropy, stemming from an interplay between the crystal electric field and the spin-orbit coupling. It was also found that both the crystal electric field and the spin-orbit coupling are of similar strengths, leading to a partial quenching of the orbital moment, an optimal situation for enhanced MAE. A smaller portion of the MAE could be associated with the Co-*d* band anisotropy, related to the peak in the density of states at the Fermi energy.

The above understanding of the origin of MAE of $SmCo_5$ has significant implications on the magnetic anisotropy of a $SmCo_5$ thin film, because the crystal electric field will depend on the local stress and strain of $SmCo_5$ grains experienced in the thin film, especially when the $SmCo_5$ thin film is grown epitaxially with relative large mismatch to the underlining lattice (underlayer or substrate). It is also helpful in understanding of the large anisotropic field of certain $Sm(Co,M)_5$ alloy, when Co is partially substituted by M atoms (e.g. Cu and Ni), as discussed later.

2.4 Studies of $SmCo_5$ Thin Films as Potential Longitudinal Magnetic Recording Materials

2.4.1 Amorphous Sm-Co thin films

Early HDD employed longitudinal magnetic recording, where recording media with in-plane anisotropy were used. Amorphous $Sm_{100-x}Co_x$ ($75 < x < 90$) thin films had been considered for magnetic recording material as early as in 1984 (Kullmann et al.), which showed a considerable improvement relative to particulate (γ-Fe_2O_3) and CoP thin film disks. The formation of a saw-tooth-like domain wall at the magnetization transition was found, which was believed to be a limiting factor for the recording performance of SmCo thin films.

Velu and Lambeth (1992) conducted a systematic study of the application of Sm-Co thin films in longitudinal recording. Fig. 2.7 gives a schematic diagram showing various layers and their thickness ranges studied in Sm-Co/Cr hard disk. In this study, Sm-Co/Cr

thin films with coercivity up to 3000 Oe were prepared by RF-diode sputtering without substrate heating. A Cr (110) underlayer was used to try to induce microcrystalline, and it significantly reduced the exchange interaction and hence the noise level in Sm-Co films. No XRD results were reported. However, as these Sm-Co films were deposited without substrate heating and any post-annealing, amorphous Sm-Co dominant films are expected, although the textured Cr (110) underlayer was used.

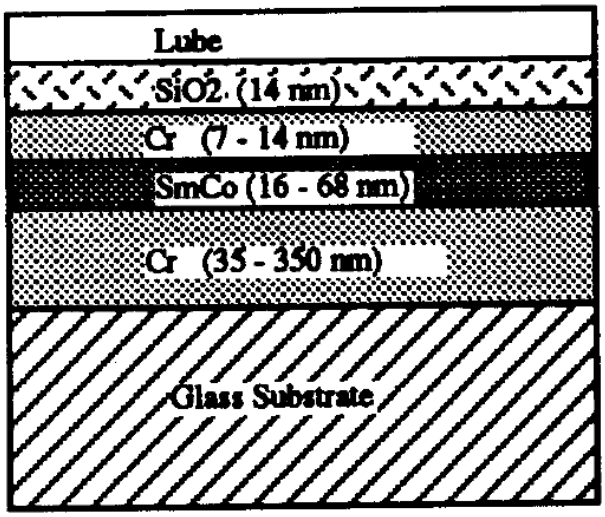

Figure 2.7 A schematic diagram showing various layers and their thickness ranges studied in SmCo/Cr hard disk. (Velu and Lambeth 1992)

The Cr underlayer continued to be the underlayer for Sm-Co thin films in all the later studies targeting at longitudinal recording application. Liu et al. (1994) studied the nanostructures of Sm-Co on Cr thin films prepared by dc magnetron sputtering, with high-resolution transmission electron microscopy (HRTEM) and diffraction techniques. HRTEM micrographs show that the crystallites in the Sm-Co films as revealed by the lattice fringes, are distributed discontinuously in the matrix. The matrix is amorphous as indicated by microdiffraction study. The size of the crystallites is in the range of 2-5 nanometers. Takei et al. (1997) studied the effect of Ar gas pressure (P_{Ar}) on Sm-Co/Cr bilayer films and found that lower P_{Ar} gave higher coercivity and squareness because of better crystallized Cr underlayer. However, opposed effect of the P_{Ar} was also reported by

Liu et al. (2001). A possible reason for the conflict results could be due to the difference in the composition of these Sm-Co films. Both of the two studies did not show any quantitative analysis results of their Sm-Co film composition. Furthermore, no Sm-Co films in these two studies showed any crystalline characteristics in their XRD patterns. Therefore, opposed results may be possible.

Overall, amorphous Sm-Co thin film with Sm/Co ratio close to 1:5 had been studied as longitudinal recording media in the past, but it was never successful in the real application and was given up long ago even before the perpendicular magnetic recording technology emerged in the HDD industry.

2.4.2 $SmCo_5$ thin films with high in-plane anisotropy

The $SmCo_5$ thin film with large in-plane anisotropy may find its application in micro-electro-mechanical-system (MEMS), but it is not desirable for future high density magnetic recording media application. So here only a brief introduction is given on this topic.

High in-plane coercivity Sm-Co thin films on Cr underlayer can be obtained by either post-deposition annealing (e.g. Malhotra et al. 1996) or deposition at elevated temperature (e.g. Fullerton et al. 1997, and Zhang et al. 2008).

Malhotra et al. (1996) reported that the as-deposited Sm-Co films with a Cr underlayer had magnetic coercivities of about 500–2800 Oe, but after annealing at 500 °C coercivities as high as 31 kOe for Sm-Co/Cr films were observed. HRTEM study showed that crystallization, and grain growth is promoted by post-annealing for the Sm-Co films resulting in a large increase in coercivity. Fullerton et al. (1997) reported that epitaxial Sm–Co $(1\bar{1}\,00)$ and $(11\bar{2}\,0)$ films had been grown by magnetron sputtering onto Cr buffered single-crystal MgO (110) and (100) substrates at a substrate temperature T_s of 600 °C, respectively, while the Cr buffer layer had developed Cr(211) and (100) texture, respectively too. The Sm–Co $(1\bar{1}\,00)$ films exhibit uniaxial in-plane anisotropies of ≈ 20 – 25 T and room-temperature coercive fields that increase to 4.1 T as the film thickness decreases to 75 Å. The 3 T coercivities of the $(11\bar{2}\,0)$ films are independent of thickness.

Both studies showed very large in-plane anisotropy in their Sm-Co films, but did not claim the $SmCo_5$ phase was formed, probably because of the nominal film composition of Sm:Co is 2:7. But it is very possible the hard magnetic phase in their films is $SmCo_5$.

A more recent report (Zhang et al. 2008) showed that, even when deposited at a relatively low temperature (400 °C), a $SmCo_5$ thin film with $(11\bar{2}\,0)$ texture and an in-plane intrinsic coercivity up to 26.5 kOe can be grown on the Cr (200) underlayer and glass substrate. Higher in-plane coercivity was observed in thicker $SmCo_5$ layer, which was attributed to the improvement of the crystallinity of $SmCo_5$.

2.5 $SmCo_5$ Thin Films with Perpendicular Anisotropy on Cu Underlayer

To make the $SmCo_5$ thin films a good candidate for ultimate high density magnetic recording application, there are three major challenges, which include 1) orientation control – $SmCo_5$ thin film with perpendicular magnetic anisotropy; 2) requirements on microstructure and magnetic properties as in conventional recording media, such as magnetic cluster control – small and uniform grain size of $SmCo_5$ grains, exchanged-decoupling between grains, and a narrow anisotropy distribution of magnetic grains; 3) anti-corrosion control – enhance the anti-corrosion property of $SmCo_5$-based thin film media.

The first challenge seemed to be largely overcome since the discovery that highly textured $SmCo_5$ (0001) thin films were first grown on Cu (111) underlayer at relatively low substrate temperature (~ 350 °C). In this section, earlier works of Sm-Co thin film grown on Cu underlayer is introduced, and followed by the work in which the $SmCo_5$ thin films with perpendicular anisotropy were first obtained by using a Cu (111) underlayer and substrate heating. Broader investigations but under same system (Cu underlayer) are reviewed, such as the effects of 1) the thickness of the seed layer, underlayer, and $SmCo_5$ layer; 2) sputtering parameters (base pressure and substrate bias);

3) different seed layer materials. Microstructure and micro-composition analysis results are examined, and the important implications are discussed.

2.5.1 $SmCo_5$ (0001) thin films grown on Cu (111) underlayer

It is well known in thin film technology that, film structure and sputtering parameters are important to fabricate thin films with a specific texture. Usually a textured underlayer or a single-crystal substrate is needed to provide a base for an epitaxial growth of the thin film of interest. Besides, proper substrate temperature during deposition is often critical to obtaining the certain desired phase(s). In the case of preparing $SmCo_5$ ($CaCu_5$-type) thin films with perpendicular anisotropy, the two most-important factors are a proper underlayer and deposition temperature.

Chen et al. (1993) reported that a Sm–Co film sputter-deposited at a high Ar pressure and post-annealed at a high temperature showed perpendicular magnetic anisotropy. However, this Sm–Co film was amorphous and did not have the structure of the $SmCo_5$ phase. Neu et al. (2002) studied Sm-Co thin films prepared by pulsed laser deposition in an Ar atmosphere and claimed a perpendicular magnetic anisotropy in the film. In fact, however, the magnetic properties of the film seem to be isotropic in nature.

Sm-Co thin films with the composition close to $SmCo_5$ using Cu underlayer had been reported on 1994 (Okumura et al. 1994). The deposition temperature of all layers in this study was at room temperature, which led to a thin film consisting of mostly amorphous Sm-Co with a relatively small in-plane coercivity, although the Cu underlayer had an (111) texture. Post-annealing of as-deposited amorphous Sm-Co films on Cr underlayer in a vacuum can increase greatly the in-plane coercivity (from 200 Oe to more than 20 kOe), which was suggested to be associated with the domain-wall pinning at high anisotropy nanocrystallites of $SmCo_5$ phase embedded in an amorphous matrix (Prados and Hadjipanayis 1998).

At around 2003, the R&D focus of magnetic recording media in HDD industry was shifting from longitudinal recording media to perpendicular recording media, which

could support continuing growth of areal density in HDD products. The research focus of Sm-Co thin film studies for magnetic recording media applications has to be changed accordingly. $SmCo_5$ thin film with high perpendicular magnetic anisotropy is desired. Sayama et al. (2004b) are the first to report the growth of $SmCo_5$ ($CaCu_5$-type) thin films with high perpendicular anisotropy, by sputtering a Co/Sm multilayer, whose composition is close to $SmCo_5$, on a Cu underlayer, with the deposition temperature of 345°C.

Fig. 2.8 shows the crystal structure of $SmCo_5$ and the lattice matching between Cu (111) and $SmCo_5$ (001) (Sayama et al. 2004b). The crystal structure of $SmCo_5$ is that of a layer-by-layer configuration along the c-axis, consisting of atomic layer of Co and a layer containing both Co and Sm atoms (same as Fig. 2.3 (a)). The lattice misfit between Cu (111) and $SmCo_5$ (001) is about 2.3% (Cu (111) lattice is slighter larger), which is small enough to promote epitaxial growth of $SmCo_5$ (001) on Cu (111).

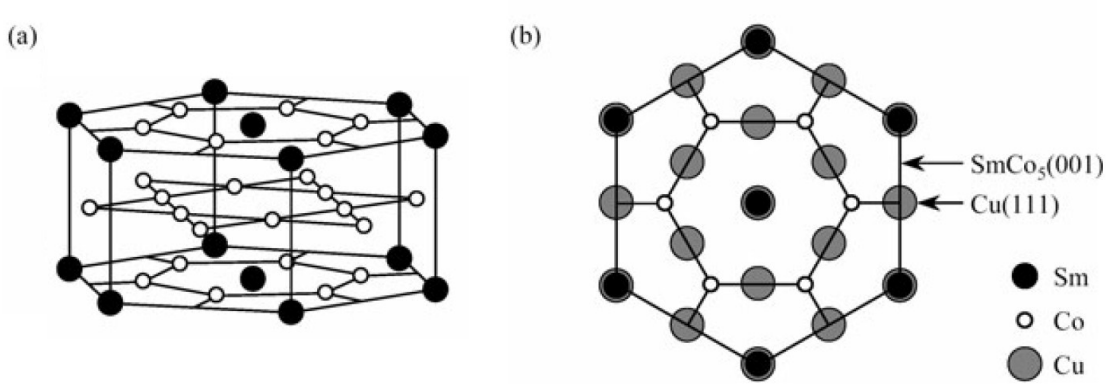

Figure 2.8 (a) Crystal structure of $SmCo_5$ with hexagonal unit cell. (b) Lattice-matching between Cu[110] (∥Cu(111)) and $SmCo_5$[100] (∥$SmCo_5$(001)). Black, white, and grey circles represent Sm, Co, and Cu atoms, respectively. [Sayama et al. 2004b]

Later improvements on magnetic and structural properties of $SmCo_5$ thin films were obtained by using a Ti seed layer under the Cu underlayer and depositing all underlayers at room temperature so that the Cu (111) texture can be improved. Sayama et al. (2004a) deposited $SmCo_5$ on a Cu (100 nm)/Ti (25 nm) dual underlayer at 325°C using sputtering. The Sm–Co layer was formed by laminating Sm (0.31 nm) and Co (0.41 nm) sublayer

alternately 35 times. A good (001) texture was achieved in $SmCo_5$ films because of the epitaxial growth relationship of $SmCo_5$ (001) on Cu (111). The $\Delta\theta_{50}$ value of $SmCo_5$ (002) was 3.1°, suggesting a highly orientated *c* axis. This strong structural anisotropy gives improved perpendicular magnetic properties in the film. The perpendicular anisotropy reached 4.0×10^7 erg/cm^3. The perpendicular coercivity and remanent ratio were 1.2 T and unity, respectively. Good magnetic properties can be maintained to thinner underlayers and Sm-Co layer as shown in Fig. 2.9 (Kawaji et al. 2005 and Sayama et al. 2006c).

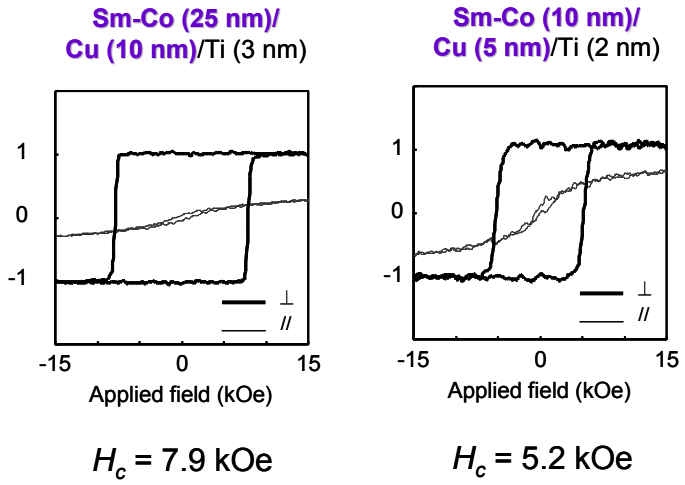

Figure 2.9 Magnetic properties of Sm-Co thin films on Cu/Ti underlayer. [Kawaji et al. 2005]

Jayama et al. (2004a) also tried to use a Sm-Co alloy target, but they failed to obtain good perpendicular anisotropy in Sm-Co thin films. However, Takei et al. (2004) fabricated successfully $SmCo_5$ with (00*l*) orientation on top of the Cu underlayer, with a composite SmCo target (Sm plates placed on a Co sheet). A key factor of success here seemed to be the Cu underlayer deposited without substrate heating, which produced a Cu underlayer of (111) texture with much smaller surface roughness (Ra ~ 4.1 nm) than

deposited at elevated temperatures (Ra ~ 26.7 nm), as confirmed later by Jayama et al. (2004b).

The grain size and the magnetic cluster size (defined as the correlation length where the value of the autocorrelation function for the MFM image at an AC-demagnetized state was zero) of $SmCo_5$ thin films prepared on the Cu underlayer are generally large (magnetic cluster size > 200 nm, as reported in Sayama et al. 2005b). Kato et al. (2006) studied Sm-Co thin film with Ru as a seed layer and an interlayer in addition to Cu underlayer, and found that the Ru seed layer was effective to reduce the grain size and roughness of Cu underlayer (from ~170 nm and 8.5nm to ~31 nm and 0.5 nm, respectively), and the Ru interlayer promoted the perpendicular magnetic anisotropy of Sm-Co film. However, the grain sizes or magnetic cluster sizes of the Sm-Co thin films were not mentioned. Another modification to the layer structure that helps reducing the grain size and roughness of Sm-Co thin films was to use Cr as the seed layer as well as the doping element in the Cu underlayer (Morisako et al. 2006a and 2006b). It was reported that the grain size of Sm-Co layer was reduced from ~110 nm with the Cr\Cu underlayer to ~40 nm with Cr\Cu-Cr (2 at.%) underlayer.

2.5.2 **Effects of layer thicknesses and sputtering parameters**

Sayama et al. (2006b and 2006c) studied the effects of thicknesses of Cu/Ti underlayer and Sm-Co layer and the base pressure of the sputtering system on magnetic properties of the $SmCo_5$ perpendicular magnetization films.

It was found that thicker Cu underlayer or $SmCo_5$ layer would lead to higher perpendicular coercivity, but Ti seed layer seemed to have an optimum value. Too thick or too thin of Ti may reduce the squareness ratio of $SmCo_5$ film. It was reported that a low base pressure equal to or better than 5×10^{-8} Torr is preferred to achieve the squareness close to 1 in the perpendicular direction of magnetic hysteresis loops as shown in Fig. 2.10.

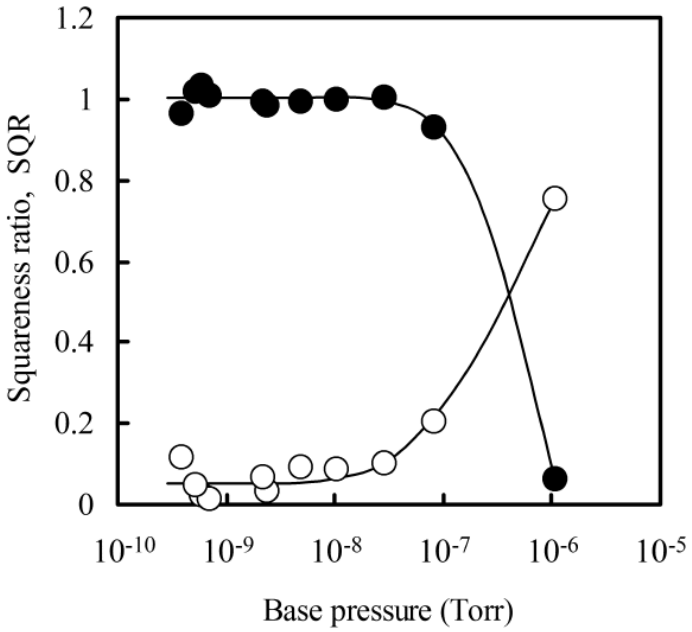

Figure 2.10 Relationship between the squareness ratio for films of Sm-Co (25 nm)/Cu (10 nm)/Ti (3nm)/glass_sub and the base pressure in the sputtering chamber before the films were deposited. Black and white circles represent the values in the directions perpendicular and parallel to the film plane, respectively (Sayama et al. 2006b).

Bias sputtering is well-known to assist in controlling the film morphology, structure, and physical properties through low energy ion bombardment of the growing film (see, e.g., Petrov et al. 1989, and Shi et al. 2000), which is well-known to minimize the gaseous impurity content (Frerichs 1962 and Maissel et al. 1965), influence the evolution of film structure and stress, and therefore modify the film properties (Rossnagel et al. 1990 and Ohring 1992). Wang et al. (2008) reported the deposition of $SmCo_5$ films (20 nm) with a Ti(5 nm)\Cu(20 nm) underlayer onto glass substrate using bias sputtering. $SmCo_5$ films with the best magnetic properties (H_c ~ 13.2 kOe and squareness ratio of 1 in the out-of-plane direction) were prepared at an optimum substrate bias of - 60V. At this substrate bias, the average grain size of 30 nm with an average surface roughness of 1.2 nm and a peak-to-peak value of 11.2 nm were also the best. $SmCo_5$ films with larger negative substrate bias showed larger average grain sizes and poorer structural and magnetic properties. This result was explained by the observation of the formation of Cu_3Ti phase due to the inter-diffusion at the interface between Cu and Ti, which

decreased the effective thickness of the Cu underlayer and degraded the Cu (111) texture and therefore the epitaxial growth of the $SmCo_5$ film on the Cu (111). While the grain sizes in these $SmCo_5$ films are still too large for recording media application, the substrate bias has been demonstrated as an effective means in modifying the structural and magnetic properties of $SmCo_5$ thin films.

2.5.3 Effects of other seed layers

Chen et al. (2008) and Zhang et al. (2009a) found that Ta seed layer is better than Ti seed layer for Sm-Co thin films grown on Cu underlayer, in terms of $SmCo_5$ (0001) texture and crystallization, as well as the out-of-plane intrinsic coercivity of the $SmCo_5$ film (higher than 20 kOe). Those improvements were correlated to the smoother Cu underlayer with (111) texture on Ta underlayer of proper thickness (4 nm), possibly because of higher melting point of Ta (2996 °C) than Ti (1668 °C), and the large surface energy of Ta layer.

2.5.4 Microstructures of $SmCo_5$ thin films with perpendicular anisotropy on Cu (111) underlayer

Through Auger electron spectroscopy (AES) analysis, Sayama et al. (2006a) showed that Cu atoms were diffused up to the Sm-Co layer from the Cu underlayer, which was suggested to be strongly related with the appearance of the perpendicular magnetic anisotropy by introducing the Cu underlayer.

Takahashi et al. (2006) investigated the microstructure of $SmCo_5$ thin films deposited on Cu, Cu/Ti and Pt underlayers, by cross-section TEM with energy filtered elemental map and energy dispersive x-ray spectroscopy line analysis. $SmCo_5$ films developed a strong (0001) texture on the Cu/Ti underlayers, which showed strong Cu (111) texture, and mixed orientations of $SmCo_5$ ($1\bar{1}00$) and (0002) on the Pt underlayer, which did not have strong Pt (111) texture. The grain size of the Cu underlayer is about 200 nm and that of the $SmCo_5$ is also very large (~200 nm). Fig. 2.11 shows the cross-

section TEM image of the $SmCo_5$ film on the Cu/Ti underlayer. The layer structure of the film is clearly seen.

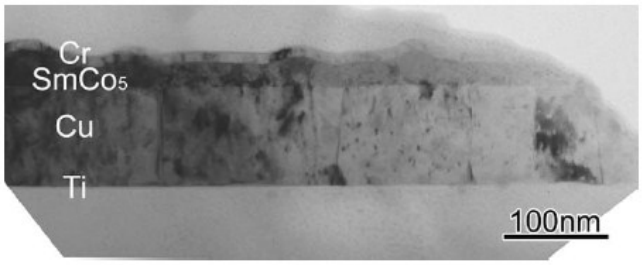

Figure 2.11 Cross-section TEM image of the $SmCo_5$ film deposited on the Cu/Ti underlayer. [Takahashi et al. 2006]

Fig. 2.12 shows the intensity profiles of each element. Arrows (a) and (b) in the Co map correspond to the two orthogonal scanning directions. The intensity profiles show that Cu substitutes for Co and diffuses into the $SmCo_5$ layer to form a $Sm(Co, Cu)_5$ solid solution. There are fluctuations of Cu concentrations with a scale length of 40 nm along the in-plane direction in the $Sm(Co, Cu)_5$ layer, which are believed to cause local changes in the magnetocrystalline anisotropy. This gives rise to the pinning force for the magnetic domain wall motion, which was used to explain the high coercivity of the $SmCo_5$ film grown on the Cu underlayer. On the other hand, a two-layer structure of $SmCo_5$ thin film consisted of a crystallized bottom layer and an amorphous upper layer, was formed on Pt underlayer with imperfect Pt (111) texture (having other planes parallel to the film plane, such as (220), (311), etc.). Crystallized $SmCo_5$ grains showed both $(1\bar{1}00)$ and (0002) orientations. no large compositional fluctuations were observed in the $SmCo_5$ bottom layer that contained Pt. The upper $SmCo_5$ layer remained amorphous because of the insufficient dissolution of Pt. These observations were used to explain the low coercivity of the $SmCo_5$ film grown on the Pt underlayer.

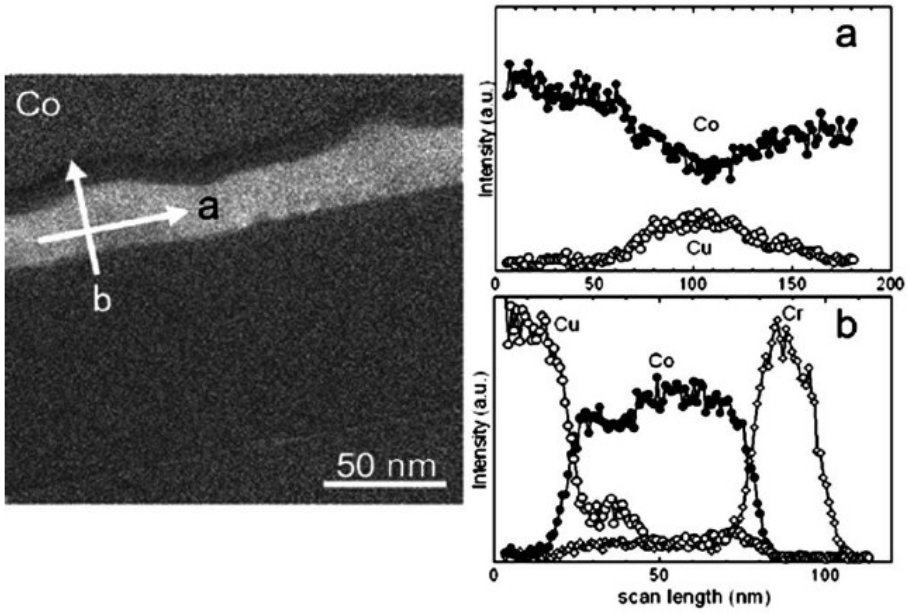

Figure 2.12 Energy filtered Co map obtained from the cross-sectional image of the $SmCo_5$ layer deposited on the Cu/Ti underlayer and EDS intensity profiles of Cr, Co, and Cu along two orthogonal analysis directions shown as (a) and (b). [Takahashi et al. 2006]

There are two kinds of defects that could pin the domain wall motion, depending on the anisotropy (crystalline or magnetoelastic) of the defect relative to that of the matrix, as shown in Fig. 2.13 (Fig. 9.12 in O'Handley 2000). A nonmagnetic or low-anisotropy defect reduces the local wall energy and can be visualized as an "Energy Well" in domain wall energy - spatial position chart, while a high-anisotropy defect increases the local wall energy and can be represented an "Energy Barrier". In the report of Takahashi et al. (2006), it was implied that the $Sm(Co, Cu)_5$ grains in $SmCo_5$ film deposited on Cu/Ti underlayer serve as energy wells, not energy barriers, to domain wall motion, because the magnetocrystalline anisotropy of $Sm(Co, Cu)_5$ is known to decrease with increasing Cu content (Lectard et al. 1994). So this is true only if the Sm-Co regions around the $Sm(Co, Cu)_5$ grains are crystalline $SmCo_5$ phase. In fact, the $Sm(Co, Cu)_5$ grains could also be the energy barriers for domain wall motion in $Sm(Co, Cu)_5$ films, as reported by Zhao et al. (2012).

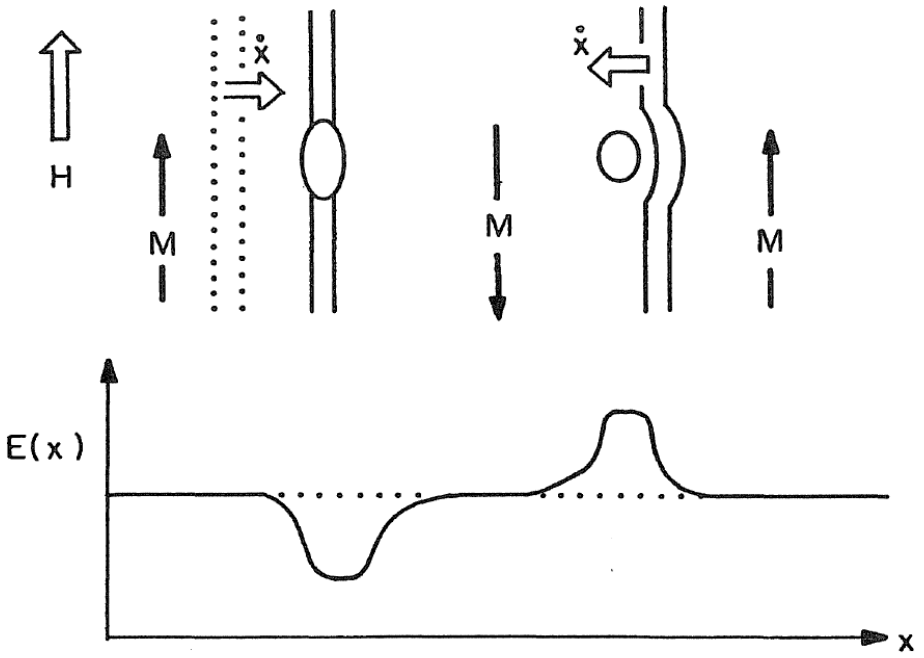

Figure 2.13 Upper panel depicts two kinds of defect and their influence on wall motion for vertical applied field: nonmagnetic inclusions locally lower the wall energy by decreasing its area; particles of different anisotropy or magnetization than the matrix present a barrier to wall motion. Below is shown the domain wall energy as a function of position in the absence of an applied field. [Figure 9.12 of O'Handley 2000]

Another interesting finding in the study of Takahashi et al. (2006) is the roughness of $SmCo_5$ layer. All underlayers (Cu, Cu/Ti, and Pt) showed very smooth interfaces with the $SmCo_5$ layer, because of the substrate used in the study are thermally oxidized Si substrates. But the fully crystallized $SmCo_5$ layers on Cu and Cu/Ti underlayers are very rough, as shown by many bumps (thicker regions of the $SmCo_5$ layer). These bumps often coincide with a $Sm(Co, Cu)_5$ grain at the bottom of $SmCo_5$ layer, suggesting that the rough surface is correlated to the formation of $Sm(Co, Cu)_5$ grains.

The discovery of non-uniform Cu diffusion along the film plane from the Cu underlayer into the $SmCo_5$ thin films is extremely important, because it means the local composition of Sm-Co-Cu layer is not controllable. This makes the Cu underlayer out of choice in the potential application of $SmCo_5$ thin film as perpendicular recording media.

Other underlayers without such non-uniform diffusion have to be used. A good candidate is Ru underlayer as discussed in later sections.

2.6 Sm(Co, Cu)$_5$ Alloys with Large Uniaxial Magnetic Anisotropy

2.6.1 Stability of Sm(Co, Cu)$_5$ ternary alloys

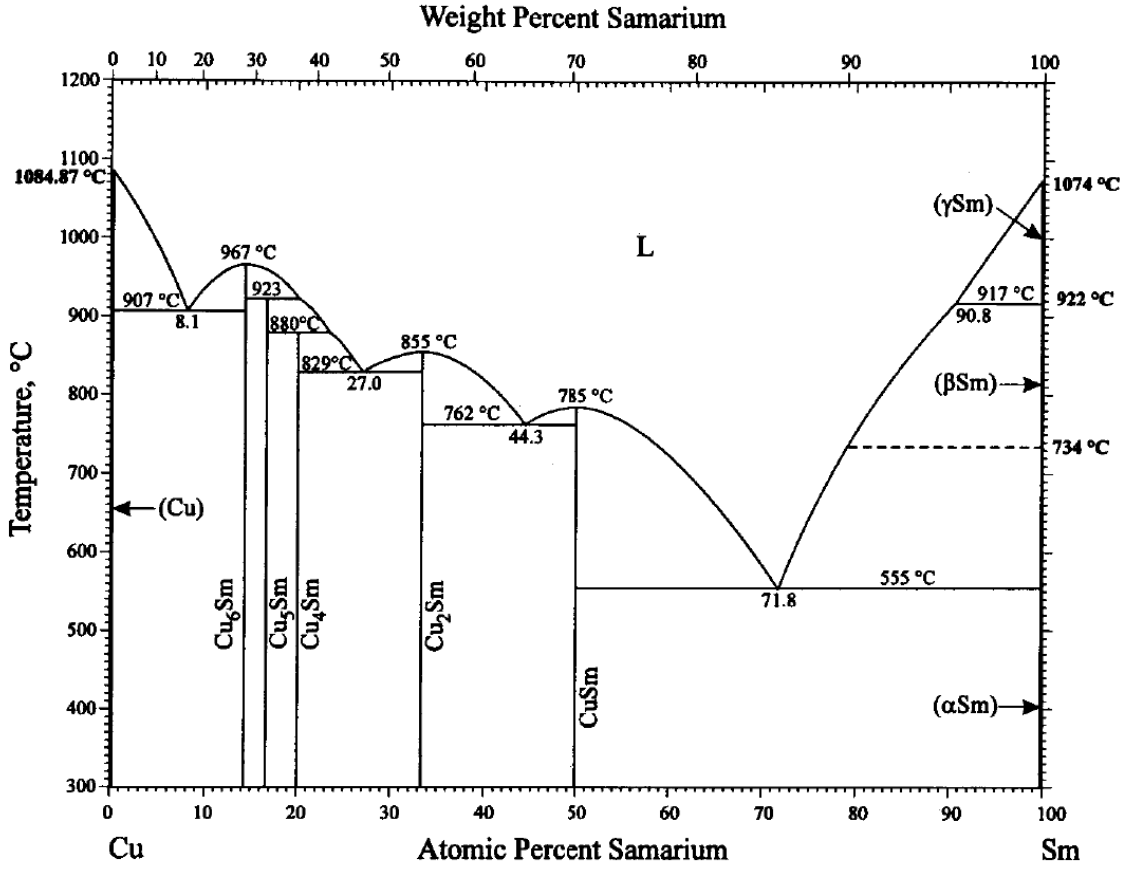

Figure 2.14 Cu-Sm binary phase diagram. [Okamoto 1998]

Cu has a negligible solubility in Co below 400 °C, and the solubility is less than 5 at.% even at 800 °C, according the Co-Cu binary phase diagram (SGTE and Franke et al.). According to Bodak and Fabrichnaya (2007), the ternary phase $Sm(Co_{1-x}Cu_x)_5$ is stable for the whole range of $x \in (0, 1)$ when the temperature is above 800 °C. This is

related to the fact that the Sm-Cu alloy system also has a $SmCu_5$ phase which has the same $CaCu_5$ structure as $SmCo_5$ phase, and the $SmCu_5$ phase is thermodynamically stable below 923 °C, as shown in Fig. 2.14. Unlike the Sm-Co system, there is no "Sm_2Cu_{17}" or "Sm_5Cu_{19}" phase on the Cu-rich or Sm-rich side of $SmCu_5$. This may be one reason that Cu-doping in Sm-Co alloy stabilizes the $SmCo_5$ phase, but makes the Sm_2Co_{17} phase unstable, as seen in the experimental studies, such as Perry et al. (1977).

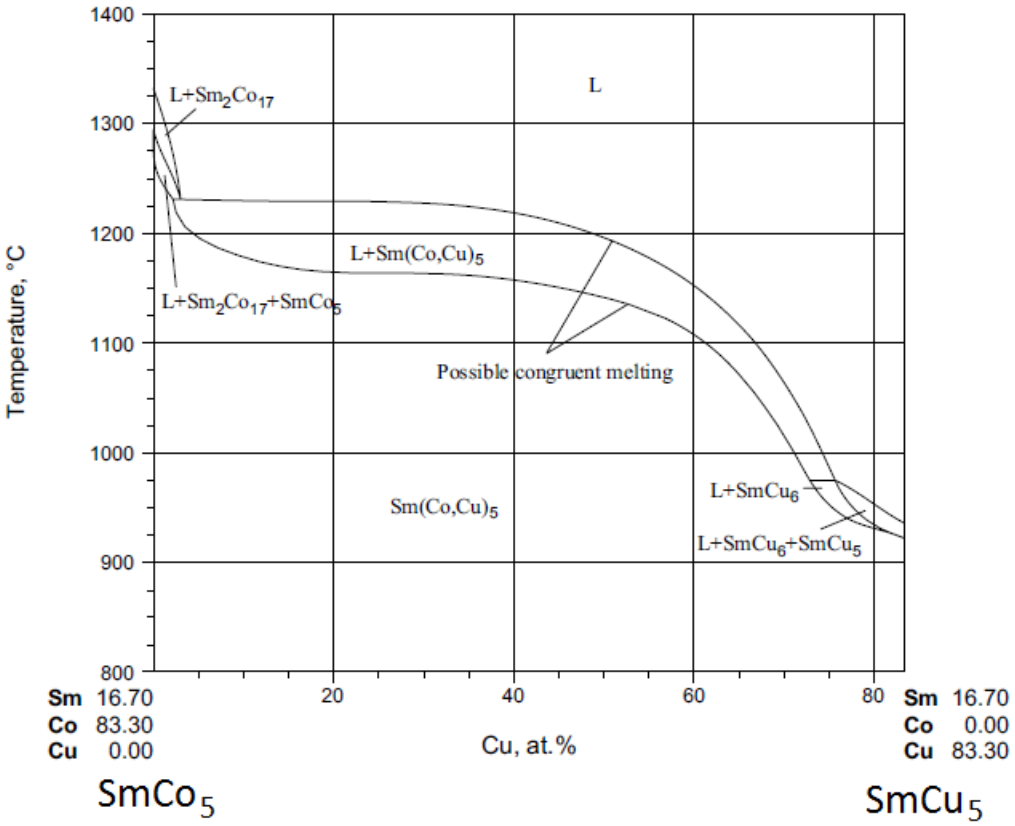

Figure 2.15 $SmCo_5$-$SmCu_5$ pseudobinary phase diagram. [After Bodak and Fabrichnaya 2007]

The $SmCo_5$-$SmCu_5$ pseudobinary phase diagram given by Bodak and Fabrichnaya (2007) is shown in Fig. 2.15. It is seen that the melting point of $Sm(Co_{1-x}Cu_x)_5$ decreases about 100 °C with ~ 5 at.% of Cu, and remains nearly unchanged up to ~ 40 at.% of Cu, before fast decreases to that of $SmCu_5$. This is consistent with the decrement of the crystallization temperature of Sm-Co due to the addition of Cu seen in both bulk alloys

(Oesterreicher et al. 1979) and films (Prados and Hadjipanayis 1998, and Yamazaki et al. 1998).

On the stability of $Sm(Co_{1-x}Cu_x)_5$ phase at lower temperature (<= 800 °C), some early studies (e.g. Hofer 1970, Katayama et al. 1973, and Kamino et al. 1973) reported a possible spinodal decomposition into two $Sm(Co_{1-x}Cu_x)_5$ phases (one Co-rich and the other Cu-rich), in the as-cast state or upon heat treatment. Other studies (e.g. Perry et al. 1977 and Meyer-Liautaud et al. 1987), however, concluded that complete solubility should be expected between $SmCo_5$ and $SmCu_5$, as evidenced by a linear increase of the lattice constants with increasing Cu content and the extended solid solutions at 400 °C. More recent studies (e.g. Téllez-Blanco et al. 1998, Estevez-Rams et al. 1999, and Gabay et al. 2005) also observed the microsegregation in as-cast $Sm(Co_{1-x}Cu_x)_5$ alloys by SEM and thermomagnetic analysis. The segregated components are still of $CaCu_5$ structure, but have a randomly varying transition metal composition, which cannot be distinguished with powder XRD. Subsequent annealing at 800 - 1000 °C removed this variation in stoichiometry.

2.6.2 **Structural and magnetic properties of $Sm(Co, Cu)_5$ alloys**

The $Sm(Co_{1-x}Cu_x)_5$ alloys exhibits a large magnetic anisotropy for Cu contents up to $x = 0.5$. A fairly complete set of data on the structural and magnetic properties of $Sm(Co, Cu)_5$ alloys covering nearly the whole composition range can be found from the reports of Lectard et al. (1994) and Téllez-Blanco et al. (1998). Fig. 2.16 shows the x dependence of the saturation magnetization (M_s) and the anisotropy field (H_A) of $Sm(Co_{1-x}Cu_x)_5$ phases at 300 K. The Curie temperature (T_C), exchange constant (A), and anisotropy constant (K_1) at 300 K of $Sm(Co_{1-x}Cu_x)_5$ phases as a function of x are shown in Fig. 2.17.

The saturation magnetization M_s decreases and vanishes for $SmCo_2Cu_3$ at 300 K. Similar decrease of the Curie temperature T_c versus $_x$ is observed. When Cu doping (x) is larger than 0.35, the anisotropy field (H_A) shows a strong decrease. For lower Cu contents ($x < 0.35$), anisotropy fields are very large, which makes difficult the accurate determination of the substitution effect. The first anisotropy constant K_1, calculated using

the available values of H_A and M_s, shows a linear decrease from $SmCo_5$ to $SmCo_2Cu_3$. The interpolated K_1 values of $SmCo_4Cu_1$ and $SmCo_3Cu_2$ are about 10 and 5 ($\times 10^7$ erg/cm^3), respectively, which are still comparable to that of the $L1_0$-phase FePt (~7.0 $\times$ 10^7 erg/cm^3).

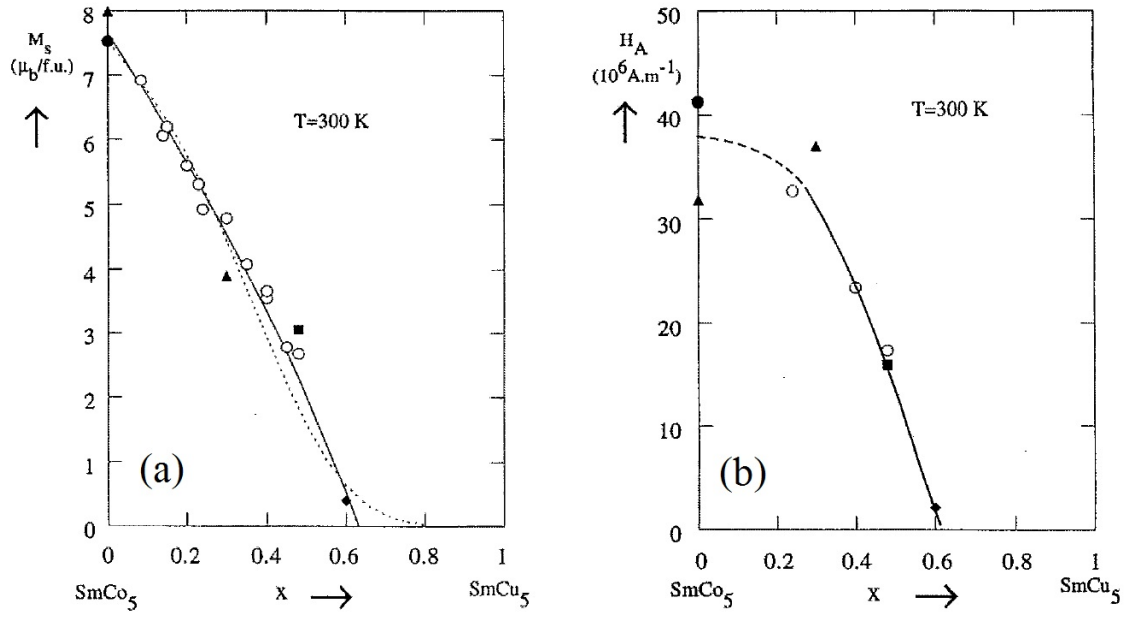

Figure 2.16 (a) The *x* dependence of the saturation magnetization (M_s) of $Sm(Co_{1-x}Cu_x)_5$ phases at 300 K. Dashed line: simulated variation using the Jaccarino-Walker model (five neighbors). (b) The anisotropy field (H_A) of $Sm(Co_{1-x}Cu_x)_5$ phases at 300 K. [Lectard et al. 1994]

The composition dependence of the lattice parameters *a* and *c* and volume of the cells of annealed $SmCo_{5-x}Cu_x$ alloys from Téllez-Blanco et al. (1998) agree well with previous studies (e.g. Nishida et al. 1974 and Meyer-Liautaud et al. 1987). The differences in lattice parameters and Curie temperature between annealed and as-cast alloys were explained by a change of actual Cu content in the $SmCo_{5-x}Cu_x$ alloys before and after annealing (assuming that not all Cu entered into the $SmCo_5$ lattice in as-cast alloys, as discussed in section 2.6.1).

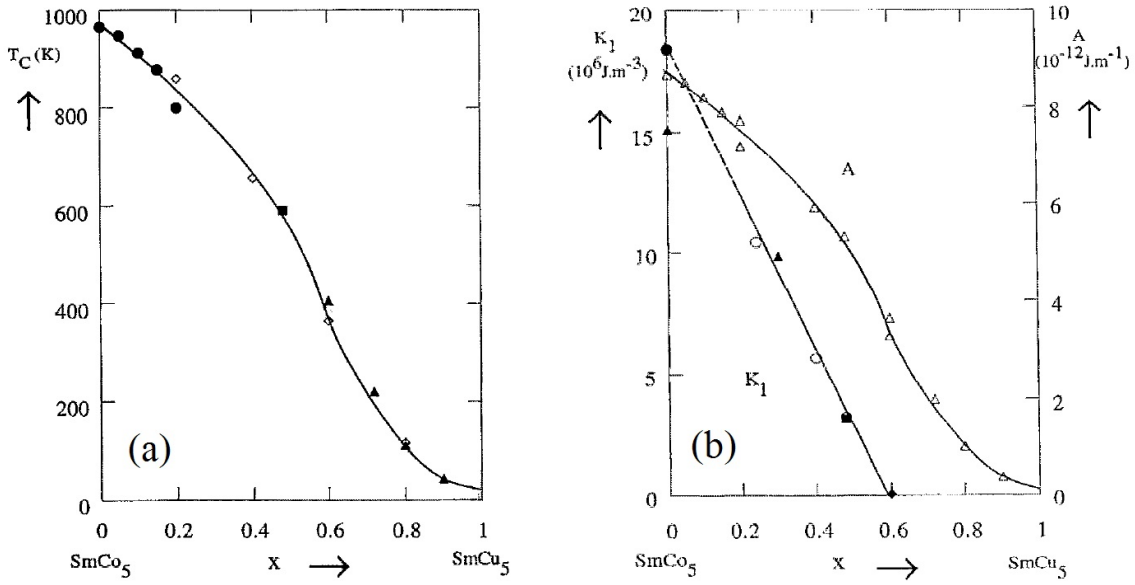

Figure 2.17 (a) The Curie temperature (T_C) of $Sm(Co_{1-x}Cu_x)_5$ phases as a function of x. (b) The anisotropy constant (K_1) at 300 K and exchange constant variations vs. x in $Sm(Co_{1-x}Cu_x)_5$ phases. [Lectard et al. 1994]

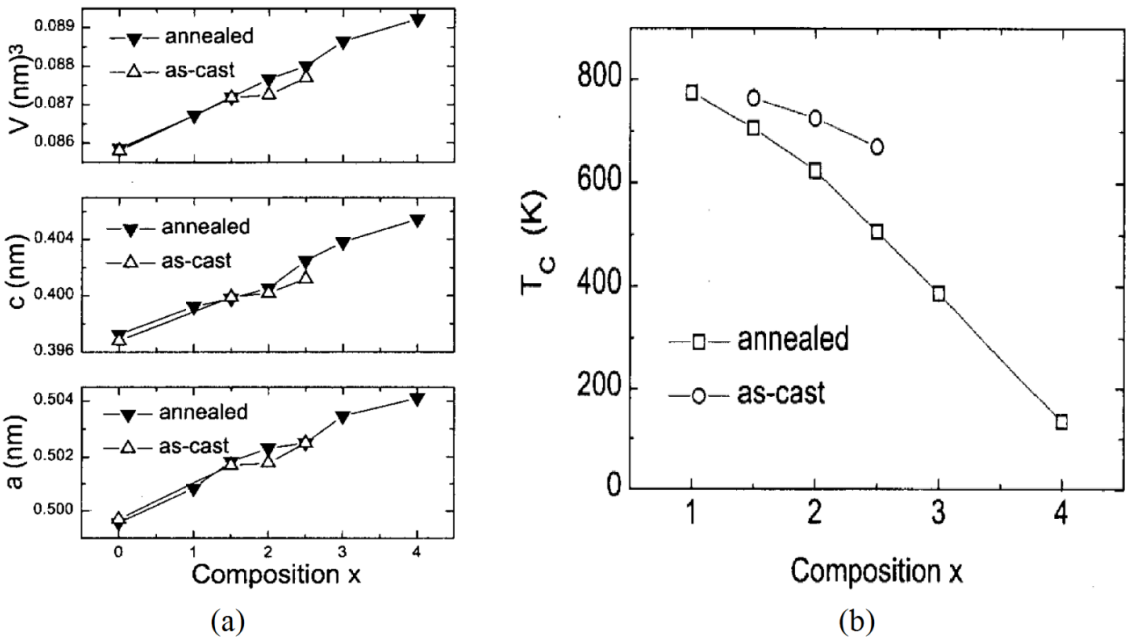

Figure 2.18 (a) The composition dependence of the lattice parameters a and c and volume of the cells of $SmCo_{5-x}Cu_x$ alloys determined at room temperature. (b) The concentration dependence of the Curie temperature of $SmCo_{5-x}Cu_x$ compounds. [Téllez-Blanco et al. 1998]

The data of structural and magnetic properties of $Sm(Co, Cu)_5$ alloys serve as a reference in the understanding of these properties of $Sm(Co, Cu)_5$ thin films. For example, film composition can be deduced from the Curie temperature, or the stress/strain state of a $Sm(Co, Cu)_5$ thin film can be evaluated from the differences in lattice constants from the alloy with the same composition.

2.6.3 Site preference of Cu in $Sm(Co, Cu)_5$ phase

There are two Co sites, i.e., Co(2c) and Co(3g), in the $SmCo_5$ crystal structure, and doping at different Co sites may result in different values of properties such as the exchange coupling constants, T_c, and magnetocrystalline anisotropy constant. There is no concrete experimental evidence in the literature on the determination of whether there is a site preference when Cu is doped into $SmCo_5$ phase. For example, Nishida et al. (1974) found a change in saturation magnetization of $SmCo_{5-x}Cu_x$ in the concentration range $x < 2$ is linear, but that in the range $x > 2$ is not linear, which seem to suggest that Cu substitution in $SmCo_5$ occurs preferentially at the layers together with Sm atoms. From the X-ray measurements, however, it is not clear whether $SmCo_3Cu_2$ has an ordered lattice or not, since the integrated reflection for as-cast and annealed specimens shows no difference, i.e., the difference between the values of atomic scattering factor for Co and Cu is small.

Predictions using different methods based on first-principles theory also gave different results. Sabirianov et al. (2004) conducted the first-principles study of transition-metal substitutions in Sm-Co permanent magnets. Their calculation using the Vienna *ab initio* simulation package (VASP) found that Cu substituting Co(2c) sites has much lower solution energy than substituting Co(3g) sites. This suggests that Cu substitution prefers 2c sites. Another report from Gabay et al. (2005) calculated the total chemical energy of $SmCo_{5-x}Cu_x$ as a function of x with the full-potential, linearized augmented plane wave (LAPW) method using the WIEN2k code. The calculations suggested that the Cu atoms prefer the 2c sites for any x value if the $SmCo_{5-x}Cu_x$ phase is chemically stable. However, the result could be problematic because it also predicted the

decomposition of $SmCo_{5-x}Cu_x$ into $SmCo_5$ and $SmCu_5$, which is not supported by XRD and thermomagnetic analysis. One suggested reason for the discrepancy is that only chemical energy of each phase was considered in the calculations, while the transformation might be suppressed in the real alloy due to positive changes of the elastic strain energy. Chen et al. (2012a) also studied the site preference of Cu in $Sm(Co, Cu)_5$ phase by simulations based on first-principles theory for the exchange interaction of $SmCo_4Cu$ crystal. It was suggested that Cu doping in $SmCo_4Cu$ should occur primarily at Co(2c) sites, because the total exchange correlation J_0 of $SmCo_4Cu$(2c) is less than that of $SmCo_4Cu$(3g), according to calculation results using the open source package Material eXplorer (OpenMX), combined with a linear combination of atomic orbits (LCAO) based on density functional theory.

One the other hand, the calculations of magnetic moments of $SmCo_{5-x}Cu_x$ as a function of Cu doping, based on the first-principles theory using a highly accurate DFT code VASP package including the LDA+U formalism, suggest that the Cu atoms prefer the Co(3g) sites for any *x* value (Chen et al. 2012b).

According to an unpublished work by Sun et al. (2010), the highly (0001) textured $Sm(Co, Cu)_5$ thin films were investigated by extended x-ray absorption fine structure (EXAFS) spectroscopy at Cu *K*- and Co *K*- edges, respectively. The primary results suggested that the model of Cu randomly substituting Co sites gave the best fit of experimental data. However, this conclusion may be questionable, because the $Sm(Co, Cu)_5$ thin films in this study are not single-crystalline films. In fact, there are both crystalline and amorphous regions in these films (Zhao et al. 2012). Therefore, it is still an open question for if there is a site preference of Cu doping in $Sm(Co, Cu)_5$ crystals, and what it is if yes.

2.7 $Sm(Co, Cu)_5$ Thin Films with Perpendicular Anisotropy Fabricated by Direct Doping of Cu

2.7.1 $Sm(Co, Cu)_5$ thin films formed by $[Sm/Co/Cu]_n$ multilayer deposition on Ti\Cu underlayer

While the Cu diffusion from the Cu underlayer into the Sm-Co layer which helps reducing the crystallization temperature of $SmCo_5$ thin films by forming the ordered $Sm(Co, Cu)_5$ phase was generally studied and recognized by various research groups, Sayama et al. (2006a) also studied the effect of Cu addition into the Sm-Co layer by laminating additional Cu sublayers into the Sm/Co multilayer, and found that it enhanced the perpendicular magnetic anisotropy and reduced the Cu underlayer thickness required to obtain the squareness ratio of unity. The natural next step of the study would be the direct doping/alloying of Cu into the Sm-Co layer, and checking its effect on crystallization, structural and magnetic properties of $Sm(Co, Cu)_5$ thin films.

2.7.2 $Sm(Co, Cu)_5$ (0001) thin films grown on Ta\Ru (0002) underlayer

The first studies of co-sputtering Cu together with Sm and Co elemental targets, were reported by Liu et al. (2008a and 2008b). To exclude the effect of Cu diffusion from underlayers and achieve smaller grain size in underlayer, a Ta\Ru underlayer was employed in this study. The Ta\Ru underlayer is well known to form an excellent Ru (0002) texture at room temperature, and is widely being used in conventional CoCrPt-oxides-based perpendicular magnetic recording media (Shi et al. 2005). Considering the same hcp structure and close lattice constants in the (0001) planes between CoCrPt and $SmCo_5$, it is expected that $SmCo_5$ thin films with (0001) texture can be grown hetero-epitaxially on Ru underlayer with (0002) texture. In this paper, it reported that highly textured $Sm(Co, Cu)_5$ (0001) thin films on Ru (0002) underlayer were successfully fabricated by dc magnetron sputtering, as shown in Fig. 2.19 (a). Strong perpendicular anisotropy was obtained with the squareness ratio of 1, zero in-plane coercivity, and 11 kOe out-of-plane coercivity. It is worth noting that the deposition temperature of Sm-Co-

Cu layer is 350 °C, significantly lower than that of $SmCo_5$ films with good perpendicular anisotropy grown on Ru buffered single-crystal α-Al_2O_3 (0001) substrate (700 °C, see Seifert et al. 2009). Crystallization of Sm(Co, Cu)$_5$ thin film is significantly dependent on film composition and substrate temperature. Sm(Co, Cu)$_5$ phase may form only when the Cu/Co ratio is about 1:3 or more, at the substrate temperature of 350 °C. The film with the highest Cu/Co of 1:2 and the highest substrate temperature of 350 °C in this study gave the best Sm(Co, Cu)$_5$ (0001) texture and perpendicular anisotropy. The thickness dependence of Sm(Co, Cu)$_5$ thin film showed the largest perpendicular coercivity at 10 nm. Thinner or thicker both would lead to smaller perpendicular coercivity. This dependence was explained by combining the effects of grain agglomeration and the existence of magnetic dead layer at the interface between Sm-Co-Cu layer and Ru underlayer.

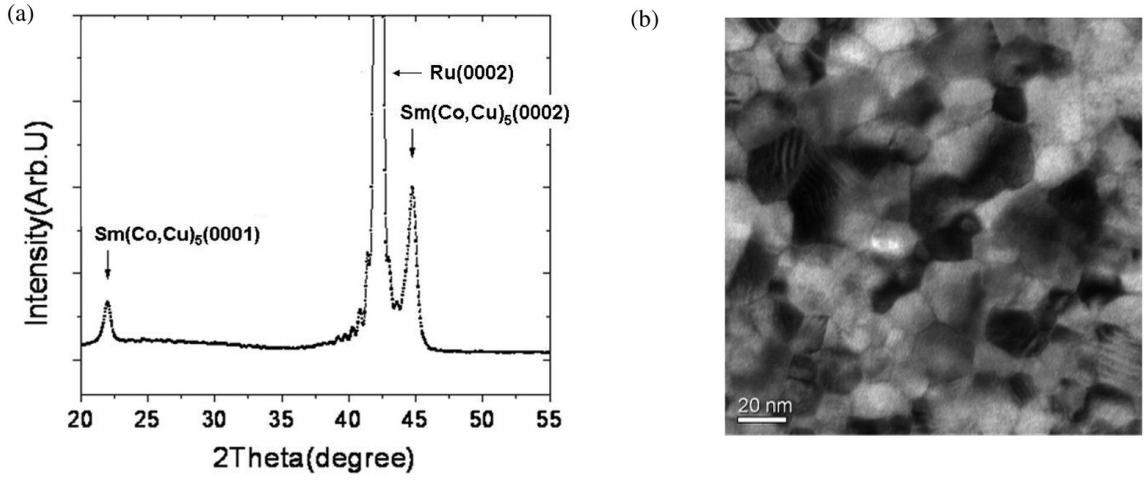

Figure 2.19 (a) XRD spectrum and (b) Plane-view TEM image of the sample: Glass\ Ta(4.2 nm)\ Ru-1(16 nm)\ Ru-2(4 nm)\ $Sm_{14}Co_{58}Cu_{28}$ (10 nm)\ Ta(3 nm). [Liu et al. 2008a]

The plane-view TEM image showed in Fig. 2.19 (b) was claimed in this paper to represent the microstructure of the $Sm_{14}Co_{58}Cu_{28}$ thin film. However, a later report by Zhao et al. (2012) suggested that those small faceted crystalline grains (10-30 nm in size) are Ru grains, instead of Sm(Co, Cu)$_5$ grains. Grain sizes in Ru underlayer are indeed

much smaller than that of Cu underlayer (~ 100 nm), as expected. The Sm-Co-Cu layer contains voids (not completely continuous) and is mainly in the form of crystalline grains embedded in an amorphous matrix, where inhomogeneous composition across the film plane existed. Fig. 2.20 showed such compositional variation in the HAADF image and elemental mapping of a typical $Sm(Co, Cu)_5$ thin films with Ta\Ru underlayers (Zhao et al. 2012).

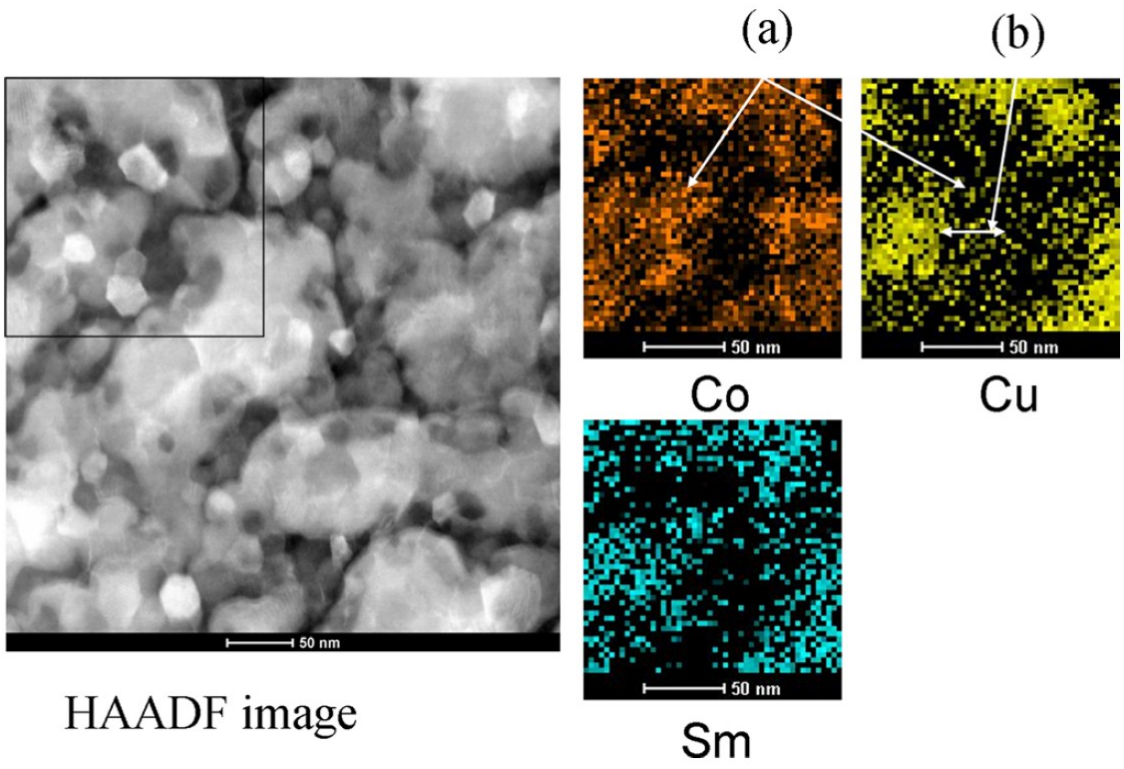

Figure 2.20 HAADF image and elemental mapping of Sm(Co, Cu)5 thin film (20 nm) with Ta\Ru underlayers. The upper-left square box in the HAADF image indicates the region which was elementally mapped, and shown on the right. [Zhao et al. 2012]

The magnetization reversal mechanism of $Sm(Co, Cu)_5$ (0001) thin films on Ru (0002) underlayer was identified to be domain-wall pinning, based on initial curves of magnetic hysteresis loops and angular dependence of coercivity (H_c) and remanence coercivity (H_{cr}) measurement. The composition variation of $Sm(Co, Cu)_5$ films is

believed to be the dominant pinning factor. A model based on lateral graded anisotropy due to composition/crystallization variation was proposed to explain the relatively small H_c (11 kOe) comparing with H_K (> 200 kOe), as shown in Fig. 2.21. More detailed characterizations of microstructure and pinning sites of the $Sm(Co, Cu)_5$ layer and calculations based on this model will be discussed in Chapter 4 of this thesis.

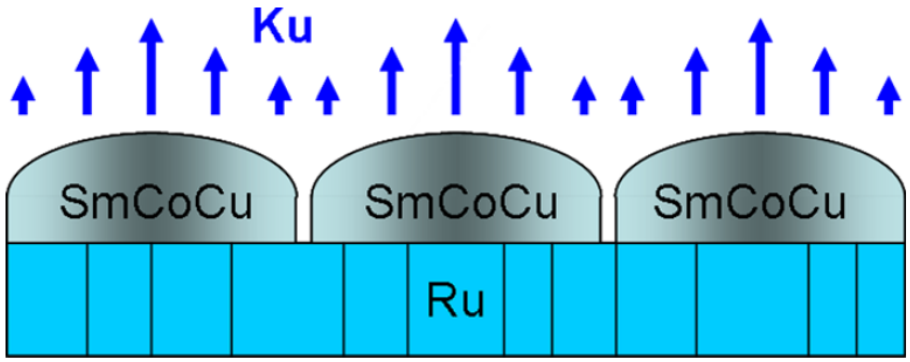

Figure 2.21 Schematic drawing of a $Sm(Co, Cu)_5$ thin film with lateral graded anisotropy grown on the Ru underlayer. The variation of the length of arrows represents the variation of perpendicular anisotropy of $Sm(Co, Cu)_5$ regions. [Zhao et al. 2012]

Liu et al. (2008b) attempted to use Ru(Cr) as the underlayer for Sm-Co-Cu thin films, in order to reduce the lattice mismatch between the atomic distance of Ru-Ru in the plane of Ru (0002) (~2.706 Å) and Co-Co in the plane of $SmCo_5$ (0001) (~2.501 Å), and to expect better crystallization of the Sm-Co-Cu layer and higher perpendicular anisotropy. Another motivation was that, if Cr was over-doped, some of the Cr atoms might diffuse into Ru grain boundaries to induce the growth of small and isolated Ru grains. XRD results showed that $Sm(Co, Cu)_5$ (0001) texture was seen on all Ru(Cr) underlayers. The addition of Cr reduced the lattice constants of Ru(Cr) underlayer continuously up to the highest Cr concentration in the study (~61.3%). It seems no over-doping of Cr was observed. Magnetic hysteresis loops in the out-of-plane direction indicated poorer perpendicular anisotropy as the Cr doping increased. This paper suggested that a slightly larger lattice misfit may be better for the growth of $Sm(Co, Cu)_5$ (0001) texture.

Yin et al. (2013) reported a study on the effects of a wider range of Cu doping on the crystalline structure and magnetic properties of $SmCo_{5-x}Cu_x$ (x = 0, 1, 2, 3, 4, and 5) thin films grown on Ru (0002) underlayer. Clear transitions of phases in these films from Co or Sm_2Co_{17} (x = 0), to nearly single phase of $SmCo_3Cu_2$ and $SmCo_2Cu_3$ (x = 2 and 3), and to $SmCu_5$ phase (x = 5), were observed. Compared with a previous study (Zhao et al. 2012), higher substrate temperature (380 °C vs. 350 °C) and lower Ar pressure (2 mTorr vs. 3 mTorr) should have helped crystallization of the $SmCo_{5-x}Cu_x$ thin films with x = 0 and 1. Curie temperature (T_c) of the $SmCo_{5-x}Cu_x$ (x = 0, 1 and 2) thin films decreases with the Cu doping. The M-T curve of $SmCo_3Cu_2$ thin film suggests a mixture of two phases with different T_c values (~700 K and ~450 K) co-exists.

2.7.3 Sm-Co-Cu thin films on TiW\Cu underlayer

Cheng et al. (2012a and 2012c) also studied the direct Cu doping effect on the structural and magnetic properties of Sm-Co-Cu thin films. A new Ti_3W_7 seed layer was employed in these studies with the Cu underlayer. The reported Cu (111) texture grown on Ti_3W_7 seed layer is much worse than that on a Ti or Ta seed layer, as those reported in the literature. This could be the reason the crystallization of Sm-Co-Cu thin films was poor, and no $Sm(Co, Cu)_5$ (0001) texture was obtained in the films of these studies. For the as-deposited Sm-Co-Cu thin films, the highest out-of-plane coercivity is ~3.7 kOe, and the squareness ratio is less than 0.9.

2.8 Other Topics on $SmCo_5$ Thin Films with Perpendicular Anisotropy

2.8.1 $SmCo_5$ thin films with perpendicular anisotropy on single crystal substrate

$SmCo_5$ thin film with an out-of-plane texture and in-plane orientation can be epitaxially grown on proper single crystal substrate with proper buffer layer(s). Here we

review only the $SmCo_5$ thin film with perpendicular anisotropy, i.e. (0001) texture. Table 2.2 lists the studies reported in the literature.

Table 2.2 Studies of $SmCo_5$ thin films with perpendicular anisotropy grown on single crystal substrate.

Substrate	Buffer layer(s)	$SmCo_5$ thickness	Capping layer	Preparation method	T_{dep}_$SmCo_5$ (°C)	Reference
α-Al_2O_3 (0001)	Co(2 nm) \Cu(10 nm)	20 nm	None	MBE	500	Nukaga et al. 2008
α-Al_2O_3 (0001)	None, Co (5 nm), Ru (5 nm), or Co(2 nm) \Cu(10 nm)	20 nm	None	MBE	500	Ohtake et al. 2009b
α-Al_2O_3 (0001)	Co(2, 5 nm) \Cu(10 nm)	20 nm	None	MBE	500	Ohtake et al. 2009a
α-Al_2O_3 (0001)	Co(2 nm) \Cu(2-100 nm)	20 nm	None	MBE	500	Ohtake et al. 2010.
α-Al_2O_3 (0001)	Ru (20 nm)	100 nm	Cr (10 nm)	PLD	550-800	Seifert et al. 2009

Nukaga et al. (2008) and Ohtake et al. (2009a, 2009b, and 2010) studied mainly the $SmCo_5$ thin films grown on α-Al_2O_3 (0001) single crystal substrate with a Co\Cu buffer layer. Two types of possible epitaxial orientation relationship can be described as follows:

Type A - $SmCo_5(0001)\langle 1\bar{1}00\rangle$ // $Cu(111)\langle 11\bar{2}\rangle$ // $Al_2O_3(0001)\langle 1\bar{1}00\rangle$;

Type B - $SmCo_5(0001)\langle 11\bar{2}0\rangle$ // $Cu(111)\langle 11\bar{2}\rangle$ // $Al_2O_3(0001)\langle 1\bar{1}00\rangle$.

A schematic drawing of the two relationships is shown in Fig. 2.22 (Adapted from Fig. 3 of Ohtake et al. 2009a). The lattice misfits (or mismatch) are about -2.3% and +12.8% in Type A and B, respectively. The orientations of these two types of $SmCo_5$ domains are rotated around film normal by 30 degrees to each other. This is sometimes called a bi-crystalline structure (Ohtake et al. 2009b). Given the large lattice misfit of Type B, it seems unlikely for $SmCo_5$ to develop this epitaxial relationship on Cu underlayer. However, the bi-crystalline structure was indeed seen in the RHEED observations (Nukaga et al. 2008) and in-plane XRD spectra (Ohtake et al. 2010) of $SmCo_5$ thin films. It is not very clear about why the Type B domains developed on Cu underlayer. One

possible reason may be related to the Cu diffusion into the $SmCo_5$ from the Cu underlayer and the formation of $Sm(Co, Cu)_5$ alloy. The composition of $Sm(Co, Cu)_5$ alloy is estimated to be $Sm(Co_{0.5}Cu_{0.5})_5$ based on the lattice constants measured by out-of-plane and in-plane XRD in a later study (Ohtake et al. 2010). In another study of Ohtake et al. (2009a), it was reported that a $SmCo_5$ (0001) single-crystal film was successfully obtained by introducing a thin Co seed layer (5 nm) on Cu (111) underlayer (10 nm). The nucleation of $SmCo_5$ crystal on Cu underlayer seems to be controllable by varying the interaction between the Cu underlayer and the $SmCo_5$ layer.

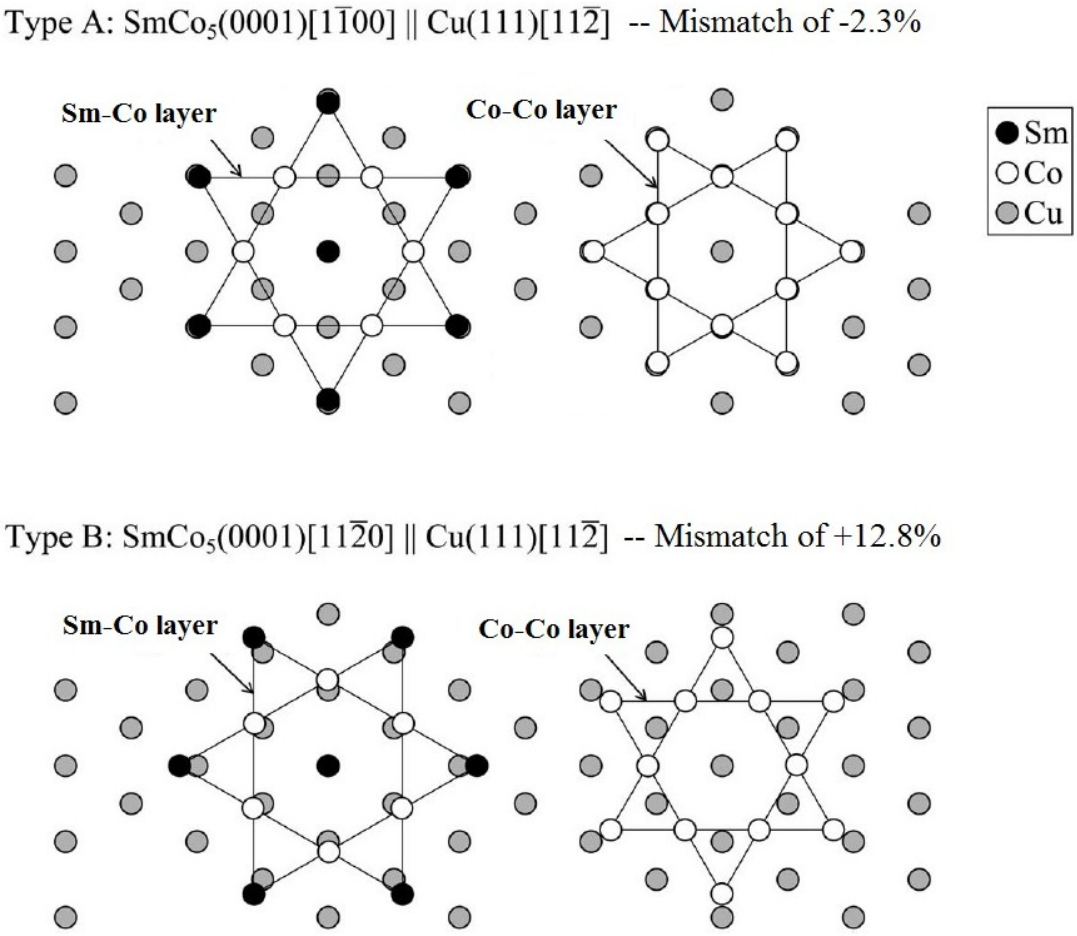

Figure 2.22 Two types of epitaxial orientation relationship between $SmCo_5$ (0001) crystal and Cu (111) underlayer. [Adapted from Ohtake et al. 2009a]

Ohtake et al. (2009b) also reported that Sm-Co thin film forms amorphous layers on Ru (0001) and Co (0001) underlayers as well as when the film is deposited directly on an Al_2O_3 (0001) substrate. Ohtake et al. (2010) studied the effects of substrate temperature and Cu underlayer thickness on the crystallographic properties of $SmCo_5$ (0001) epitaxial films on Al_2O_3 (0001) substrate. This study reinforced the understanding of Cu underlayer effect in that Cu atoms are considered to have diffused from the underlayer into the $SmCo_5$ layer to form an alloy compound of $Sm(Co, Cu)_5$. Cu underlayer helps reducing the crystallization temperature of $SmCo_5$ thin films by forming the ordered $Sm(Co, Cu)_5$ phase.

A similar observation of two different crystallographic orientations was also claimed by Seifert et al. (2009), where a Ru (0001) buffer layer (20 nm) was employed between $SmCo_5$ (0001) and α-Al_2O_3 (0001) single crystal substrate, and higher substrate temperature (~ 700 °C) was used. The misfits of Type A and B of $SmCo_5$ (0001) with the Ru (0001) layer are -7.7% and 6.6%, respectively. It is easier to understand that both types are seen in this study, since the misfits are smaller than 10%.

Table 2.3 Structural and magnetic properties of $SmCo_5$ (0001) thin films grown on single crystal α-Al_2O_3 (0001) substrate.

Buffer layer(s)	$SmCo_5$ thickness	Capping layer	T_{dep} (°C)	Lattice Constant (Å)	Magnetic properties of $SmCo_5$ thin film	Reference
Co(2 nm) \Cu(10 nm)	20 nm	None	500	a = 5.035; c = 4.045.	N.A.	Ohtake et al. 2010.
Ru (20 nm)	28 nm	Cr (10 nm)	700	a = 4.945; c = 4.021.	Ms = 788 emu/cm^3, Hc = 13.5 kOe, Ku = 7.6 × 10^7 erg/cm^3, (BH)max = 22.5 MGOe.	Seifert et al. 2009

Table 2.3 summarizes the structural and magnetic properties of $SmCo_5$ (0001) thin films grown on single crystal α-Al_2O_3 (0001) substrate. Lattice constants of $SmCo_5$ thin film with Ru buffer layer are smaller than those with Cu buffer layer, which is expected

because of Cu inter-diffusion effect. Compared to those of the bulk $SmCo_5$ as given in Table 2.1, lattice constants of $SmCo_5$ thin film with Ru buffer layer are smaller in *a*, but larger in *c*. This implies in-plane compressive stresses exist in the of $SmCo_5$ (0001) thin films with Ru buffer layer. This result further suggests that only the epitaxial relationship of Type B should have happened in these films, since Type A would only produce tensile stresses in the film. Similar compressive stresses are also observed in $Sm(Cu, Co)_5$ (0001) thin films grown on Ru polycrystalline underlayer (as discussed in Chapter 3).

No magnetic properties of the $SmCo_5$ thin films grown on α-Al_2O_3 (0001) single crystal substrate with a Cu buffer layer were reported by Nukaga and Ohtake. One reason may be because all these $SmCo_5$ thin films may have no capping layer for the protection of oxidation and corrosion, and might be easily oxidized or corroded in the normal lab environment. The saturation magnetization (Ms) of $SmCo_5$ (0001) thin film grown on Ru buffered single crystal α-Al_2O_3 (0001) substrate is almost same as its bulk value, but its anisotropy constant (Ku) is smaller than those reported bulk values ($1.1 - 2.0 \times 10^8$ erg/cm^3), although it is still twice as large as that grown on Ti\Cu buffered glass substrate (Sayama et al. 2004a). The main reason is probably the imperfections/defects in these $SmCo_5$ thin films, which showed a pinning dominated magnetization reversal mechanism in this study, as compared to nucleation dominated reversal mechanism in bulk $SmCo_5$ magnets. It is observed that the $SmCo_5$ thin films in this study should contain a compressive strain, as evidenced by the decreased lattice constant *a* and increased lattice constant *c* (as compared to the bulk values in Table 2.1). As discussed before, the magnetic anisotropy of $SmCo_5$ depends on the crystal effective field of the lattice. It is possible that the compressively strained $SmCo_5$ in the lattice constant *a* direction may have different magnetic anisotropy than the bulk alloy with the same composition. It is also reported that the *c*-axis texture and perpendicular magnetic anisotropy improve further for films with smaller thickness. This implies that proper compressive strain might help improve perpendicular anisotropy in $SmCo_5$ films because thinner films should experience large compressive strain.

2.8.2 $SmCo_5$ thin film with perpendicular anisotropy grown on a NiW underlayer

Without the direct doping of Cu in Sm-Co layer, many efforts in fabricating $SmCo_5$ thin films with perpendicular anisotropy on the underlayers other than Cu failed (e.g. Ni, Co, Pd, Pt, Al, and Au in Morisako et al. 2006a, and Pt in Takahashi et al. 2006), even though the lattice mismatch between $SmCo_5$ (0001) plane and the proposed epitaxial (111) planes of the underlayers are small. One reason is the poor or no (111) texture of these underlayers, which do not have a proper seed layer. Another important reason is that the crystallization temperature of $SmCo_5$ is very high, mainly due to poor mobility of large Sm atoms. But if the deposition temperature of $SmCo_5$ is enough high, underlayers other than Cu can be used to induce $SmCo_5$ (0001) texture too. The $SmCo_5$ (0001) thin films grown on Ru buffered single crystal α-Al_2O_3 (0001) substrate discussed in previous sections is a good example, where the substrate temperature needs to be around 700 °C.

Zhang et al. (2010a and 201b) reported another example, in which $SmCo_5$ thin films showing good (0001) texture were achieved on a W\$Ni_4$W(211) underlayer or a W\$Ni_4$W(211)\Ni(111) underlayer on glass substrates, with the sputtering deposition temperature of 500–530 °C. The glass substrate type is not given, but should be one kind of high-temperature glass substrates, whose strain point should be higher than 550 °C (the highest deposition temperature in the study). Large out-of-plane coercivity (~15 kOe) and very low in-plane coercivity are observed. Poorer crystallinity and smaller out-of-plane coercivity were seen for the sample prepared at a slightly higher deposition temperature (550 °C), which was explained the W diffusion from the 20 nm thick W cover layer into the $SmCo_5$ layer, based on the composition depth profile measured by SMIS. No detailed microstructure and micro-composition analysis were given in the reports. It is not clear if there were any Ni diffusion happened at the interface as well.

2.8.3 Oxidation and corrosion protection of $SmCo_5$-based thin films with perpendicular anisotropy

Chapter 2. Review of Studies on $SmCo_5$-Based Thin Films for Magnetic Recording

SmCo magnets have a strong resistance to oxidation and corrosion, and usually do not need to be coated for applications in high temperature and poor working conditions (http://www.china-magnet.net/smco.html). SmCo thin films, however, are much more susceptible to oxidation and corrosion than bulk magnets because of larger surface-to-volume ratio.

There were not many reports on the anti-corrosion control issue of SmCo thin films. Zana et al. (2001) investigated the long-term stability of Co–Sm thin films, both with no overcoat and covered with silicon nitride layers of varying thickness, and found that bare Co–Sm films exhibit an accelerated decrease in magnetization with respect to reference Co–Pt films, while silicon nitride layers of about 8 nm should provide adequate protection against degradation of the magnetic properties of Co–Sm thin films. Sayama et al. (2005a) reported a result that the Sm–Co film formed by laminating Sm and Co sub-layer alternately possesses a corrosion resistance as much as a CoCr film by electrochemical analysis. Morisako et al. (2006a) found that, for almost all the Sm-Co films (15 - 40 nm), the coercivities of these films almost did not change with duration of nearly 3 years at ambient atmosphere, even though those films do not have any protection layer.

Zhao et al. (2011) conducted an accelerated corrosion test (130 °C, 95% RH, 6 h), where the test conditions are common for the qualification of hard disk recording media, on the $Sm(Co, Cu)_5$ thin films with a Ta (3 nm) capping layer, which were stable in normal laboratory environment (25 °C, 50% RH) for over 3 years. Severe Co oxidation and corrosion were observed after test treatment. It is clear that the corrosion resistance of the $Sm(Co, Cu)_5$ thin film is not enough for current recording media application. Even a Ta (3nm) capping layer is not able to provide sufficient protection. In magnetic recording application, the non-magnetic protection layer over the magnetic recording layer should be as thin as possible to reduce signal loss. In current commercial perpendicular recording media, the thickness of carbon overcoat (which provides wear and corrosion protection) is now 2 nm or less. Therefore, novel ideas on the effective ways of protecting $SmCo_5$-based thin films without sacrificing magnetic signal strength

are needed. At the end of this paper, hcp-phased CoPt-alloys were proposed as capping materials for $Sm(Co, Cu)_5$ thin films in future high-density magnetic recording applications.

2.8.4 Recording characteristics of $SmCo_5$-based thin films with perpendicular anisotropy

Although the microstructure of $SmCo_5$-based thin films is far away from meeting the key requirements of good perpendicular magnetic recording media, one group of researchers from Waseda University already started pioneering studies on the integration of a $SmCo_5$ recording layer and a soft underlayer (SUL), and on recording characteristics of the $SmCo_5$ recording layer with (double-layered media) or without the SUL.

Osaka et al. (2007) studied the fabrication and recording performance of $SmCo_5$-based double-layered perpendicular media with a SUL of Co-Zr-Nb. A Ru buffer layer introduced between a Cu/Ti intermediate layer and a Co-Zr-Nb soft magnetic underlayer is found to be necessary to achieve perpendicular magnetic anisotropy. It is no surprise to find that the medium noise of their $SmCo_5$ double-layered media was high compared with commercial media. One useful finding is that the media noise at high linear density could be reduced by depositing the Sm-Co layer under high Ar gas pressure, which is also consistent with the reduced magnetic cluster size (from 145 nm to 125 nm) at an AC-demagnetized state of these media.

Another report (Asahi et al. 2008) from the same group of researchers tried using C doping into Cu underlayer to reduce the magnetic domain size in the $SmCo_5$ layer. It was found that only a very small amount of C doping, less than 0.20 at.%, had beneficial effects on magnetic properties of the media as seen in reduced magnetic domain size without a large decrease in squareness ratio. C doping more than that may lead to poorer $SmCo_5$ (0001) texture. The optimized C doping at 0.20 at.% led to decreasing medium noise and increasing of SNR, but the overall SNR are still too low (~ 8 dB at 600 KFCI).

The latest study from the Waseda Univ. group on reducing the magnetic cluster sizes of $SmCo_5$ thin films was reported by Sugiyama et al. (2010). After studying the Cu-Ta_2O_5

and Cu-SiO_2 underlayers and realizing the adverse effects of metal oxides on the magnetic properties of thin Sm-Co layer, they developed a Sm-Co-CrTa granular layer between the Sm-Co continuous layer and the Cu underlayer of recording media, expecting a layer configuration as shown in Fig. 2.15. It is not clear if the expected layer configuration was truly achieved in their films, because there were no cross-section TEM analysis results reported. The authors claimed that the addition of CrTa into the Co layer induces the decreasing of inter-granular exchange interaction in the Sm-Co continuous layer, but also admitted that the isolation of Co-CrTa is not sufficient in this study so that the $SmCo_5$ and the CrTa in the Sm-Co-CrTa layer were not perfectly segregated.

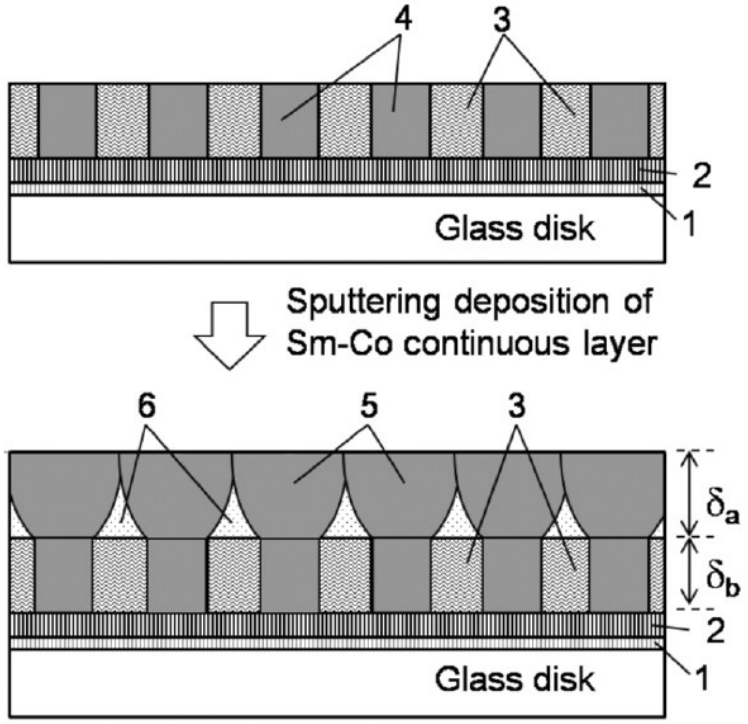

Figure 2.23 Expected layer configuration for a sample after deposition of Sm-Co continuous layer. 1: Ti layer, 2: Cu layer, 3 and 4: CrTa rich phase and Sm-Co rich phase in Sm-Co-CrTa multilayer, respectively, 5: Crystallized SmCo phase by the diffusion of Cu, 6: amorphous-like SmCo phase which exhibits low magnetic anisotropy. [Sugiyama et al. 2010]

In summary, recording media made of $SmCo_5$ thin films with perpendicular anisotropy on Cu(111) underlayer were studied by the Waseda Univ. group. Large grain

sizes / magnetic cluster sizes of the recording media is the main issue discussed in these studies. Despite various efforts being tried, no clear solution is available or foreseeable to solve this issue up to now.

2.9 Future Development of $SmCo_5$-based Thin Films for Magnetic Recording Media Application

As reviewed in above sections, of the three major challenges faced by the $SmCo_5$ thin films in the application of ultimate high-density magnetic recording, the orientation control of $SmCo_5$ thin film has achieved significant progresses. Large perpendicular anisotropy (comparable to the $L1_0$-phase FePt) can be achieved in Sm(Co, Cu)$_5$ (0001) thin films. Therefore, this challenge can be deemed as largely solved, while some improvements are still wanted, such as better crystallization and homogeneity of the Sm(Co, Cu)$_5$ (0001) thin films. For the other two challenges, there were not many significant achievements up to now. They should be the focus of future research effort. Some thoughts on addressing these issues are discussed below.

2.9.1 Better crystallization and homogeneity of the Sm(Co, Cu)$_5$ (0001) thin films

As discussed in section 2.7.2, even in the highly (0001) textured Sm(Co, Cu)$_5$ thin films grown on Ta\Ru (0002) underlayer, there are amorphous matrix and regions with inhomogeneous composition. Optimizing the sputtering parameters, such as deposition pressure (lower) and temperature (higher), should help improve the crystallization. Using a composite target of Sm-Co-Cu instead of co-sputtering of three elemental targets may help with the homogeneity. Lastly, biasing sputtering may be combined to improve the film quality.

2.9.2 **Magnetic cluster control for conventional magnetic recording**

For the magnetic cluster control, the general requirements are small and uniform grain size of magnetic grains, which are largely exchanged-decoupled, and with a narrow distribution of perpendicular anisotropy. The key is to find a proper material, which can segregate from $Sm(Co, Cu)_5$ phase during co-sputtering with the main elements (Sm, Co, and Cu) to form non-magnetic boundaries. A natural candidate could be Zr, which has been widely used in Sm-Co magnets and is known to form a boundary phase. Common oxides (such as SiO_2, Ta_2O_5, etc.) may have adverse effect on the magnetic properties of Sm-Co thin films, as reported by Sugiyama et al. (2010), probably due to the large enthalpy of formation of Samarium oxide (Sm_2O_3). In this sense, the Sm_2O_3 itself may be considered as the boundary material. Doping boundary materials may affect the crystallization of main $Sm(Co, Cu)_5$ phase. Therefore, proper deposition parameters for each boundary material may be different.

2.9.3 **Anti-corrosion control**

In principle, there are two means that can help improve the corrosion resistance of $SmCo_5$-based thin film media, without increasing the magnetic spacing between the recording head and recording media. One is use a magnetic overcoat which has a stronger intrinsic corrosion resistance, such as CoCrPt-based materials used in current perpendicular recording media. This has been proposed in Zhao et al. (2010).

Another way is to improve the intrinsic corrosion resistance of $SmCo_5$ by doping with the proper element(s), which would not adversely affect the anisotropy constant, or at least would not cause too much of the decrease of the anisotropy constant. A potential candidate is Ni, because $Sm(Co, Ni)_5$ is known to have comparable anisotropy field as $Sm(Co, Cu)_5$ for the same amount of Ni or Cu doping, both at cryogenic temperature (e.g. Foner et al. 1978 and Oesterreicher 1978) and room temperature (Pratos and Hadjipanayis 1999). Ni is known to have excellent corrosion resistance in most environments. So the corrosion resistance of $Sm(Co, Ni)_5$ is expected to be better than

that of $Sm(Co, Cu)_5$. How much improvement that $Sm(Co, Ni)_5$ can provide should be verified. Note that $Sm(Co, Ni)_5$ or Ni may be considered as the magnetic overcoat as well.

Chapter 3. Fabrication of $Sm(Co, Cu)_5$ (0001) Thin Film with Perpendicular Anisotropy

Summary

In this chapter, fabrication and characterization of polycrystalline Sm–Co–Cu films with highly (0001) textured $Sm(Co, Cu)_5$ grains were described. Sm–Co–Cu films with variable composition were prepared by DC magnetron co-sputtering of Sm, Co, and Cu elemental targets on highly (0002) textured and smooth Ru or Ru(Cr) underlayers. Good perpendicular anisotropy of $Sm(Co, Cu)_5$ thin films has been achieved, such as the out-of-plane coercivity of 11 kOe, the nearly zero in-plane coercivity, the squareness ratio of 1 in the out-of-plane direction, and the estimated perpendicular magnetic anisotropy constant of $3.3\sim5.8 \times 10^7$ erg/cm^3. Effects of deposition temperature, film composition, and Sm-Co-Cu layer thickness on the magnetic properties of $Sm(Co, Cu)_5$ films were investigated. Composition of crystalline $Sm(Co, Cu)_5$ grains estimated from Curie Temperature matches reasonably well with that from lattice unit volume. Strain state of crystalline $Sm(Co, Cu)_5$ grains was also studied. The effect of Cr doping in Ru underlayer on structural and magnetic properties of $Sm(Co, Cu)_5$ films was investigated. A proper Cr doping could improve the perpendicular anisotropy of $Sm(Co, Cu)_5$ films.

3.1 Introduction

$SmCo_5$ alloy has been extensively studied as a permanent magnet material since the 1960s (e.g. Das 1969). The study of amorphous Sm–Co films as magnetic recording media appeared as early as 1984 (Kullmann et al.) for longitudinal magnetic recording. $SmCo_5$ thin films with large in-plane anisotropy can be easily grown on Cr underlayer at elevated temperature. However, they had never been considered in longitudinal magnetic recording, partly because their in-plane coercivity is usually too large (> 10 kOe) for the write element in the recording head to record. Perpendicular magnetic recording

technology using soft underlayer (SUL) gives a larger writing field and allows the use of magnetic recording materials with higher anisotropy than longitudinal recording. The concept and application of exchange-coupled composite (ECC) media in perpendicular recording further increases the upper-limit on the anisotropy constant of magnetic recording layer. New recording technologies based on perpendicular recording, such as domain-wall assisted recording and heat- or energy- assisted magnetic recording (HAMR or EAMR), could even eliminate the upper-limit on the anisotropy constant of magnetic recording layer. The development of these new technologies spurred the study of $SmCo_5$ thin films with large perpendicular anisotropy.

At the time (early 2007) when we started our study on $SmCo_5$ thin films for future magnetic recording media application, it had been found that $SmCo_5$ thin films with good perpendicular anisotropy can be grown on Cu (111) underlayer (Sayama et al. 2004a and Takei et al. 2004). The microstructure and micro-composition analysis of such films (Takahashi et al. 2006) showed significant Cu diffusion at the interface between Cu underlayer and $SmCo_5$ layer, suggesting the formation of $Sm(Co, Cu)_5$ phase, which may have a lower crystallization temperature. However, the Cu diffusion also led to compositional inhomogeneity and rough surfaces of $SmCo_5$ thin films. Another issue with the use of Cu underlayer is its large average grain size (>100 nm). Conventionally the grain size of the magnetic recording layer is controlled by the grain size of the underlayer, due to epitaxial growth relationship between them. If the grain size of $SmCo_5$ layer is same as the Cu underlayer, it will not meet the requirements for high-density magnetic recording application. The large average grain size of Cu underlayer relates to the relatively low melting point of Cu (1085 °C). With the doping of Cr (Morisako et al. 2006a and 2006b), the average grain size can be reduced to ~ 40 nm, which is still too large. Therefore, many underlayers other than Cu (e.g. Co, Ni, Pd, Pt, etc.) had been tried to grow $SmCo_5$ thin film with perpendicular anisotropy, but none worked without the help of Cu (e.g. Morisako et al. 2006a). New underlayer with small grain size was highly wanted at that time.

In the meantime, the Ta\Ru underlayer is well known to form an excellent Ru (0002) texture at room temperature, and is widely being used in conventional CoCrPt-oxides-based perpendicular magnetic recording media (Shi et al. 2005). The melting point of Ru is as high as 2330 °C, which leads to a much smaller average grain size than Cu when deposited as a thin film at room temperature. In addition, considering the same hcp structure and close lattice constants in the (0001) planes between CoCrPt and $SmCo_5$, it is expected that $SmCo_5$ thin films with (0001) texture can be grown hetero-epitaxially on Ru underlayer with (0002) texture. Further literature search found that the $Sm(Co_{1-x}Cu_x)_5$ alloys exhibit a large magnetic anisotropy for Cu contents up to $x = 0.5$ (as introduced in Section 2.6.2). On the ground of this knowledge and understanding and the finding of the formation of $Sm(Co, Cu)_5$ phase on Cu underlayer, we proposed and successfully fabricated highly textured $Sm(Co, Cu)_5$ (0001) thin film with large perpendicular anisotropy on the Ta\Ru underlayer, by co-sputtering Sm, Co, and Cu targets.

Experimental details on the fabrication and characterization of $Sm(Co, Cu)_5$ (0001) thin films are described in Section 3.2. Typical structural and magnetic properties of Sm-Co-Cu films grown on the Ta\Ru underlayer as well as the effects of deposition temperature, film composition, and film thickness are discussed systematically in Section 3.3. The lattice mismatch between the atomic distance of Ru–Ru in the plane of Ru (0002) (~2.706 Å) and Co–Co in the Co(3g) plane of $SmCo_5$ (0001) (~2.501 Å) is about 8%. Doping the smaller atom Cr into Ru lattice was expected to make the lattice mismatch smaller, and hence better epitaxial growth of the $Sm(Co, Cu)_5$ (0001) thin film on the Ru (0002) underlayer. In Section 3.4, the study of the crystalline structures and magnetic properties of Sm–Co–Cu thin films grown on Ru(Cr) underlayers is reported. Section 3.5 includes further discussions on composition of $Sm(Co, Cu)_5$ grains, and the epitaxial growth between $Sm(Co, Cu)_5$ (0001) layer and Ru (0002) underlayer. Section 3.6 is the conclusion.

3.2 Fabrication and Characterization of $Sm(Co, Cu)_5$ (0001) Thin Films

The Sm-Co-Cu thin films with the layer structure of Ta(4.2 nm)\[Ru or Ru(Cr)] (20 nm)\Sm-Co-Cu(*x* nm)\Ta(3 nm) (*x* = 5, 10, 15, 20) were deposited on glass substrates by using a home-built eight-target dc magnetron sputtering system as introduced in Chapter1. The base pressure of this system was less than 1×10^{-7} Torr. The working gas (Ar) pressure was 3 mTorr. The Ru(Cr) underlayers were formed by co-sputtering of Ru and Cr targets at 3 mTorr. The bottom Ta layer was deposited for texture control and the cap Ta layer was deposited as a protective layer against oxidation. The composition and thickness of Sm–Co–Cu layer were controlled by sputtering power and time during the co-sputtering of Sm, Co, and Cu targets. The thickness of the Sm–Co–Cu magnetic layer ranged from 5 to 20 nm. The deposition temperature of Sm-Co-Cu layer and Ta capping layer controlled by heating the substrates ranges from 150 to 350 °C. All other layers were prepared at room temperature.

Magnetic properties of the films were characterized by a vibrating sample magnetometer (VSM) and superconducting quantum interference device (SQUID). The crystallographic texture of the films was investigated by X-ray diffraction (XRD) with Cu K_α radiation. Transmission electron microscopy (TEM) and Rutherford backscattering spectroscopy (RBS) were used to study the structure and composition of Sm-Co-Cu films.

There are two types of average compositions for the Sm-Co-Cu thin films in this study: nominal composition and RBS composition. Since the Sm-Co-Cu thin films in this study were prepared by co-sputtering of Sm, Co, and Cu elemental targets, the composition of Sm-Co-Cu thin films can be adjusted by using different sputtering power of each target. The nominal film composition is calculated from the sputtering power of each elemental target, by using the calibrated sputter deposition rate and molar volume of each element. The average composition measured by RBS may be different from the nominal composition due to errors from the calibration of sputter-deposition rate, non-ideal molar volume, or the fitting of RBS data, etc.

3.2.1 Composition of Sm-Co-Cu thin films measured by RBS

Generally speaking, RBS method will give a better estimation of the composition of Sm-Co-Cu thin films than the method using sputter deposition rate and molar volume. However, one big issue in the determination of Sm composition by RBS for films with current layer structure is the impact of Ta underlayer. Ta has a larger atomic weight than Sm, which means a larger energy of backscattered Helium ions from Ta than from Sm, if they were in the same depth of the film. But since there is a Ta underlayer in our film structure, the energy of backscattered He ions from Ta underlayer will be decreased due to layers on top of it, and fall close to that from Sm. This may lead to a large uncertainty in the estimation of Sm atom content. This issue can be avoided by preparing coupon samples for RBS measurement with Sm-Co-Cu thin films of the same composition without the Ta underlayer.

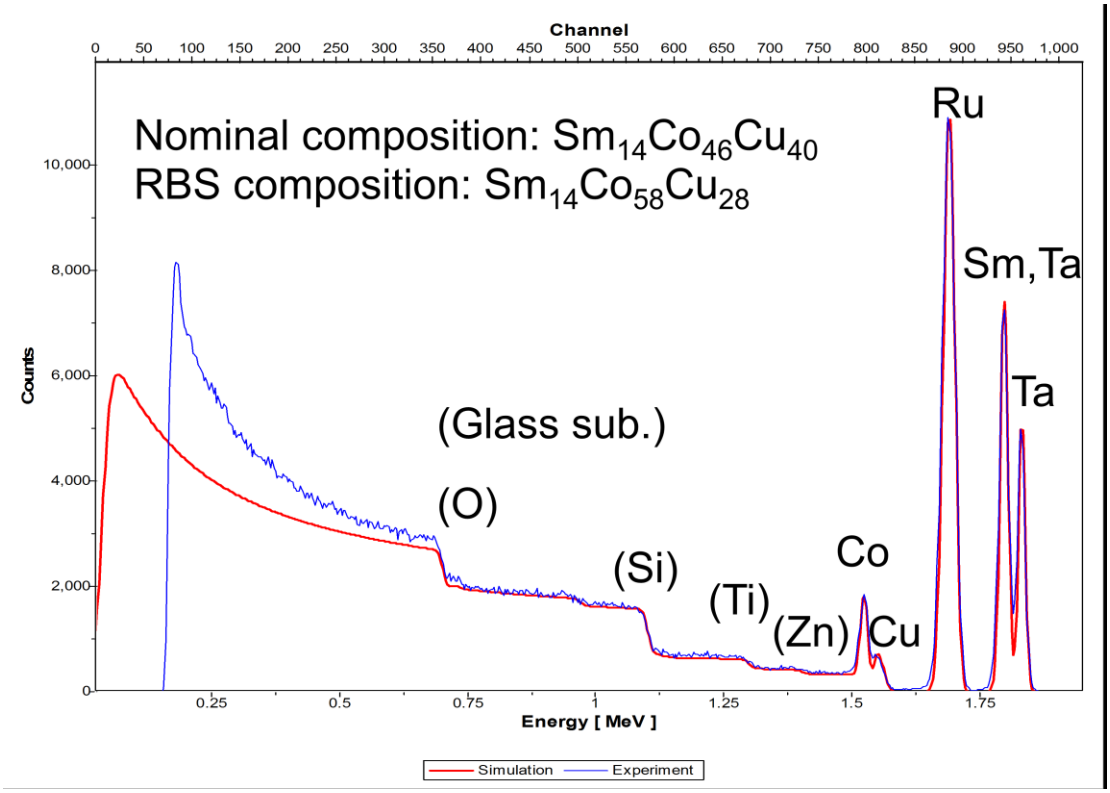

Figure 3.1 The experimental and simulated RBS spectra of the sample with the structure of Glass\Ta(4.2 nm)\Ru (20 nm)\Sm-Co-Cu(10 nm)\Ta(3 nm).

Still there is a way to minimize the uncertainty caused by Ta underlayer in the fitting of RBS data. This is because the layer structure of our Sm-Co-Cu thin films also contains a Ta capping layer, and the layer thickness ratio between the Ta capping layer and Ta underlayer is just the ratio of deposition time of each layer (which are known in sample preparation), because these two layers were deposited under same sputtering conditions. The error in deposition time is small (less than 2.5%) for Ta layers in our experiment. The amount of Ta capping atoms can be accurately calculated in RBS spectrum because it is a single peak. Therefore, the amount of Ta underlayer atoms can also be determined.

Fig. 3.1 shows the experimental and simulated RBS spectra of the sample with the structure of Glass\Ta(4.2 nm)\Ru (20 nm)\Sm-Co-Cu(10 nm)\Ta(3 nm). Both the nominal and RBS compositions of the Sm-Co-Cu layer are showed for comparison. The Co/Cu ratio in RBS composition may be underestimated because of imperfect fitting, which could arise from inhomogeneous distribution of Cu in the film.

3.3 $Sm(Co, Cu)_5$ (0001) Thin Films on Ta\Ru Underlayer

3.3.1 Typical structural and magnetic properties

Fig. 3.2 shows the XRD spectra and magnetic hysteresis loops of a typical sample glass\Ta(4.2 nm)\Ru(20 nm)\Sm-Co-Cu(20 nm)\Ta(3 nm) with a good $Sm(Co, Cu)_5$ texture and perpendicular anisotropy. The substrate temperature for the deposition of Sm-Co-Cu layer is 350 °C. The composition of this Sm–Co–Cu layer was determined to be $Sm_{14}Co_{58}Cu_{28}$, based on RBS analysis. There were only $Sm(Co, Cu)_5$ (00. *l*) and Ru (00. *l*) peaks observed in the normal θ - 2θ scan, and only (*h k*. 0) peaks in the in-plane scan, as seen in Fig. 3.2 (a) and (c). These results strongly suggested that a $Sm(Co, Cu)_5$ thin film with very good (0001) texture was formed. Further investigation on the rocking curves of $Sm(Co, Cu)_5$ (0002) and Ru (00002) peaks showed that both peaks have a small $\Delta\theta_{50}$ value of 3.1^o, as seen in Fig. 3.2 (b). Therefore, it was concluded that $Sm(Co, Cu)_5$ thin films in this study are highly (0001) textured. The results shown in Fig. 3.2 (d) confirmed the perpendicular magnetic anisotropy and also indicated that it is far away from

saturation along the hard axis (in-plane direction) under an applying field of 70 kOe, which is consistent with the expected high H_K in $Sm(Co, Cu)_5$ alloy. The kink in the in-plane loop matches the drop of moment at low fields in the out-of-plane loop, which could be due to misoriented $Sm(Co, Cu)_5$ grains and short-range ordered or amorphous SmCoCu components in the $Sm(Co, Cu)_5$ thin film. The perpendicular coercivity is about 8 kOe.

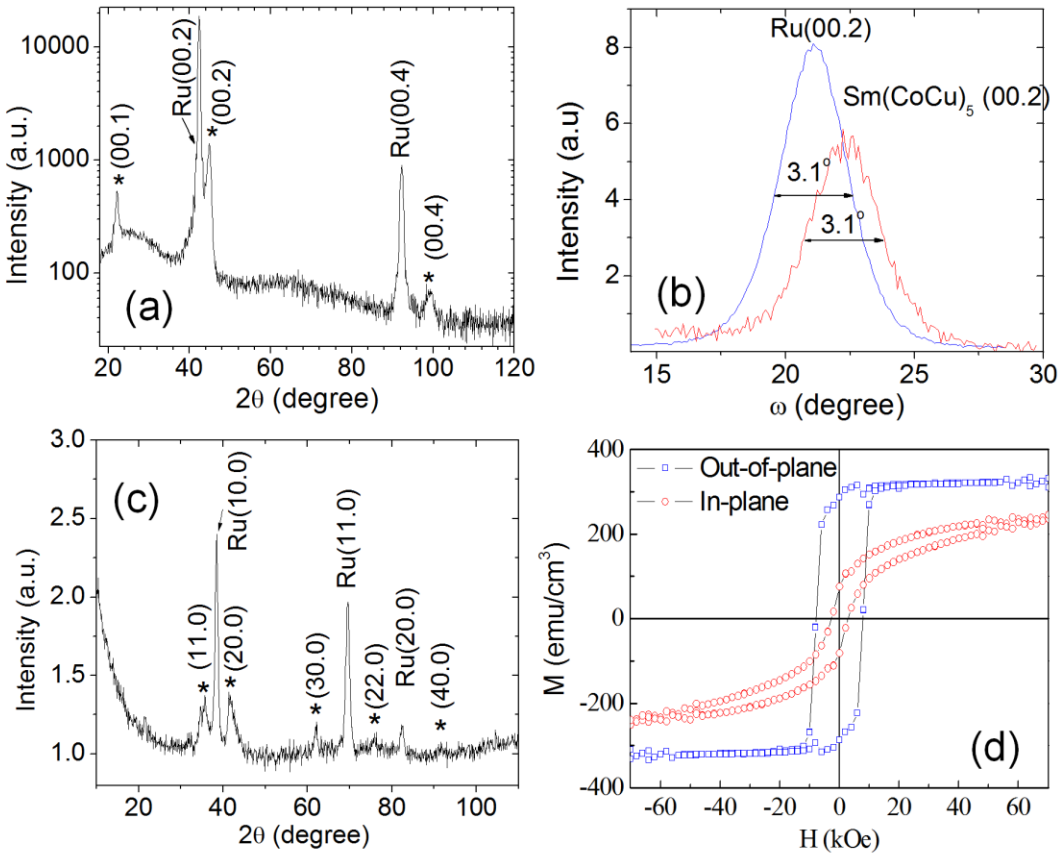

Figure 3.2 The XRD spectra and hysteresis loops of $Sm(Co, Cu)_5$ thin film (20 nm): (a) Normal θ-2θ scan, (b) $\Delta\theta_{50}$ of rocking curves of (00.2) peaks, (c) In-plane scan, (d) Hysteresis loops measured by SQUID at high field and room temperature. Note: " * " stands for $Sm(Co, Cu)_5$ phase in the XRD spectra.

Estimation of H_K and K_u

H_K of 200 ~ 350 kOe can be estimated from the interception point between the in-plane and the out-of-plane loops, as shown in Fig. 3.3. Given the average saturation

magnetization of ~ 330 emu/cm^3, the maximum magnetocrystalline anisotropy constant (K_u) in these $Sm(Co, Cu)_5$ thin film can be estimated to be around 3.3 ~ 5.8 × 10^7 erg/cm^3.

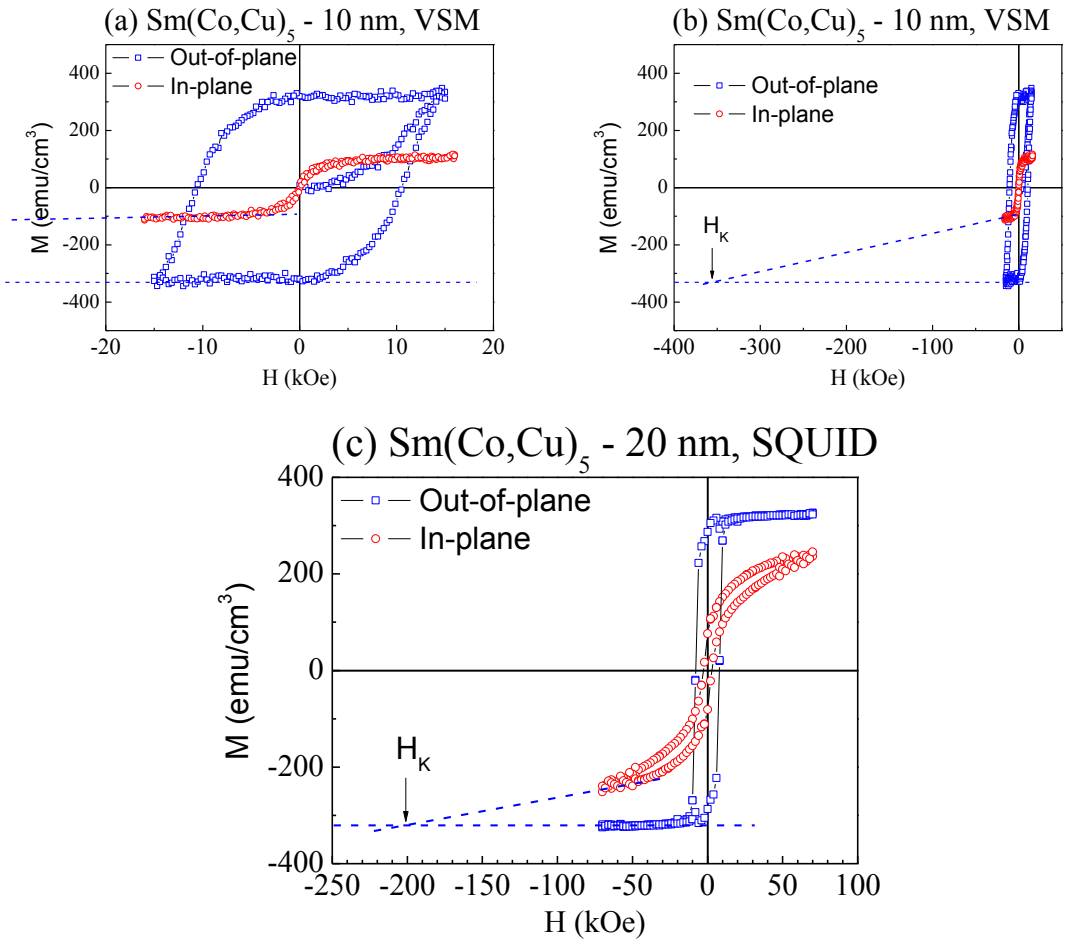

Figure 3.3 H_K estimation from the interception point between the in-plane and the out-of-plane loops: (a) $Sm(Co, Cu)_5$ thin film of 10 nm measured by VSM; (b) same set of data as (a), but the left scale is zoomed out to show the interception point (H_K); (c) $Sm(Co, Cu)_5$ thin film of 20 nm measured by SQUID.

Magnetization reversal mechanism: domain-wall pinning

Magnetization reversal is dominated by domain wall pinning mechanism as revealed by the angular dependence of coercivity and remanence coercivity and other supporting evidences including initial magnetization curves, minor hysteresis loops, and the relationship between IRM remanence and DCD remanence.

A. Angular dependence of coercivity and remanence coercivity

Fig. 3.4 showed the angular dependence of normalized coercivity (H_c) and remanence coercivity (H_{cr}) of $Sm(Co, Cu)_5$ thin film (10 nm). Both H_c and H_{cr} increase with the angle between the applied field and easy axis (or field angle), which is the characteristic of a domain-wall movement assisted magnetization reversal. Note that the H_{cr} is missing for the field angle above 60°, which is because the magnetic moment is too small to measure reliably. Even the H_{cr} values at 60° might have significant measurement error as it deviates largely from the experimental fitting curve. It is interesting to see that the fitting curve does not follow the simple Kondorsky switching field distribution function (i.e. $H_{cr}(\vartheta) \sim 1/\cos(\vartheta)$). This result will be discussed in Chapter 4.

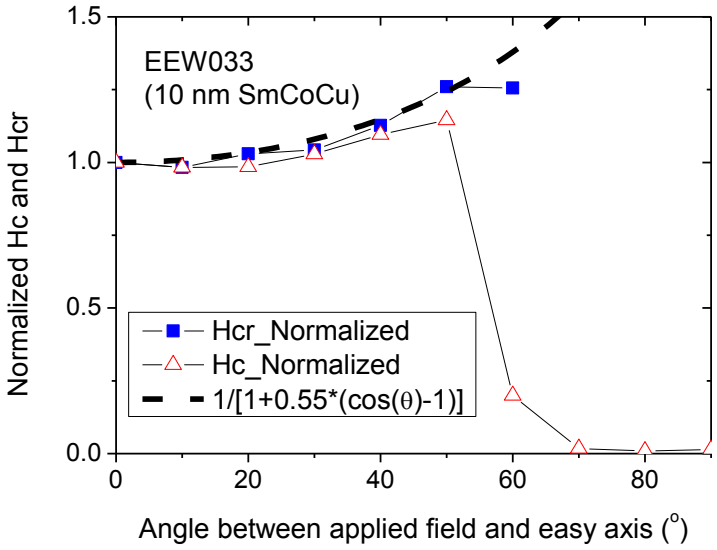

Figure 3.4 Angular dependence of normalized coercivity and remanence coercivity of $Sm(Co, Cu)_5$ thin film (10 nm).

It is well known that domain-wall movement assisted magnetization reversal mechanism including two types: domain-wall pinning and domain-wall nucleation. The angular dependence behaviour of H_c and H_{cr} cannot tell which type is the dominant one in our $Sm(Co, Cu)_5$ thin films.

B. Out-of-plane and in-plane hysteresis loops with initial magnetization curve

The typical shape of initial magnetization curve, as shown in Fig. 3.3 (a), excludes the nucleation-type domain wall switching as the magnetization reversal mechanism in these thin films. Therefore, domain-wall pinning should be the dominant switching mechanism in $Sm(Co, Cu)_5$ thin films. The initial magnetization curve can be interpreted as the following. The magnetic moment and remanence increase slowly at the beginning of magnetization under low applied field, since domain walls are pinned. However, once the applied field is strong enough to move domain walls across pinning sites, the magnetic moment and remanence will increase sharply.

C. Minor hysteresis loops

Fig. 3.5 showed the minor hysteresis loops and coercivities of $Sm(Co, Cu)_5$ thin film (10 nm) under varying external applied field. The coercivity increases little with the external field before 9 kOe but rapidly after that, indicating that the magnetization process should be classified as a pinning–type, not a nucleation-type, domain wall switching. This evidence is similar to the initial magnetization curves.

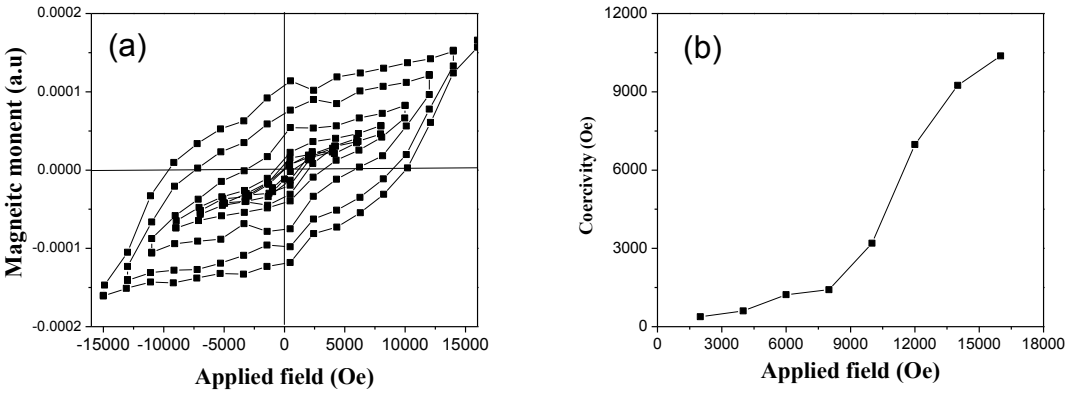

Figure 3.5 The minor hysteresis loops and coercivities of $Sm(Co, Cu)_5$ thin film (10 nm) measured by VSM.

D. Relationship between IRM remanence and DCD remanence

Remanence curves of Isothermal remanent magnetization (IRM) and DC demagnetization (DCD) of the sample $Sm(Co, Cu)_5$ thin film (10 nm) were measured. The following relationship between $M_D(H)$ and $M_R(H)$ is expected for a pinning type domain wall switching mechanism

$$\frac{M_D(H)}{M_R(\infty)} = 1 - 2\frac{M_R(H)}{M_R(\infty)} . \qquad (3.1)$$

Here $M_D(H)$ is the DCD remanence, $M_R(H)$ is the IRM remanence, and $M_R(\infty)$ is the saturation remanence.

Fig. 3.6 showed the measurement results from the sample $Sm(Co, Cu)_5$ thin film (10 nm). The dashed straight line is from the Eq. (3.1). It is clear that the measured results match the Eq. (3.1) very well, proving that the pinning type domain wall switching is indeed dominant (note that the rotational switching mechanism has a similar relationship, but it can be excluded from angular dependent coercivity and remanence coercivity behavior).

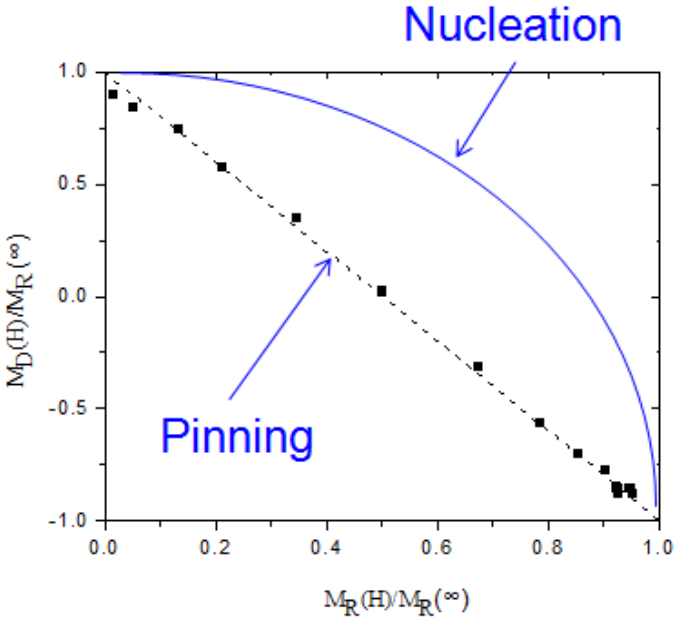

Figure 3.6 The relationship of normalized remanences between IRM and DCD of $Sm(Co, Cu)_5$ thin film (10 nm) measured by VSM.

Microstructure study under SEM, AFM, plane-view and cross-section-view TEM

Various types of pinning sites were identified, such as voids, grain/matrix boundaries (or crystalline/amorphous boundaries), grain boundaries between crystalline grains, and composition inhomogeneity in grains. Detailed results and discussion on microstructure of pinning sites in $Sm(Co, Cu)_5$ thin films will be presented in Chapter 4.

3.3.2 **Effects of the substrate temperature**

Fig. 3.7 shows the out-of-plane magnetic hysteresis loops and XRD spectra of samples prepared at various substrate temperatures. The film structure is kept the same among them (glass\Ta(4.2 nm)\Ru(20 nm)\Sm-Co-Cu(10 nm)\Ta(3 nm)). The nominal composition of Sm-Co-Cu layer is $Sm_{15}Co_{52}Cu_{33}$. While the out-of-plane hysteresis loop of the sample prepared at substrate temperature 350 °C shows a perpendicular anisotropy with the squareness ratio of 0.7, the out-of-plane hysteresis loops of samples prepared at substrate temperature 150 °C and 250 °C show no such anisotropy, as their squareness ratios are 0.33 and near zero, respectively. In the XRD spectra, $Sm(Co, Cu)_5$ (0001) and (0002) peaks are present only for the sample prepared at 350 °C substrate temperature. Both the magnetic measurements and the XRD results clearly show that a relatively high deposition temperature is required to form $Sm(Co, Cu)_5$ (0001) texture.

Higher substrate temperature is desirable to achieve better crystallization of the Sm-Co-Cu thin films. However, the glass substrates used in this study are thin sheets of cover-glass made from Corning 0211 glass. This type of glass has a relatively low strain point (508 °C, Corning 2006). The glass substrate deformation at the clamping sites becomes apparent even at a substrate temperature of around 400 °C in our system. On the other hand, as described in Chapter 1, the maximum temperature of safe operation (for several hours continuously) in our 8-target sputtering system is around 450 ^{o}C, not much higher than the highest temperature (350 °C) used in this study. Therefore, we did not study the effect of substrate temperature higher than 350 °C, because of these limitations.

Further study on this effect requires both upgrading or modifying the heating stage of the current system to provide higher operating temperature and using glass substrates with a higher strain point (e.g. Corning 1737 with a strain point of 666 °C).

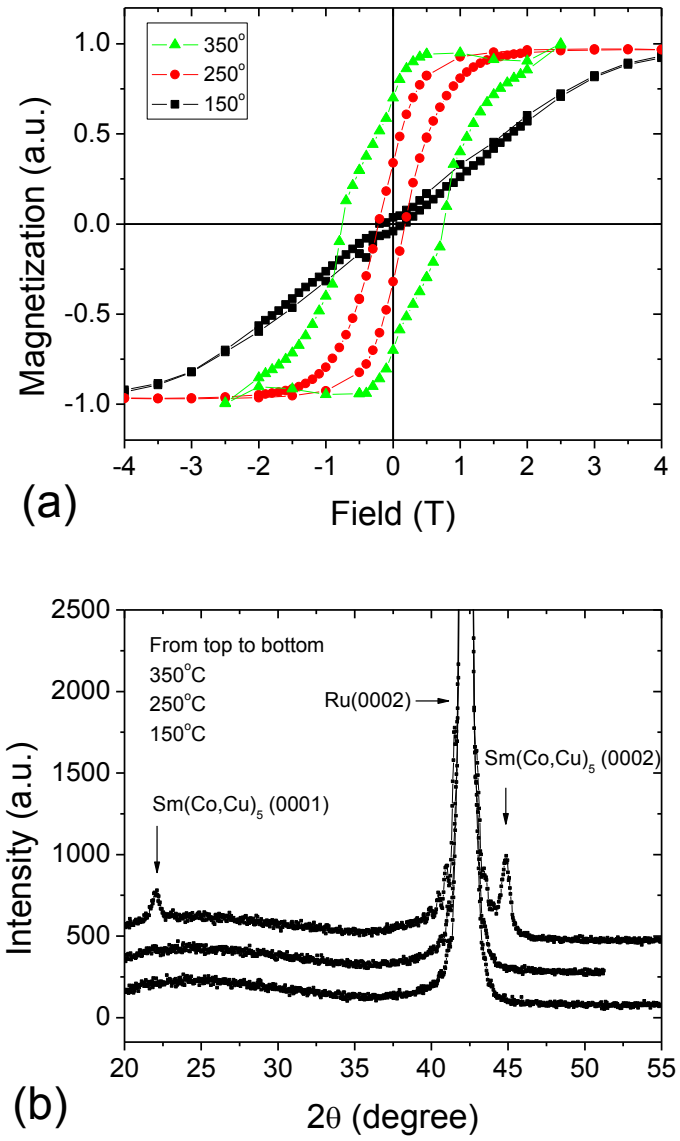

Figure 3.7 (a) Magnetic hysteresis loops along the out-of-plane direction and (b) XRD spectra of samples glass\Ta(4.2 nm)\Ru(20 nm)\Sm-Co-Cu(10 nm)\Ta(3 nm) deposited at different substrate temperature. (XRD results from top to bottom represent sample with deposition temperature: 350 °C, 250 °C, and 150 °C).

Another interesting observation of the effect of substrate temperature is the fringes of Ru (0002) diffraction peak, especially for samples deposited at higher temperature. Fig. 3.8 shows the enlarged XRD spectra around Ru (0002) of Fig. 3.4. It is apparent that higher annealing temperature led to stronger and more fringes of Ru (0002), which indicates lower surface roughness on short lateral length scales. The thickness of Ru underlayer calculated from the fringes at 350 °C is ~18 nm, which is in agreement with the nominal (designed) Ru underlayer thickness of 20 nm.

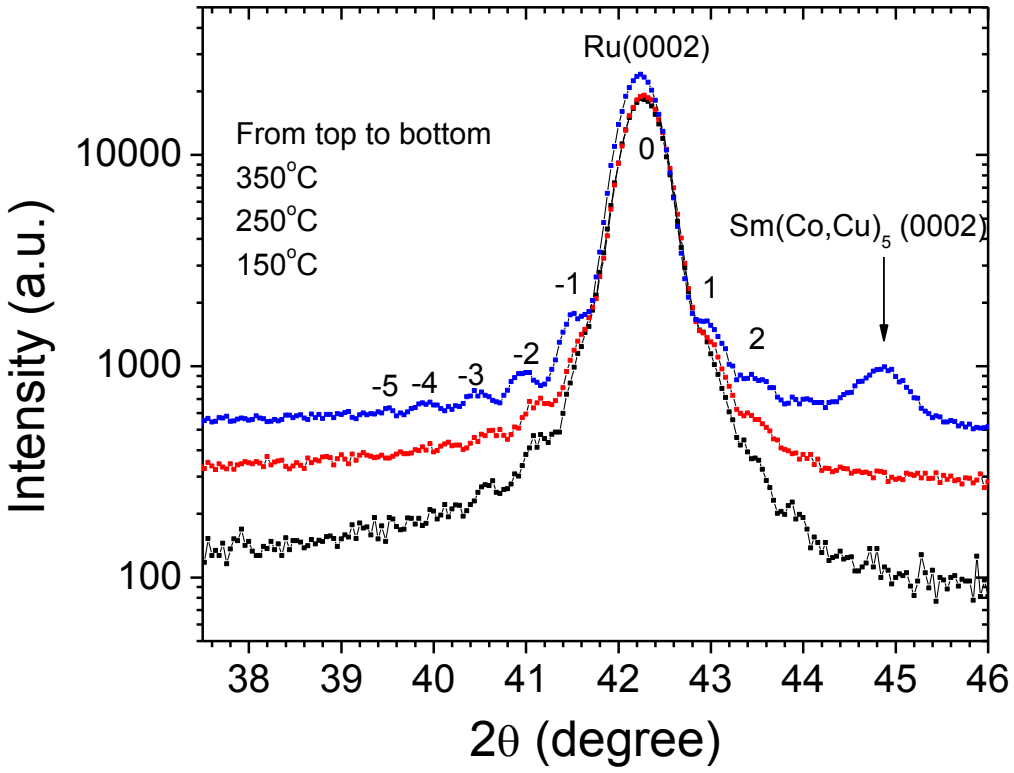

Figure 3.8 The dependence of Ru (0002) fringes on the annealing temperature. Fine fringes of the Ru (0002) peaks are labeled with the order of diffraction.

3.3.3 **Effects of the Sm-Co-Cu layer thickness**

Fig. 3.9 shows the out-of-plane and in-plane magnetic hysteresis loops of Sm-Co-Cu films on Ru(0002) underlayer with different film thicknesses. The deposition substrate

temperatures for the Sm-Co-Cu layers in the samples are 350 °C. The remanence squareness ratios of four loops are close to 1, which suggest that all Sm–Co–Cu films have strong perpendicular magnetic anisotropy, consistent with good $Sm(Co, Cu)_5$ (0001) texture, even when the film thickness is as thin as 5 nm (note: the increase of M below 5 kOe should be due to measurement errors in background removal).

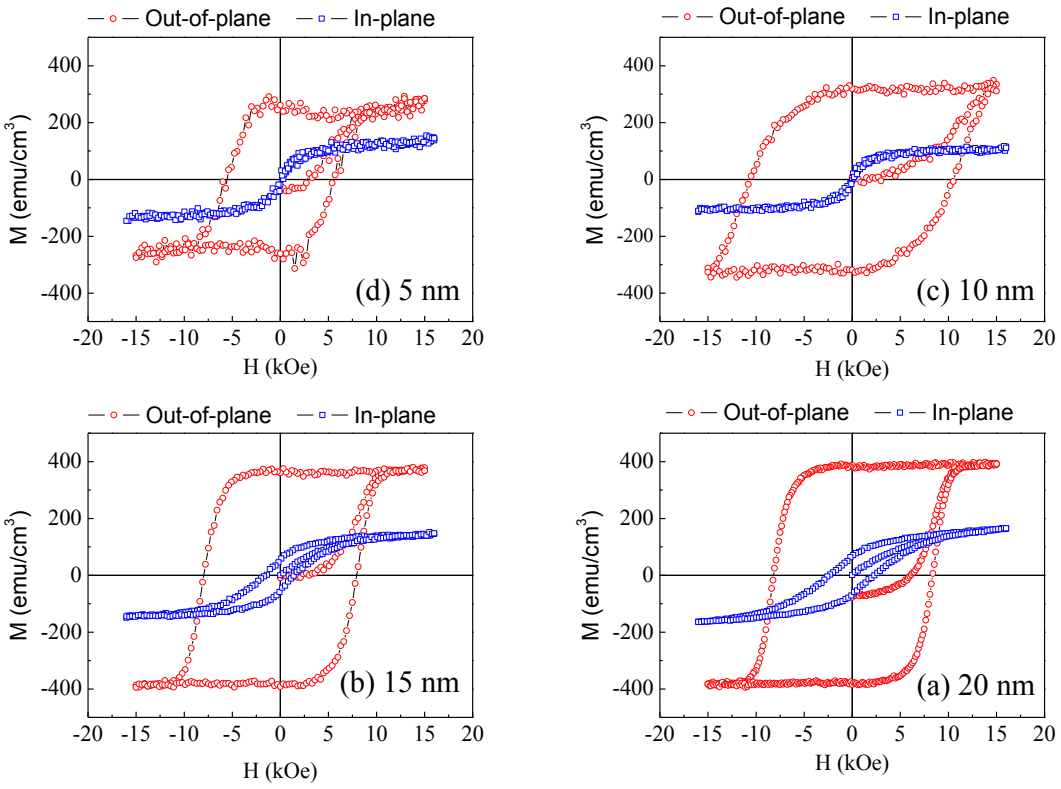

Figure 3.9 The out-of-plane and in-plane hysteresis loops with initial magnetization curves of $Sm(Co, Cu)_5$ thin films measured by VSM.

Squareness of in-plane hysteresis loops is near zero (0) when the thickness of $Sm(Co, Cu)_5$ films is 10 nm or thinner, but it increases with the thickness when that is thicker than 15 nm. These results showed that thinner $Sm(Co, Cu)_5$ films ($\leq$ 10 nm) in our study have better out-of-plane orientation ratio or less misoriented grains whose easy axis is not normal to the film surface. This result is consistent with the finding in previous XRD and

TEM results that the $Sm(Co, Cu)_5$ films were grown epitaxially on the Ru (00.2) underlayer.

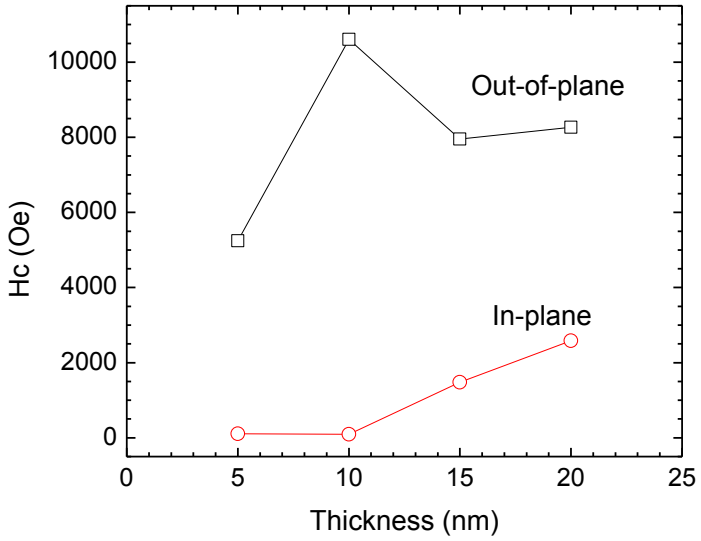

Figure 3.10 Thickness effect on the out-of-plane and in-plane coercivities of $Sm(Co, Cu)_5$ thin films.

The coercivity of $Sm(Co, Cu)_5$ films showed clear thickness dependence, as shown in Fig. 3.10. The out-of-plane coercivity has a maximum of ~ 11 kOe at 10 nm. All films, thin or thick, showed small out-of-plane coercivity. The in-plane coercivity stays close to 0 for the film thickness smaller than 10 nm but will increase with the film thickness above 10 nm.

The thickness dependence of the coercivity of $Sm(Co, Cu)_5$ film could be explained by combining the effects of the formation of misoriented grains in thicker films and more defects in thinner films, such as magnetic dead layer at the interface between the Sm–Co–Cu layer and Ru underlayer. The existence of magnetic dead layer could be caused by interfacial strain (Hayashi et al. 2004) or ion etching during film deposition (Si et al. 2005). The strain is induced by the lattice misfit between $Sm(Co, Cu)_5$ layer and Ru underlayer. The ion etching comes from Ar^+ ion in the plasma. In this case, the strain could be the main reason for the dead layer because of the 8% lattice misfit between

$Sm(Co, Cu)_5$ (0001) plane and Ru (0002) plane. The dead layer thickness, estimated by fitting (Moment / Area) versus Thickness curve, is about 1.7 nm, as shown in Fig. 3.13. When the film thickness is 5 nm, the coercivity of the entire film is lowered down by the magnetic dead layer which could have a lower coercivity as well as the defects in the layer above the dead layer which means a smaller K_u. If the Sm–Co–Cu layer is thicker (up to 10 nm), the influences of the dead layer and defects are reduced. Therefore, there is an increase of the coercivity for 10-nm Sm-Co-Cu film. When the film thickness increased to 15 or 20 nm, the column growth of films may be weakened. Many misoriented grains begin to show up as seen in the non-zero remanence in the in-plane loops. These misoriented grains could cause the decrease of the coercivity of the entire film. Additional discussion on the coercivity will be presented in Chapter 4.

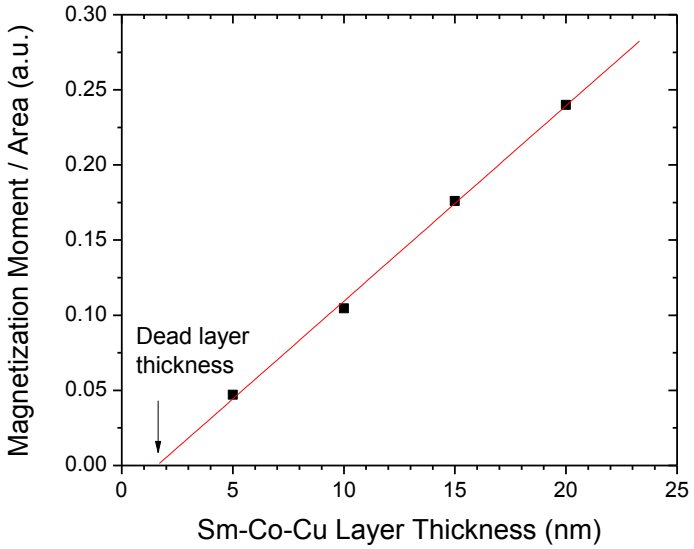

Figure 3.11 Estimation of the magnetic dead layer thickness in Sm-Co-Cu thin films grown on Ru underlayer.

3.3.4 **Effects of the Sm-Co-Cu film composition**

Composition effect on the crystallization, structure, and magnetic properties of Sm-Co-Cu thin films was studied in a series of samples as shown in Table 3.1. Here, the Sm–

Co–Cu layer was mainly designed to keep the Sm/(CoCu) ratio (y) close to 5 and vary the Co/Cu ratio (x) from 0 to ~ 0.4, where the magnetic anisotropy of $Sm(Co_{1-x}Cu_x)_y$ is expected to be larger than 5×10^7 erg/cm^3 (Lectard et al. 1994). An exception is the sample #4, which is off the stoichiometry of $Sm(Co, Cu)_5$ (slightly Sm-deficient) and Cu-rich. The nominal compositions are calculated from calibrated deposition rate (nm/s) and molar volume of each element.

Table 3.1 Nominal compositions of the Sm-Co-Cu layer in the study of the composition effect on the crystallization, structure, and magnetic properties of Sm-Co-Cu thin films.

Sample #	Nominal composition			Nominal $Sm(Co_{1-x}Cu_x)_y$	
	Sm	Co	Cu	y	x
1	17	83	0	4.9	0.00
2	16	69	15	5.3	0.18
3	16	53	31	5.3	0.37
4	14	46	40	6.1	0.47

Fig. 3.12 shows the out-of-plane magnetic hysteresis loops and XRD spectra of samples with the same thickness (10 nm) of the Sm–Co–Cu layer but different nominal compositions. The deposition substrate temperature for the Sm-Co-Cu layer was 350 °C. Magnetic properties show that the Sm–Co–Cu samples with proper Cu concentration (#3 and #4) have perpendicular anisotropy. "Kinks" are observed around the remanence points in the hysteresis loops, which suggests soft magnetic phase(s) existing in the Sm–Co–Cu layer. XRD results indicate that sample #3 $Sm(Co_{0.63}Cu_{0.37})_{5.3}$ and #4 $Sm(Co_{0.53}Cu_{0.47})_{6.1}$ have $Sm(Co, Cu)_5$ (0001) texture, but the off-stoichiometric sample (#4) shows much weaker $Sm(Co, Cu)_5$ (0001) and (0002) peaks. Attempts to fabricate Sm–Co films with perpendicular anisotropy with less Cu content (x = 0, 0.18) failed.

As revealed in Figs. 3.7 and 3.12, Cu's addition shows a similar effect as increasing the deposition temperature, which helps the Sm-Co-Cu layer to form $SmCo_5$-type phases. This result confirms that Cu's addition in the Sm–Co–Cu layer lowers the crystallization temperature $Sm(Co, Cu)_5$ thin films, which is consistent with the lower melting point of

$Sm(Co, Cu)_5$ phase with increasing Cu content as shown in the $SmCo_5$-$SmCu_5$ pseudobinary phase diagram (Fig. 2.15).

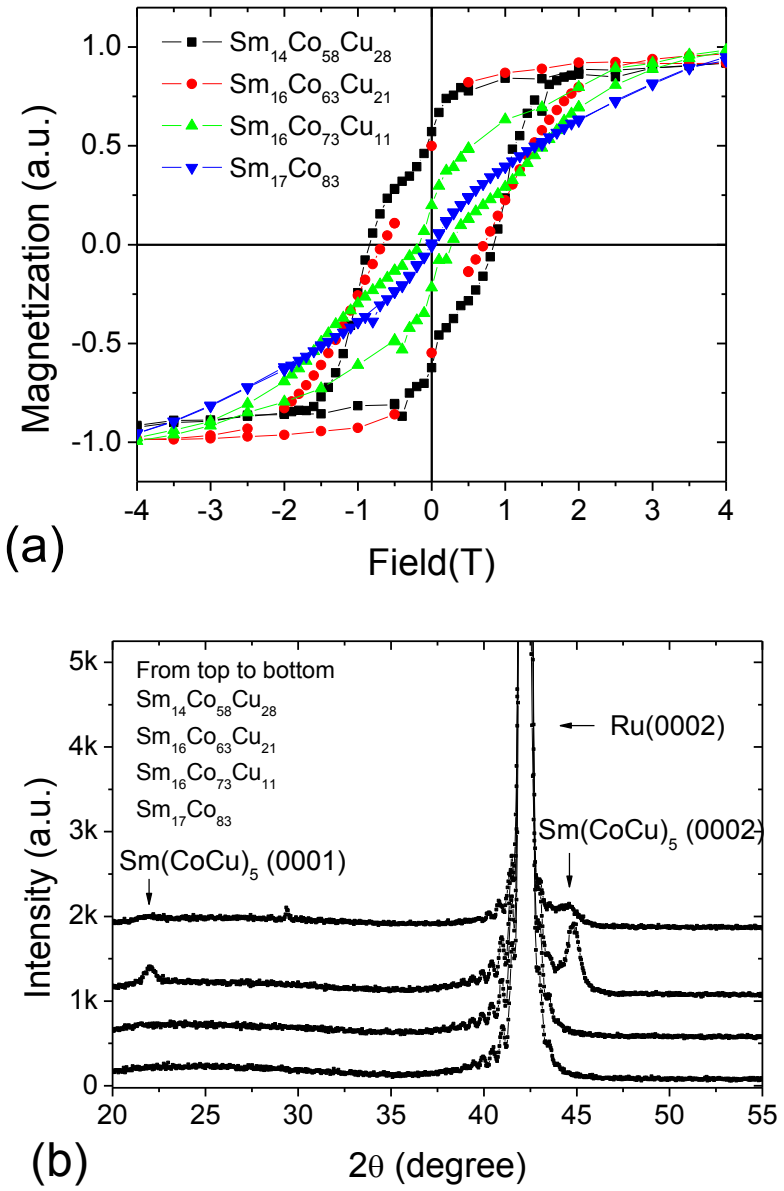

Figure 3.12 (a) Magnetic hysteresis loops in the perpendicular direction and (b) XRD spectra of samples with different Sm–Co–Cu compositions. (XRD results from top to bottom represent sample with composition: $Sm_{14}Co_{58}Cu_{28}$, $Sm_{16}Co_{63}Cu_{21}$, $Sm_{16}Co_{73}Cu_{11}$, and $Sm_{17}Co_{83}$).

3.4 Composition of $Sm(Co, Cu)_5$ Grains

Average composition of Sm-Co-Cu thin films in this study can be obtained directly by Rutherford backscattering spectroscopy (RBS). However, compositions of Sm-Co-Cu thin films are not uniform across the film plane, as discussed later in Chapter 4. XRD data have shown that the only crystalline phase in the Sm-Co-Cu layer is $Sm(Co, Cu)_5$. Microstructure study in Chapter 4 reveals that Sm-Co-Cu thin films consist mainly of nanocrystalline grains although a small fraction of amorphous regions is also seen. The median composition of nanocrystalline $Sm(Co, Cu)_5$ grains can be estimated from the structural parameters (e.g. unit volume, lattice constants *a* and *c*) or Curie temperature of the film, by comparing to the data of bulk $Sm(Co, Cu)_5$ alloys reported in the literature. The film compositions from these methods are discussed below.

3.4.1 Composition estimation by Curie temperature

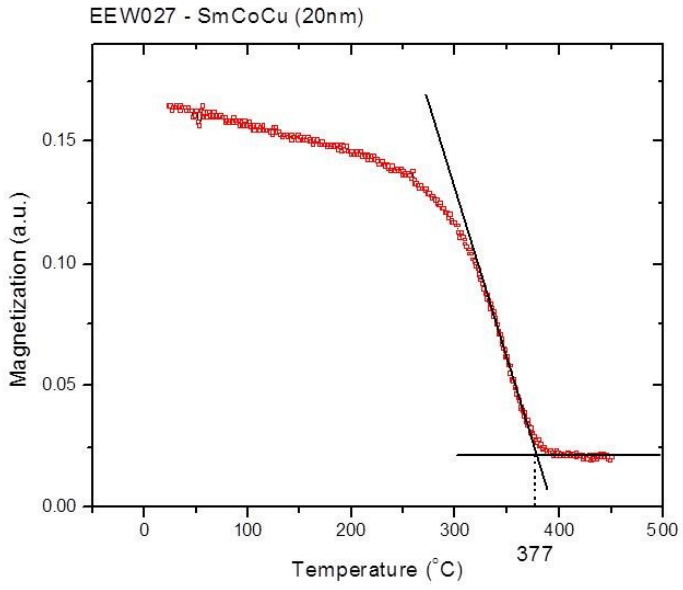

Figure 3.13 Curie temperature determination of the sample glass\Ta(4.2 nm)\Ru(20 nm)\Sm-Co-Cu(20 nm)\Ta(3 nm) deposited at the substrate temperature of 350 °C. It is the same sample in Fig. 3.1.

Fig. 3.13 shows the M - T curve of one sample (EEW027) with the thickest (20 nm) $Sm(Co, Cu)_5$ film. The Curie temperature determined from the M - T curve is 377 °C. The Curie temperature of bulk $Sm(Co, Cu)_5$ phases have been reported in the literature. Therefore, by comparing to the data reported by Téllez-Blanco et al. (1998), the composition (x) of $Sm(Co_{1-x}Cu_x)_5$ in the sample EEW027 can be estimated to be about 2.0, as shown in Fig. 3.14. Note that we choose the Tc curve of annealed bulk $Sm(Co_{1-x}Cu_x)_5$ materials for the composition estimation, because the as-casted materials are suspected to have excess of Cu not entering the $Sm(Co, Cu)_5$ phase as reported by the authors.

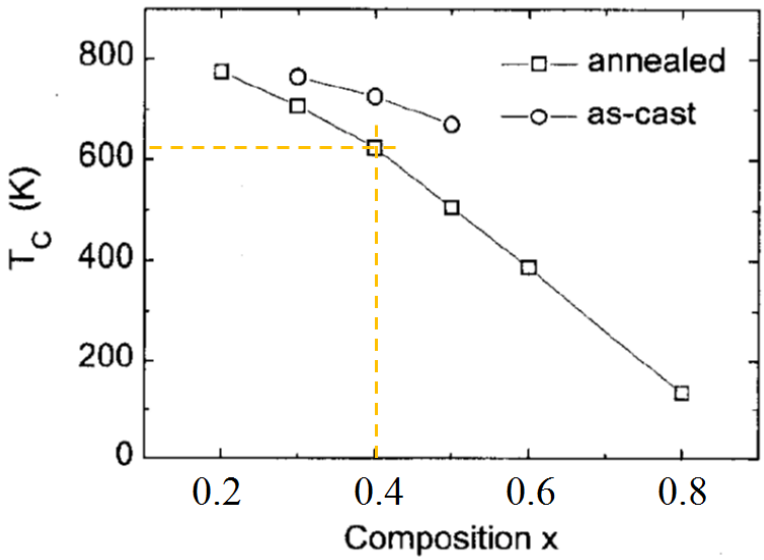

Figure 3.14 Estimation of the composition of $Sm(Co_{1-x}Cu_x)_5$ crystalline phase in the $Sm(Co, Cu)_5$ thin film (20 nm) based on Curie temperature. [Adapted from Téllez-Blanco et al. 1998]

3.4.2 **Composition estimation by lattice constants and unit volume**

The lattice constants (a and c) and unit volume of the sample EEW027 can be calculated from the XRD data (as shown in Fig. 3.1). Comparing to the data of bulk

$Sm(Co_{1-x}Cu_x)_5$ materials, the composition x can be estimated accordingly as shown in Fig. 3.15.

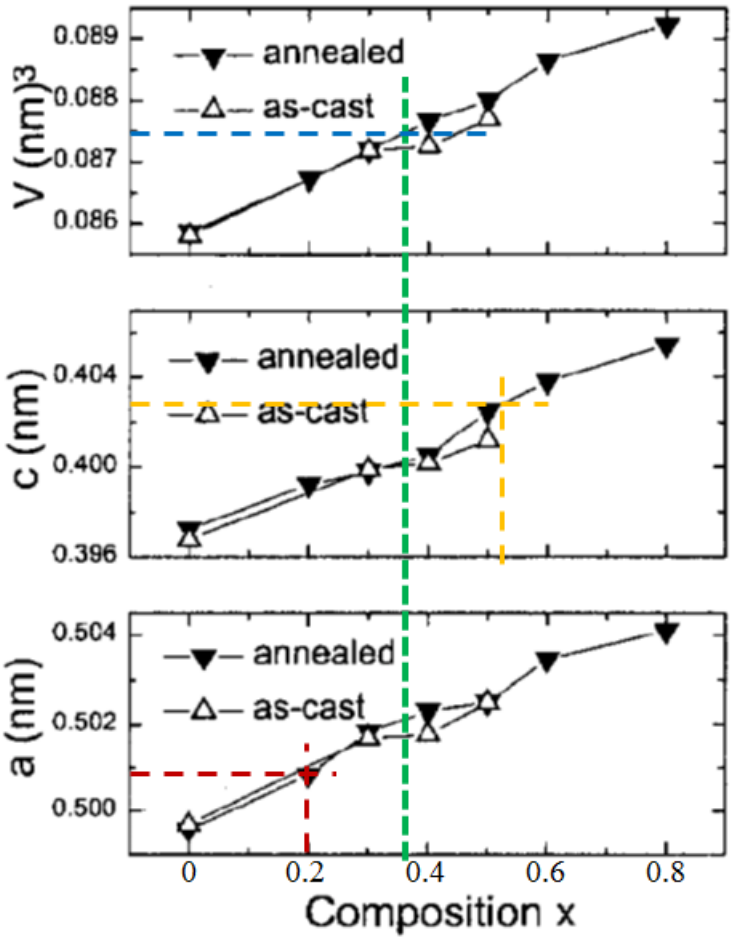

Figure 3.15 Estimation of the composition of $Sm(Co_{1-x}Cu_x)_5$ crystalline phase in the $Sm(Co, Cu)_5$ thin film (20 nm) based on unit volume and lattice constants (a and c). [Adapted from Téllez-Blanco et al. 1998]

3.4.3 **Discussion on composition estimation and strain in $Sm(Co, Cu)_5$ films**

The compositions x of the crystalline $Sm(Co_{1-x}Cu_x)_5$ phase estimated from lattice constants, unit volume, and Curie temperature are summarized in Table 3.2. The estimated compositions from unit volume and Curie temperature matched reasonably

well with each other. The average of these two values (x = 0.38) should be reliably close to the true composition of the $Sm(Co, Cu)_5$ grains in the film. Distinctly different x values are seen in the estimations from lattice constants. It can be explained if there exists in-plane compressive strain in $Sm(Co, Cu)_5$ grains due to epitaxial growth on Ru (0002) underlayer, which could lead to a reduced in-plane lattice constant a and expanded out-of-plane lattice constant c respectively. Similar but larger lattice distortions are also seen in $SmCo_5$ (0001) films grown on Ru buffered single crystal α-Al_2O_3 (0001) substrate (Seifert et al. 2009).

Table 3.2 Summary of estimated compositions of the crystalline $Sm(Co_{1-x}Cu_x)_5$ phase in the sample EEW027 (20 nm) from lattice constants, unit volume, and Curie temperature.

Parameters for composition estimation	***a* (nm)**	***c* (nm)**	***V* (nm^3)**	**Tc (°C)**
	0.5008	0.4027	0.0875	377
Estimated *x* in $Sm(Co_{1-x}Cu_x)_5$	0.20	0.52	0.36	0.40

Table 3.3 Strain estimations in $Sm(Co_{0.62}Cu_{0.38})_5$ film on Ru underlayer and the $SmCo_5$ film on Ru buffered single crystal α-Al_2O_3 (0001) substrate.

Phase	**$Sm(Co_{0.62}Cu_{0.38})_5$**		**$SmCo_5$**	
Lattice const.	***a* (nm)**	***c* (nm)**	***a* (nm)**	***c* (nm)**
Thin film[(a)]	0.5008	0.4027	0.4945	0.4021
Bulk alloy[(b)]	0.5022	0.4004	0.4996	0.3973
Strain	-0.28%	0.58%	-1.01%	1.22%

Source: (a) data of $Sm(Co_{0.62}Cu_{0.38})_5$ thin film are from this study, and data of $SmCo_5$ thin film are from Seifert et al. (2009); (b) data from Téllez-Blanco et al. (1998).

Table 3.3 shows the strain estimations in the $Sm(Co_{0.62}Cu_{0.38})_5$ film (sample EEW027) and the $SmCo_5$ film on Ru buffered single crystal α-Al_2O_3 (0001) substrate (Seifert et al. 2009). Even though $Sm(Co_{0.62}Cu_{0.38})_5$ film has larger lattice constants than the $SmCo_5$ film, it has relatively smaller strains in both *a* and *c* axes when grown on Ru underlayer. This could be due to the difference in microstructure of Ru underlayer. The Ru underlayer on a glass substrate with a Ta seed layer is polycrystalline, while the Ru buffer layer on single crystal α-Al_2O_3 (0001) substrate is single crystalline. Single crystalline Ru underlayer should be able to exert much larger interface stress on the epitaxial film grown on it. Thus, it is reasonable to see larger strain in the $SmCo_5$ film grown on the Ru buffer layer which is grown on a single crystal α-Al_2O_3 (0001) substrate.

In Section 2.8.1, we have discussed two types (Type A and B) of epitaxial orientation relationship between $SmCo_5$ (0001) crystal and Ru underlayer when grown on single crystal α-Al_2O_3 (0001) substrate. The misfits of Type A and B of $SmCo_5$ (0001) on the Ru (0001) layer are -7.7% and 6.6%, respectively. Because only Type B would cause compressive strain in the $SmCo_5$ grains, we can conclude that Type B epitaxial growth is dominant in the growth of the $Sm(Co_{0.62}Cu_{0.38})_5$ (0001) film on Ta\Ru (0002) underlayer. This conclusion has significant implication on the design/optimization of the lattice misfit between the underlayer and the $Sm(Co, Cu)_5$ layer to achieve better crystallization, *c*-axis texture, and perpendicular anisotropy. Because now decreasing the lattice constant of Ru underlayer by doping smaller Cr atoms will lead to larger misfit between the $Sm(Co, Cu)_5$ films and the Ru(Cr) underlayer, instead of smaller misfit as original planned.

3.5 $Sm(Co, Cu)_5$ (0001) Thin Films on Ru(Cr) Underlayer

In our original design, Cr doped Ru underlayer is expected to have smaller lattice constants, and consequently smaller lattice misfit between the underlayer and the $Sm(Co, Cu)_5$ layers grown on it, if the epitaxial growth relationship follows Type A route. According to the Cr-Ru binary phase diagram, as shown in Fig. 3.16, $Ru_{1-x}Cr_x$ will maintain hcp structure for $x \leq \sim 0.5$ at the temperature of 1073 K (Predel and Madelung).

Excess amount of Cr doping ($x > \sim 0.5$) will lead to the segregation of a phase of σ, Cr_3Ru, or bcc structured (Cr).

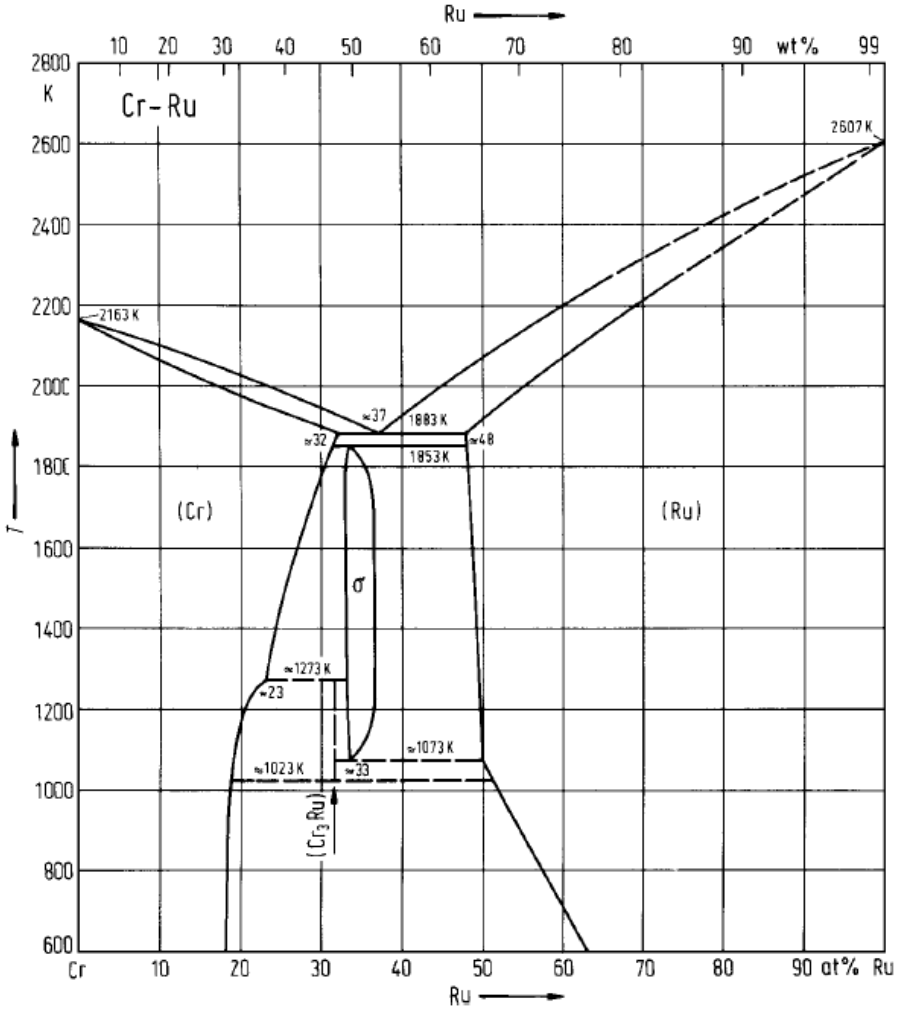

Figure 3.16 Cr-Ru binary phase diagram. [Predel and Madelung]

In our experiment, we studied the Cr doping range ($x = 0 \sim 0.62$), which is slightly beyond the single hcp (Ru) phase boundary. We expect the excess Cr will segregate from hcp Ru phase and diffuse into grain boundaries to induce smaller Ru grains. The Cr compositions are nominal values calculated from the sputtering deposition rates and molar volumes of Ru and Cr. Samples with the layer structure of glass\Ta(4.2 nm)\Ru(10

nm)\$Ru_{1-x}Cr_x$(10 nm)\Sm-Co-Cu(20 nm)\Ta(3 nm) were investigated. Deposition conditions are the same as samples with Ru underlayer only, except that the Ru(Cr) layer was deposited at same substrate temperature as the Sm-Co-Cu layer (350 °C). The composition of $Sm(Co, Cu)_5$ is the same as the sample EEW027 studied in previous sections, i.e. $Sm(Co_{0.62}Cu_{0.38})_5$.

3.5.1 Structural properties of $Sm(Co, Cu)_5$ (0001) thin films on Ru(Cr) underlayer

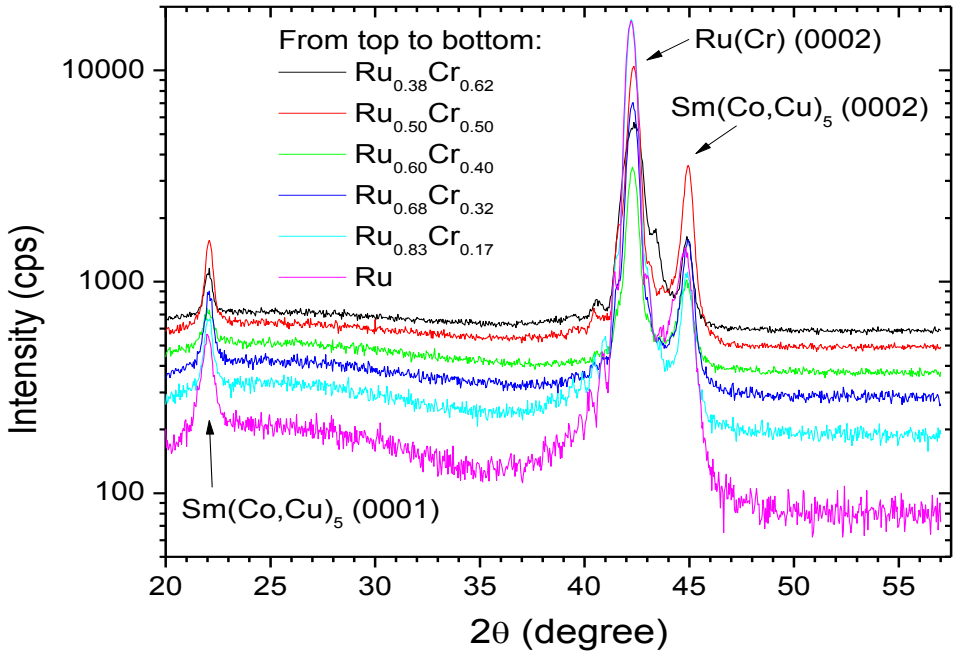

Figure 3.17 The XRD spectra by normal θ-2θ scan of $Sm(Co, Cu)_5$ thin films (20 nm) grown on $Ru_{1-x}Cr_x$ underlayers ($0 \le x \le 0.62$).

Fig. 3.17 shows the XRD spectra by normal θ-2θ scan of all Sm-Co-Cu samples grown on Ru(Cr) underlayers. Good $Sm(Co, Cu)_5$ (0001) texture is seen in all these samples. No diffraction peaks of phases other than Ru and $Sm(Co, Cu)_5$ were detected. This result is encouraging, because it confirmed that the lattice misfit between Ru underlayer and $Sm(Co, Cu)_5$ magnetic layer can be adjusted in a wide range without

causing any significant damage to the crystallization and texture of $Sm(Co, Cu)_5$ thin films.

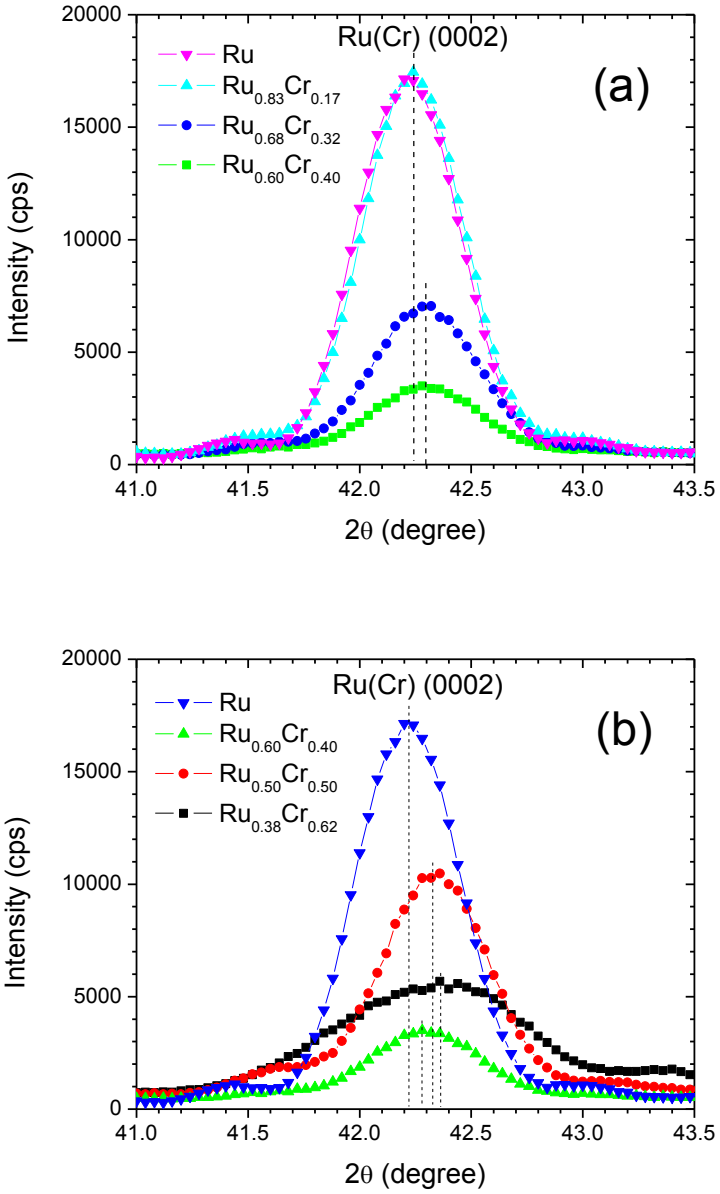

Figure 3.18 The XRD spectra showing the Cr composition x dependence of Ru(Cr) (0002) peak: (a) $0 \leq x \leq 0.40$; (b) $0.4 \leq x \leq 0.62$.

Fig. 3.18 (a) and (b) show the enlarged XRD spectra around Ru(Cr) (0002) peak for all samples. Note that the Ru(Cr) (0002) peak is a mixed signal including diffractions

from both the bottom Ru layer and the upper Ru(Cr) layer. It is clearly seen that the shift of Ru(Cr) (0002) peak towards high 2θ value as the Cr doping increase, which means smaller lattice constant *c*, just as expected, when $x \leq 0.40$, as seen in Fig. 3.18 (a). The peak intensity of Ru(Cr) (0002) did not change much for $x \leq 0.17$, but it decreases significantly beyond that, accompanying with a relatively larger change in 2θ value too. Because the 10 nm Ru(Cr) layer is grown on 10 nm Ru underlayer, it is possible that, with small amount Cr doping, the epitaxial growth of Ru(Cr) on Ru is maintained very well due to relatively small lattice misfit. But when the Cr doping is 0.32 and more, the lattice misfit might become so large that the epitaxial growth has been affected.

For $x > 0.4$, the Ru(Cr) (0002) peak continues moving to higher angles with larger *x*, as shown in Fig. 3.18 (b). The peak intensity first increase at $x = 0.5$, then decrease at $x = 0.62$. It is not clear why the trend in peak intensity reduction with increasing Cr is reversed since the $Ru_{0.5}Cr_{0.5}$ underlayer. The clearly widened Ru(Cr) (0002) peak with $x = 0.62$ may be related to Cr segregation due to the excess Cr doping, which made the Ru(Cr) alloy out of the single phase composition region given in the phase diagram.

Table 3.4 Lattice constants and nominal strain values of Ru(Cr) films grown on Ru underlayer.

Composition of Ru(Cr)		Lattice Const. of Ru(Cr)			Nominal Strain Values		
Ru	Cr	a^1 (nm)	c^1 (nm)	c^2 (nm)	$a^1 - a^1_0$	$c^1 - c^1_0$	$c^2 - c^2_0$
1.00	0.00	0.2706	0.4281	0.4281			
0.84	0.17	0.2680	0.4276	0.4279	-0.96%	-0.13%	-0.05%
0.68	0.32	0.2664	0.4265	0.4273	-1.55%	-0.37%	-0.18%
0.60	0.40	0.2660	0.4256	0.4273	-1.70%	-0.60%	-0.18%
0.50	0.50	-	-	0.4270	-	-	-0.25%
0.38	0.62	-	-	0.4267	-	-	-0.32%

Source: (1) Predel, B.: Cr-Ru (Chromium-Ruthenium). Madelung, O. (ed.). Springer Materials - The Landolt-Börnstein Database; (2) data calculated from Ru (0002) peak positions in this study.

Table 3.4 summarizes the lattice constants of Ru(Cr) alloys and thin films using the data in the literature and this study, and nominal strain values of Ru(Cr) films grown on

Ru underlayer. The lattice constant *c* values of Ru(Cr) films (c^2) are generally larger than that of the bulk phase (c^1). Besides the experimental errors in determining the nominal Ru(Cr) compositions, it must be noted that the lattice constant c^2 value is artificially larger than the true lattice constant value of a Ru(Cr) film, because of the mixed signals from both the bottom Ru layer and the Ru(Cr) layer itself.

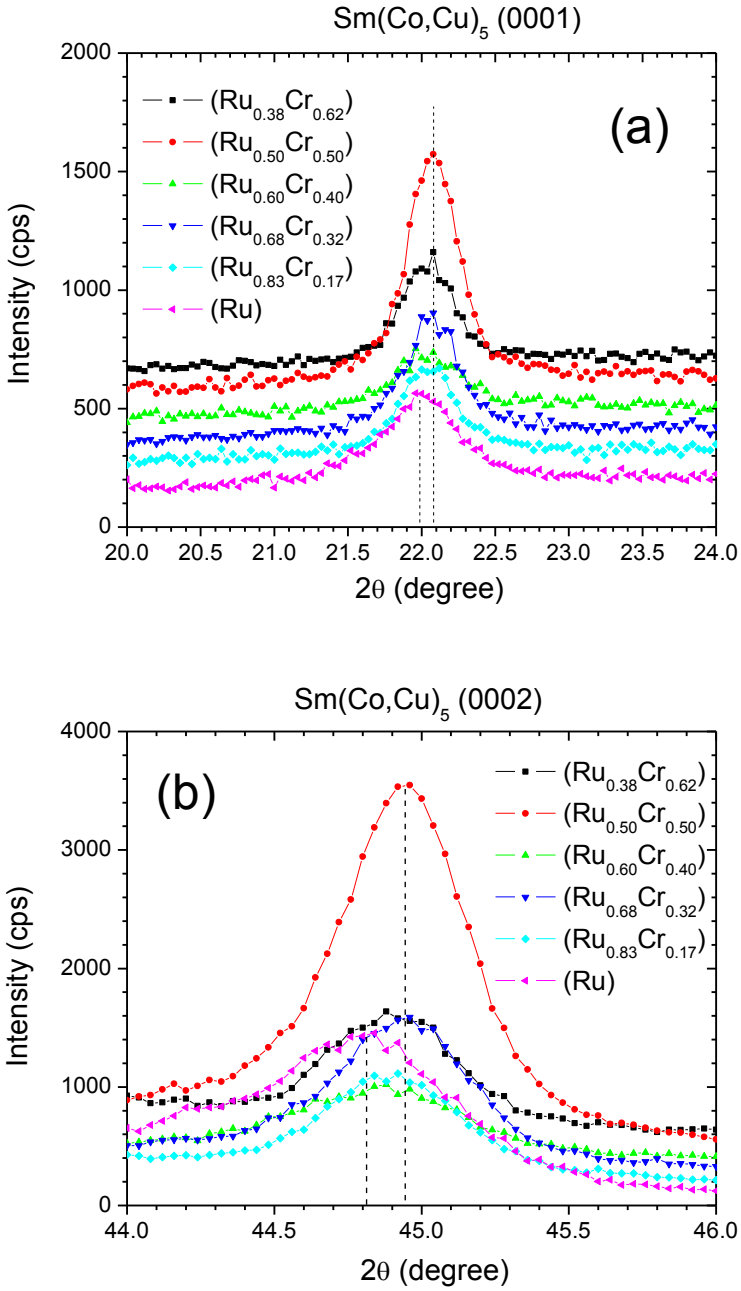

Figure 3.19 The XRD spectra showing the Cr composition x dependence ($0 \leq x \leq 0.62$) of $Sm(Co, Cu)_5$ peaks: (a) $Sm(Co, Cu)_5$ (0001) peak; (b) $Sm(Co, Cu)_5$ (0002) peak.

Fig. 3.19 (a) and (b) show the enlarged XRD spectra around $Sm(Co, Cu)_5$ (0001) and (0002) peaks for all samples. Unusually high intensities of these two peaks were observed in the sample of $x = 0.5$, consistent with the anomaly seen in the intensity of Ru (0002) peak. There seems to be a weak trend: the lattice constant c of $Sm(Co, Cu)_5$ (0001) grains decreases slightly with decreasing lattice constants of Ru(Cr) underlayer (due to increasing Cr doping). Small shifts (less than ~ 0.1°) might happen in both $Sm(Co, Cu)_5$ (0001) and (0002) peaks for Cr-doped Ru(Cr) underlayers. Considering the $Sm(Co, Cu)_5$ (0001) grains should have the same composition in these samples and thus same unit volume, this trend implies that the lattice constant a of $Sm(Co, Cu)_5$ (0001) grains increases with the decreasing lattice constant a of Ru(Cr) underlayer. This implication cannot be explained by the epitaxial growth of $Sm(Co, Cu)_5$ (0001) on Ru (0002) plane, with either compressive or tensile strains. In-plane XRD measurements of these samples are needed to investigate the lattice misfit at the interface.

3.5.2 **Magnetic properties of $Sm(Co, Cu)_5$ (0001) thin films on Ru(Cr) underlayer**

Fig. 3.20 shows the out-of-plane hysteresis loops of $Sm(Co, Cu)_5$ thin films (20 nm) grown on Ru(10 nm)\ Ru(Cr)(10 nm) underlayers with different $Ru_{1-x}Cr_x$ compositions. Perpendicular anisotropy with the squareness ratio larger than 0.8 is seen for all samples with the $x \leq 0.50$. The squareness ratio of the out-of-plane loop is reduced to ~ 0.55 for the high Cr-doping ($x = 0.62$), which is consistent with the poorer Ru(Cr) (0002) texture (low peak intensity and widened FWHM) as shown in Fig. 3.18 (b).

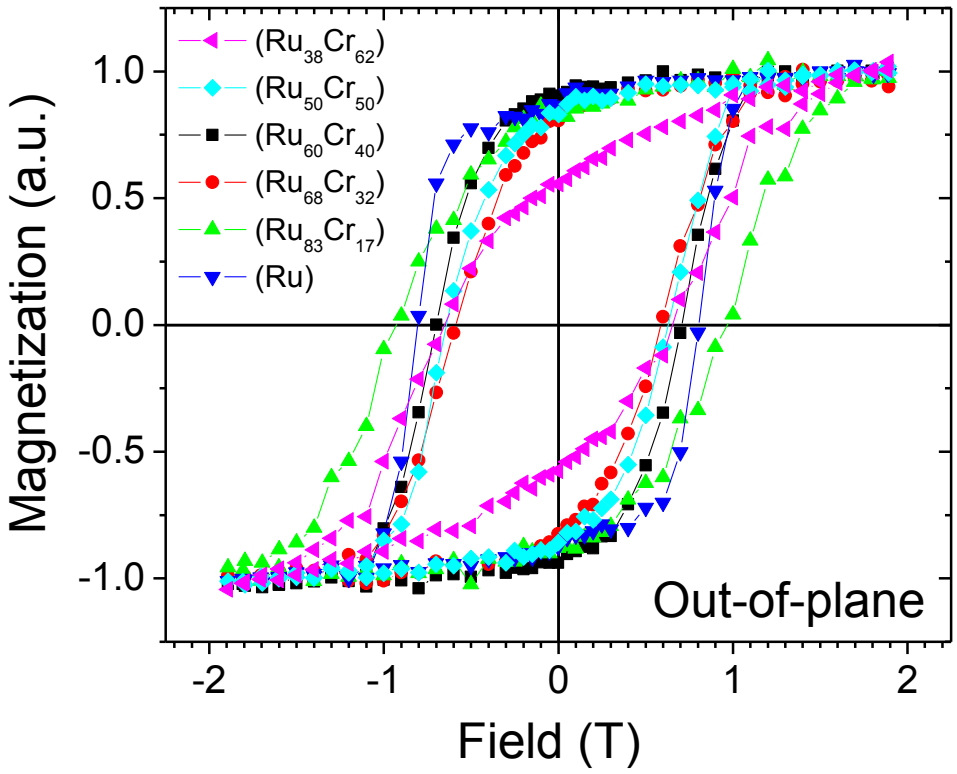

Figure 3.20 The out-of-plane magnetic hysteresis loops of $Sm(Co, Cu)_5$ thin films (20 nm) grown on the $Ru_{1-x}Cr_x$ underlayers ($0 \leq x \leq 0.62$).

Because of the relatively low Ms (~330 emu/cm^3) and thin thickness of $Sm(Co, Cu)_5$ films, the squareness ratio and intrinsic coercivity of our samples are sensitive to the background signals from either substrate or contaminations. However, the intrinsic switching field is not that sensitive to the linear background signals, so it is used to show the effect of Cr-doping on the magnetic hardness of the $Sm(Co, Cu)_5$ films grown on Ru(Cr) underlayers, as shown in Fig. 3.21.

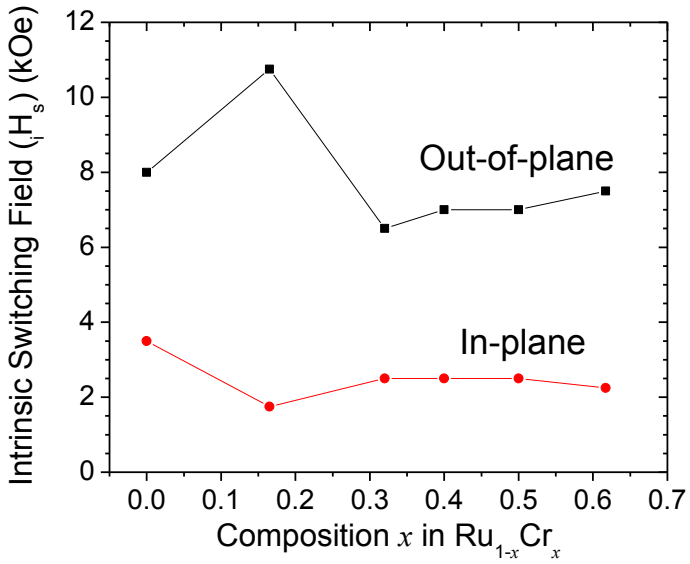

Figure 3.21 The out-of-plane intrinsic switching field of $Sm(Co, Cu)_5$ thin films (20 nm) grown on the $Ru_{1-x}Cr_x$ underlayers ($0 \leq x \leq 0.62$).

The $Sm(Co, Cu)_5$ film grown on the $Ru_{0.83}Cr_{0.17}$ underlayer shows a clear increase in the out-of-plane intrinsic switching field ($_iH_s$) (10.8 kOe vs. 8.0 kOe on Ru), as well as a decrease in the in-plane direction. However, further doping of Cr will lead to lower switching field. Therefore, a proper Cr doping in Ru(Cr) underlayer could improve the perpendicular anisotropy of $Sm(Co, Cu)_5$ films. It is not clear if this improvement is due to the slight lattice changes observed in the $Sm(Co, Cu)_5$ thin film (slightly smaller lattice constant *c* as shown in Fig. 3.19), because similar changes were also seen in other doping conditions. Another possibility would be the pinning effect of Cr atoms if they migrated into grain boundaries in the $Sm(Co, Cu)_5$ layer.

3.6 **Conclusion**

Polycrystalline Sm–Co–Cu films consisting mainly of highly (0001) textured $Sm(Co, Cu)_5$ grains have been fabricated successfully on highly (0002) textured and smooth Ru or Ru(Cr) underlayers which were grown on glass substrates with a Ta seed layer.

Consequently, good perpendicular anisotropy of $Sm(Co, Cu)_5$ thin films were achieved. Magnetization reversal is dominated by domain wall pinning mechanism as revealed by the initial magnetization curves and the angular dependence of coercivity. It was found that increasing Cu is like increasing deposition temperature - both could improve the $SmCo_5$ phase formation and the crystallinity of $Sm(Co, Cu)_5$ (0001) films. The thickness dependence of coercivities of Sm-Co-Cu films can be explained by combining the effects of the formation of misoriented grains in thicker films and more defects in thinner films, such as magnetic dead layer at the interface between the Sm–Co–Cu layer and Ru underlayer. The median compositions of nanocrystalline $Sm(Co, Cu)_5$ grains estimated from the structural parameters (e.g. unit volume, lattice constants *a* and *c*) and Curie temperature of the film matched reasonably well with each other. In-plane compressive strain, instead of tensile strain, is inferred in $Sm(Co, Cu)_5$ grains. The use of Ru(Cr) underlayer with a proper Cr doping could improve the perpendicular anisotropy of $Sm(Co, Cu)_5$ films. But it is not clear if this improvement is truly due to the slight lattice changes or pinning effect of Cr atoms in grain boundaries.

Chapter 4. Microstructure and Magnetization Reversal Mechanism of $Sm(Co, Cu)_5$ (0001) Thin Films

Summary

Previous chapter showed that magnetization reversal mechanism of $Sm(Co, Cu)_5$ thin films in this study is dominated by domain-wall pinning. In this chapter, microstructure study of pinning sites and further investigation on magnetization reversal details were presented. By using SEM, AFM, and TEM, various types of pinning sites have been identified, such as voids, grain/matrix boundaries (or crystalline/amorphous boundaries), grain boundaries between crystalline grains, and composition inhomogeneity in grains. $Sm(Co, Cu)_5$ grains are not as clearly defined as Ru grains. The grain size of Ru underlayer is about 10-30 nm, much smaller than that of Cu underlayer (~200 nm) reported in the literature. TEM elemental mapping analysis showed that Cu atoms were rich in the inner part of $Sm(Co, Cu)_5$ grains (defined by Sm and Co concentrations), instead of the outer part of grains, such as grain boundaries. Therefore, Cu served as an alloying element in $Sm(Co, Cu)_5$ grains, not as a doping element to form Cu-rich grain boundaries. A model of $Sm(Co, Cu)_5$ films with in-plane graded anisotropy due to composition/crystallization variation can explain the huge difference between the Hc and $H_{K,}$ and also the angular dependence of remanence coercivity of different Sm-Co-Cu layer thickness. A simple analytical expression of the angular dependence of switching field for graded media has been derived and shown to match well with experimental data of $Sm(Co, Cu)_5$ thin films in this study.

4.1 Introduction

$SmCo_5$ thin films are a promising candidate for extremely high areal density recording media because of their high magneto-crystalline anisotropy constant (Stmat

1988). Many studies have been carried out in recent years using either Cu underlayer or Ru underlayer (e.g. Sayama et al. 2004a and Takei et al. 2004). It has been reported that Cu doping helps stabilize the $SmCo_5$ phase rather than the Sm_2Co_{17} phase (Kamino et al. 1973 and Zhang et al. 2003). This effect could be the reason the perpendicular $SmCo_5$ thin films could be easily obtained on Cu underlayer. Although both the saturation magnetization value and anisotropy constant of $Sm(Co, Cu)_5$ decrease with the Cu addition, high anisotropy $Sm(Co, Cu)_5$ phase with a proper Cu concentration can still be formed (Lectard et al. 1994 and Tellez-Blanco et al. 1998). We reported that highly (0001) textured $Sm(Co, Cu)_5$ thin films with perpendicular anisotropy were successfully fabricated on Ru underlayer (Liu et al. 2008a and 2008b). Very large perpendicular anisotropic field (H_K ~ 200 kOe) but relatively small perpendicular coercivity (H_C ~ 10 kOe) were found in these films, where magnetization reversal had been determined to be a pinning-type domain wall switching. In this Chapter, microstructure study of pinning sites of highly (0001) textured $Sm(Co, Cu)_5$ thin films was presented.

4.2 Experiment

All layers of the films were deposited by an eight-target dc magnetron sputtering system with a base pressure of better than 1×10^{-7} Torr. Thin films with structure Ta(4.2 nm)\Ru(20 nm)\ $Sm(Co, Cu)_5$ (5–20 nm)\Ta(3 nm) were deposited onto glass substrates for characterizations of their structural and magnetic properties. The substrate temperature for the deposition of the $Sm(Co, Cu)_5$ layer and the Ta capping layer was 350°C, and all other layers were deposited at room temperature. $Sm(Co, Cu)_5$ layers were deposited by co-sputtering Sm, Co and Cu targets. All layers were deposited at an argon gas pressure of 3 mTorr.

The microstructure and composition of $Sm(Co, Cu)_5$ thin films were characterized by vibrating sample magnetometer (VSM), superconducting quantum interference device (SQUID) magnetometry, scanning electron microscopy (SEM), Atomic Force Microscopy (AFM), high-resolution transmission electron microscopy (HRTEM) using

plane-view, cross-section view, high-angle annular dark-field (HAADF) imaging and energy dispersive x-ray spectroscopy (EDS) elemental mapping.

4.3 Results and Discussion

4.3.1 Microstructure of $Sm(Co, Cu)_5$ (0001) Thin Films

Structural and magnetic properties of typical $Sm(Co, Cu)_5$ thin films on the Ta\Ru underlayer have been introduced in Section 3.3.1. Magnetization reversal of these films is dominated by domain wall pinning mechanism as revealed by the angular dependence of coercivity and remanence coercivity and other supporting evidences including initial magnetization curves, minor hysteresis loops, and the relationship between IRM remanence and DCD remanence. Now to have a better understanding of the pinning mechanism, we need to find out what types of the pinning sites exist in our films, and which type of pinning site is the dominant one.

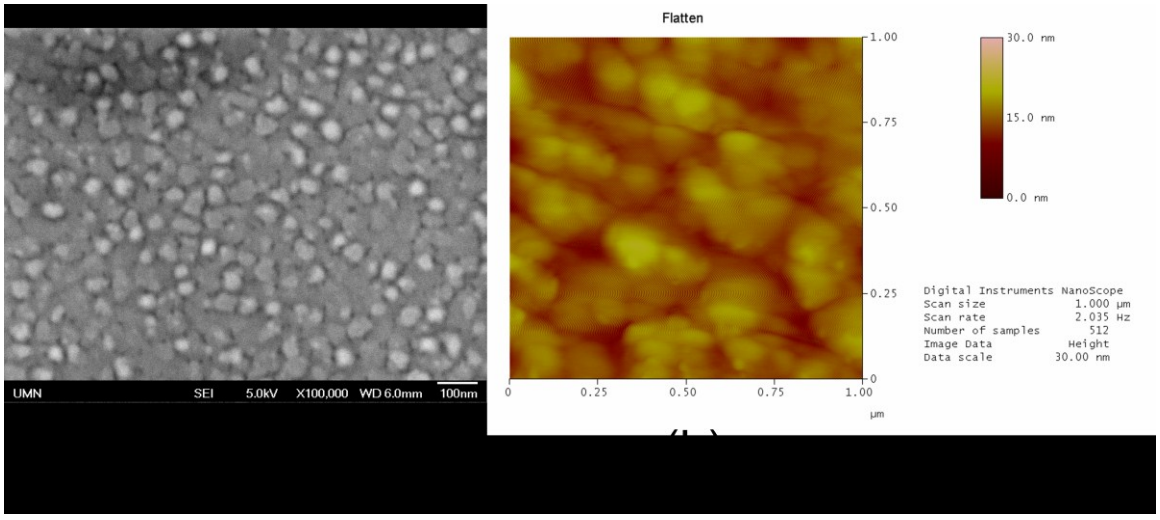

Figure 4.1 SEM (a) and AFM (b) image of $Sm(Co, Cu)_5$ thin films.

Fig. 4.1 (a) showed a typical SEM image of $Sm(Co, Cu)_5$ thin film (15 nm), where grains with sharp edges were embedded in the matrix of the film. There were many dark spots in the film, which were assumed to be voids. AFM image of $Sm(Co, Cu)_5$ thin film (20 nm), shown in Fig. 4.1 (b), also support the existence of voids between grains or

clusters of grains. The formation of voids was believed to be the result of islanded growth of the SmCoCu film on top of well-crystallized and highly (0001) textured Ru underlayer (Liu et al. 2008a). Both voids and grain/matrix boundaries in a magnetic thin film can serve as the pinning/nucleation sites in magnetic domain-wall switching. The grains and matrix might be corresponding to well-ordered and poorly-ordered (or amorphous) part, respectively, of the film.

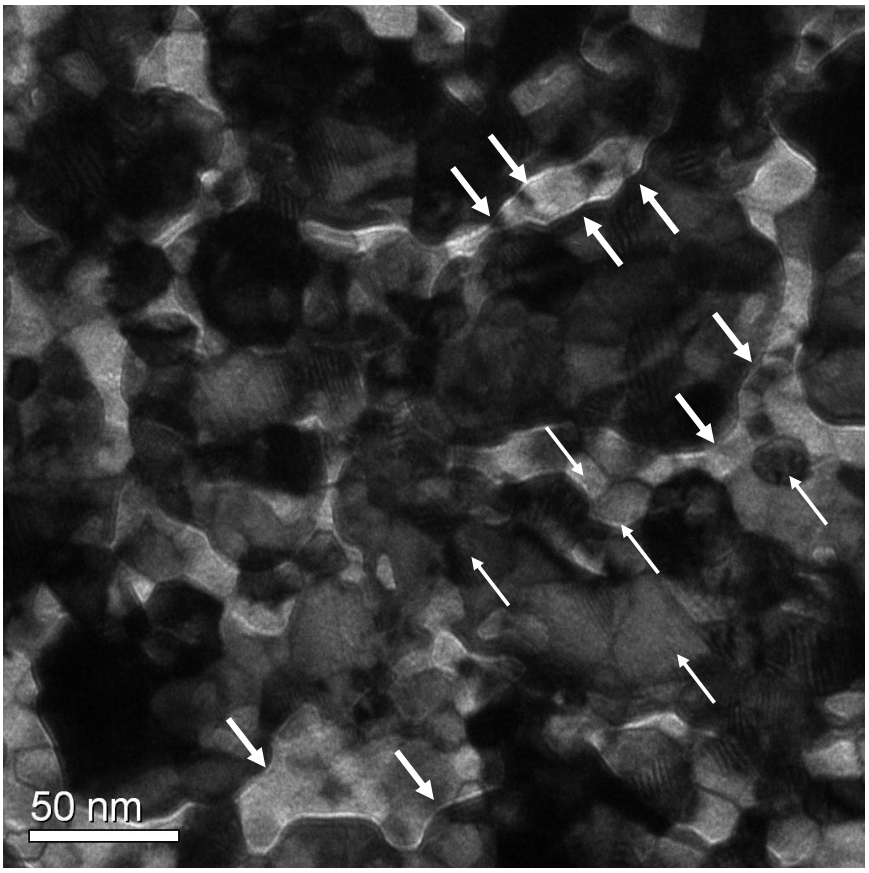

Figure 4.2 TEM plane view micrograph of the $Sm(Co, Cu)_5$ thin film with the structure of Ta(4.2 nm)\Ru(20 nm)\SmCoCu(20 nm)\Ta(3 nm).

The TEM plane-view micrograph of $Sm(Co, Cu)_5$ film (with the underlayers and the capping layer) also suggested the existence of voids. For example, brighter regions with curved but smooth boundaries in Fig. 4.2 (see the thick arrows) should be the voids. Those smaller faceted crystalline grains (10 – 30 nm in size, as pointed out by thin arrows)

are Ru grains, instead of $Sm(Co, Cu)_5$ grains, because this kind of microstructure is the typical microstructure of Ta\Ru underlayers (Shi et al. 2005), and it is consistent with our own TEM micrographs of underlayer samples (not shown here).

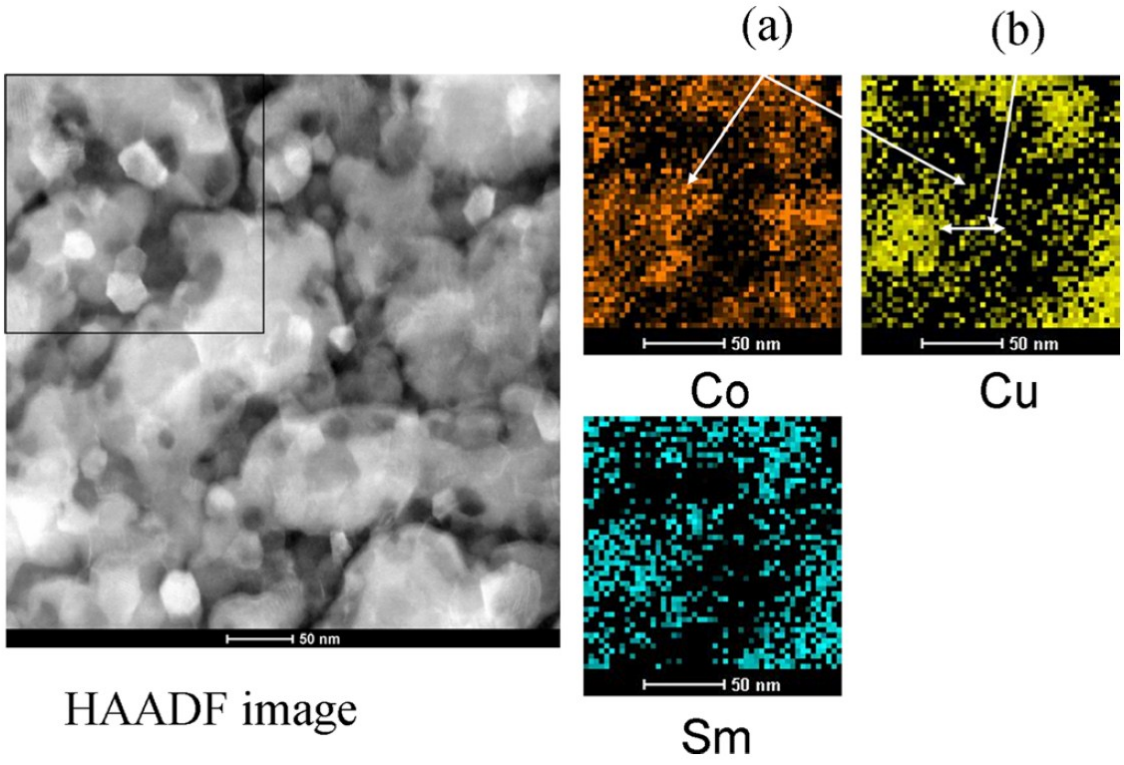

Figure 4.3 High-angle annular dark-field (HAADF) image and elemental mapping of $Sm(Co, Cu)_5$ thin film (20 nm) with Ta\Ru underlayers. The upper-left square box in the HAADF image indicates the region that was elementally mapped, and shown on the right. [Zhao et al. 2012]

Fig. 4.3 showed the HAADF image and the elemental mapping images of $Sm(Co, Cu)_5$ film (20 nm). The upper-left square box in the HAADF image indicates the region that was elementally mapped. The elemental mapping results of Sm, Co, and Cu were shown on the right. The HAADF image, which showed grains with similarly curved but smooth boundaries seen in the bright field image (Fig. 4.2), suggested that the film composition was not uniform across the surface. This is because HAADF image is also called Z-contrast image, which is highly sensitive to the variations in the atomic number of atoms in the area of interest. The wide black regions in elemental mapping images of

Sm, Co, and Cu indicated the place of voids. Indirect evidences of the voids such as that film became gradually thinner at boundaries were also observed in the cross-sectional TEM micrograph as shown in Fig. 4.4 (a) (see the white arrows).

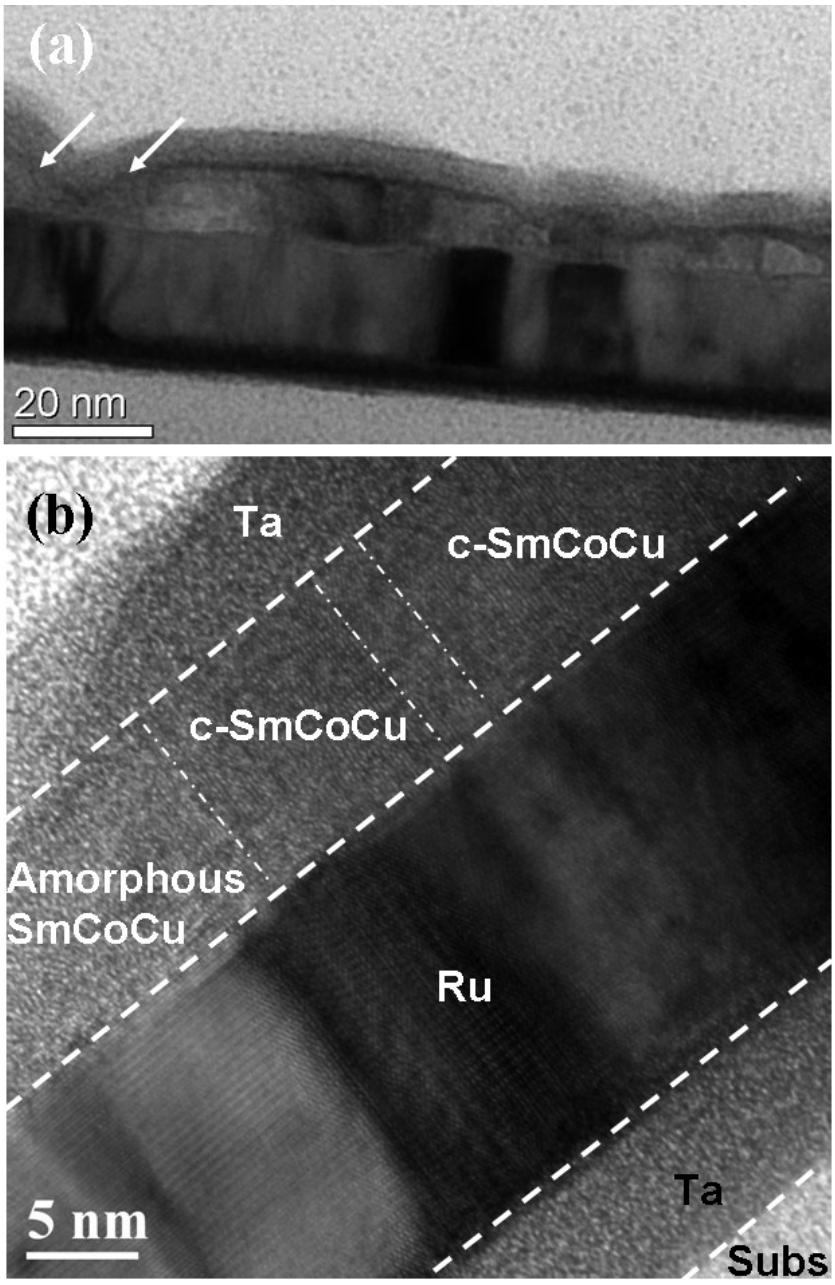

Figure 4.4 TEM cross-sectional micrographs of $Sm(Co, Cu)_5$ thin film (10 nm), where c-SmCoCu represents well-crystallized $Sm(Co, Cu)_5$ grain. [Zhao et al. 2012]

The inhomogeneous distribution of Sm, Co, and Cu atoms revealed the variation of film composition. As seen in Fig. 4.3, Sm and Co showed similar concentration pattern. However, Cu atoms were rich in the inner part of $Sm(Co, Cu)_5$ grains (defined by Sm and Co concentrations), instead of the outer part of grains, such as grain boundaries, as indicated by the arrows (a) in Fig. 4.3. This observation is contrary to our previous proposal (Liu et al. 2008b). It is also different from the result of $SmCo_5$ films grown on Cu underlayer, where the composition profiles of Co and Cu were totally mismatched (Takahashi et al. 2006). This finding clearly confirms that Cu serves as an alloying element in $Sm(Co, Cu)_5$ alloy since most of Cu stay in the inner part of $Sm(Co, Cu)_5$ grains, not as a doping element in $SmCo_5$ to form Cu-rich grain boundaries. This is consistent with the lattice constant changes of $Sm(Co, Cu)_5$ films measured in XRD patterns (Liu et al. 2008a and 2008b). It also suggests that the crystallization of $Sm(Co, Cu)_5$ films was inhomogeneous. It is reasonable to assume that the inner part of $Sm(Co, Cu)_5$ grains with more Cu are better crystallized than the outer part with less Cu (Liu et al. 2008a). Therefore, the anisotropy constant, K_u, is larger in the inner part of grains than the outer part of grains (boundaries). The gradual change of crystallization (caused by Cu composition variation) from the inner part of grains to boundaries will lead to a lateral graded K_u in SmCoCu grains. One possible reason for this composition and crystallization inhomogeneity is that the deposition temperature was not high enough for complete crystallization. The other reason might be a spontaneous phase separation (Cu-rich $Sm(Co, Cu)_5$ vs. Cu-deficient $Sm(Co, Cu)_5$).

The existences of amorphous (or poorly crystallized) regions in the $Sm(Co, Cu)_5$ films were also found in TEM cross-section micrographs. Fig. 4.4 (b) showed two well-crystallized $Sm(Co, Cu)_5$ grains separated by a narrow grain boundary. Amorphous SmCoCu region was seen at grain boundaries with thinner thickness, which suggested a higher deposition temperature might be needed for better crystallization of $Sm(Co, Cu)_5$ thin films.

Misoriented small grains are also observed in $Sm(Co, Cu)_5$ thin film (10 nm) under high-resolution TEM cross-section view, as shown in Fig. 4.5. These misoriented grains may be strongly exchange coupled to other perpendicular oriented grains so that the remanence in the in-plane direction is still negligible.

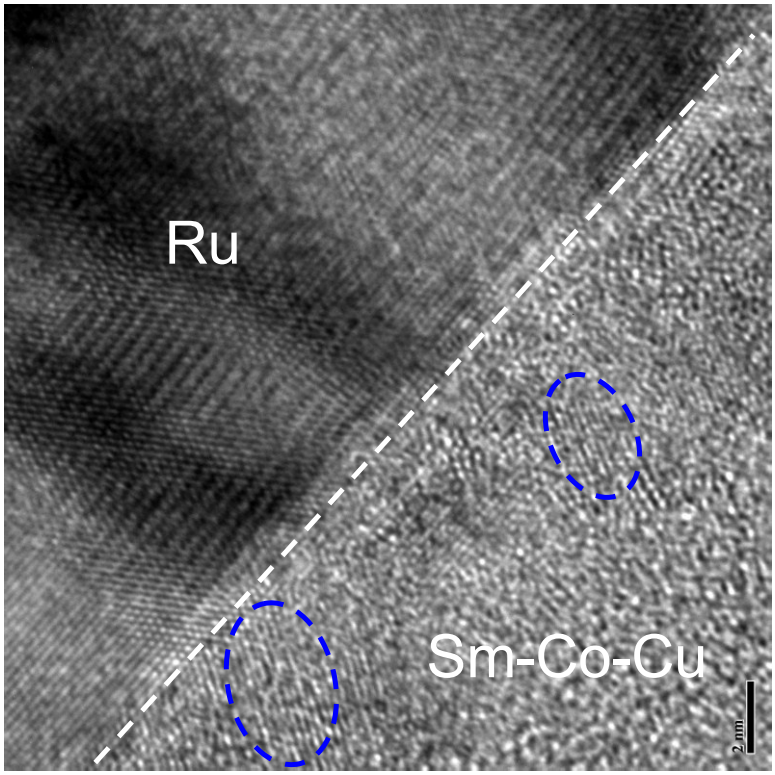

Figure 4.5 TEM cross-sectional micrographs of $Sm(Co, Cu)_5$ thin film (10 nm), where misoriented grains are highlighted by dash ellipses.

4.3.2 **Magnetization Reversal Mechanism of $Sm(Co, Cu)_5$ (0001) Thin Films**

Magnetization reversal by domain wall movement is known to reduce the coercivity in hard magnetic materials significantly. For the $Sm(Co, Cu)_5$ films in our study, it has been shown in the previous section that an in-plane graded K_u from grain core to grain boundary, with a characteristic length of about 40 nm, could be likely the major pinning mechanism. In the following, we will try to calculate the switching field based on this assumption to see if it makes sense.

A. Switching field estimation in graded media when field angle is 0°

Fig. 4.6 showed a schematic drawing of $Sm(Co, Cu)_5$ films with lateral graded anisotropy due to composition/crystallization variation. The variation of the arrow length represents the variation of perpendicular anisotropy of $Sm(Co, Cu)_5$ regions. Using equations in Kronmüller and Goll (2002) and Suess et al. (2008), the reduction of H_C due to lateral quadratically graded anisotropy in the film can be estimated:

$$H_S = \frac{4\sqrt{AK(L)}}{M_S(2L - l_D)} \tag{4.1}$$

For example, given the parameters in our experiments (M_S – 330 emu/cm^3, H_K – 200 kOe, and exchange constant (A) – 6.0x10^{-7} erg/cm), the width of the transitional region for the H_S of 8.0 kOe is about 36 nm, which is about the same as the width of Cu concentration variation found in elemental mapping image (Fig. 4.3, arrow (b)). Therefore, the in-plane graded K_u model did give a fairly good prediction on the length of graded K_u region or the switching field at the 0° field angle. To further test this model, we will look at the case when field angle > 0°.

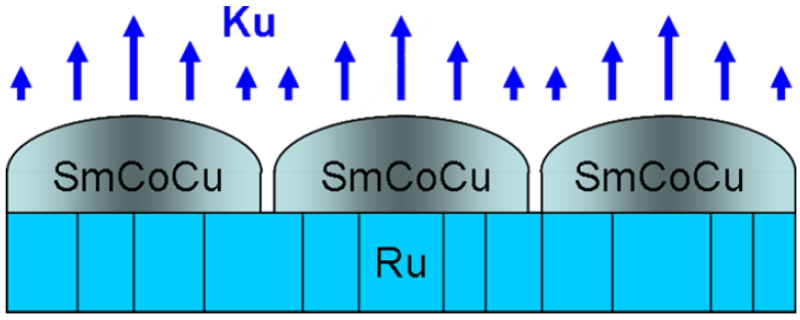

Figure 4.6 Schematic drawing of a $Sm(Co, Cu)_5$ thin film with lateral graded anisotropy grown on the Ru underlayer. The variation of the length of arrows represents the variation of perpendicular anisotropy of $Sm(Co, Cu)_5$ regions. [Zhao et al. 2012]

B. Angular dependence of coercivity and remanence coercivity in $Sm(Co, Cu)_5$ thin films

Fig. 4.7 showed the angular dependence of coercivity and remanence coercivity in $Sm(Co, Cu)_5$ thin films with different thickness. The remanence curves have been experimentally fitted with an empirical equation

$$H_{cr}(\theta) = H_{cr}{}^{0} \frac{1}{[1+\beta(Cos(\theta)-1)]}. \qquad (4.2)$$

This equation fits pretty well for all samples when the field angle is less than or equal to 50°. For the $Sm(Co, Cu)_5$ thin film of 5 nm, it fits reasonably well for all field angles (up to 80°). It is interesting to find out if this is just a coincidence, or it is dictated by the intrinsic properties of the $Sm(Co, Cu)_5$ thin films.

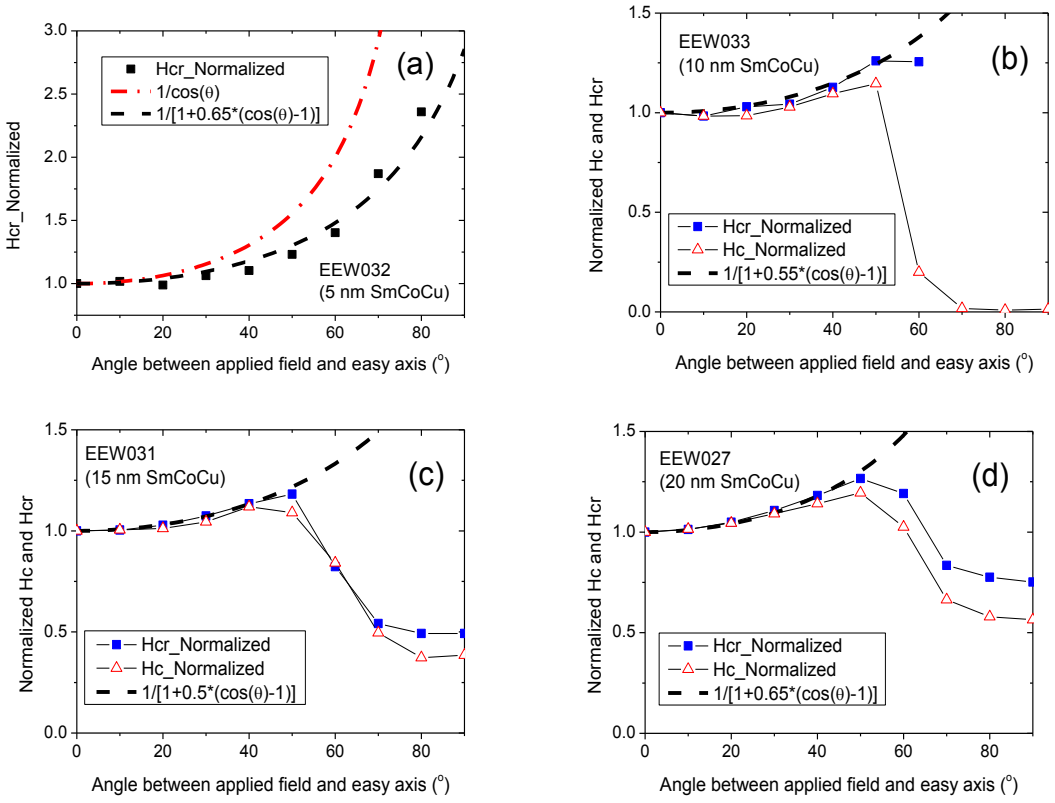

Figure 4.7 Angular dependence of coercivity and remanence coercivity of $Sm(Co, Cu)_5$ thin films with different thickness.

For the decrease of coercivity and remanence coercivity when the field angle is larger than 50°, it is believed that those *Hc* and *Hcr* values are not true properties of the perpendicularly oriented grains. Because at those high angles, the magnetic moment detected by VSM from the perpendicularly oriented grains will be smaller than the magnetic moment from the misoriented and amorphous grains, which is also related to the limited maximum applied field in VSM (~ 17 kOe).

C. Switching field estimation in graded media when field angle is > 0°

Following the approach used by Suess et al. (2008), Fig. 3.8 illustrates magnetic states (A) - (D) along the minimum energy path (MEP) and their energies for a graded thin film whose easy axis is out-of-plane (*y*-direction) but Ku increases quadratically along *z*-direction.

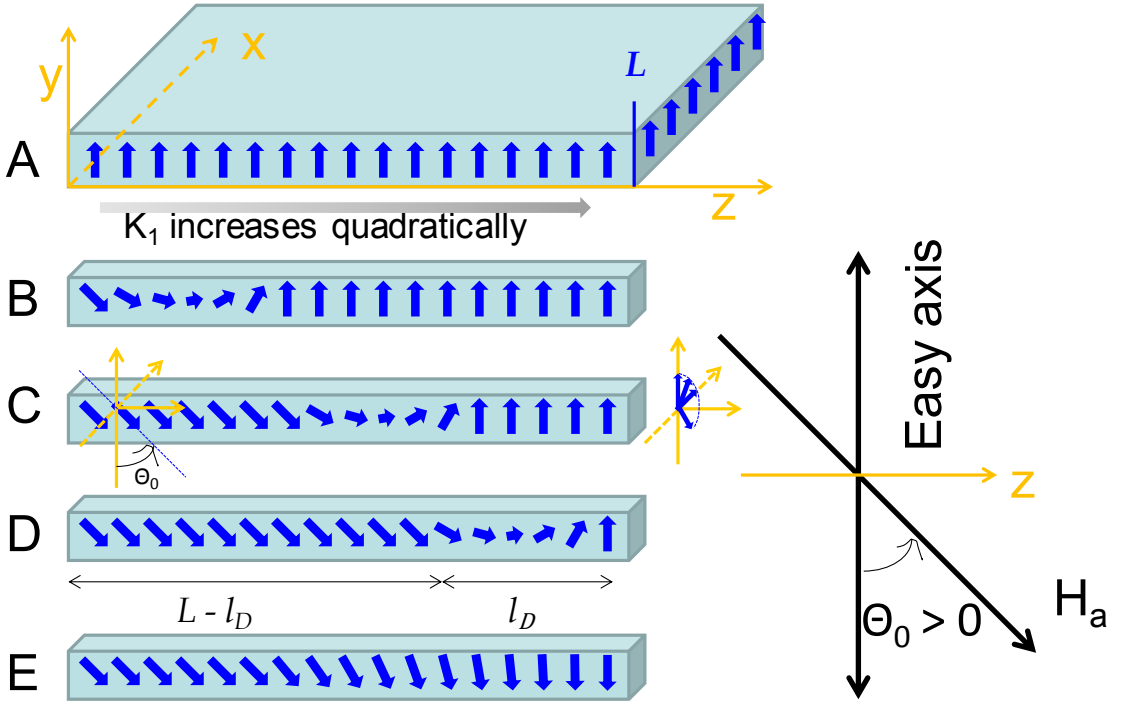

Figure 4.8 Schematic drawing of magnetic configurations along the minimum energy path (MEP) for a graded media with quadratically increasing anisotropy from the left to the right when the external field is at an angle to the easy axis.

The states (A) - (D) correspond to the initial state (A), the state of nucleation of the domain wall at the soft side of the film (B), the intermediate state where the reversed domain propagates toward the hard side (C), and the saddle point which has the highest energy configuration (D). The energy barrier is the energy difference between the state (A) and the state (D).

In simple estimation, the demagnetization energy is ignored. The energy of the initial state is

$$E_1 = LFM_SHCos(\theta_0)\,. \tag{4.3}$$

Here, the *L* is the length of graded *Ku* region along the z-direction, *F* is the cross section, *Ms* is the saturation magnetization (assumed to be constant across the film), *H* is the applied external field, and θ_0 is the angle between the applied field and easy axis.

The energy of the state (D) is

$$E_2 = 4F\sqrt{AK(L)} - (L - l_D)FM_SH\,, \tag{4.4}$$

where *A* is the exchange constant, *K(L)* is the anisotropy constant at hard end, l_D is the domain wall width (= $\pi\sqrt{A/K(L)}$). Here, we also assumed the domain wall energy is no different from where the field angle (θ_0) is 0°.

Therefore, the energy barrier is

$$\begin{aligned}\Delta E &= E_2 - E_1 \\ &= 4F\sqrt{AK(L)} - (L - l_D)FM_SH - LFM_SHCos(\theta_0) \\ &= 4F\sqrt{AK(L)} - FM_SH[(2L - l_D) + LCos(\theta_0) - L] \\ &= 4F\sqrt{AK(L)} - FM_SH(2L - l_D)[1 + \tfrac{L}{(2L-l_D)}(Cos(\theta_0) - 1)].\end{aligned} \tag{4.5}$$

Solving $\Delta E(H_S) = 0$ for $H_S(\theta_0)$, we obtain

$$H_S(\theta_0) = \frac{4\sqrt{AK(L)}}{M_S(2L-l_D)}\frac{1}{\left[1+\frac{L}{(2L-l_D)}(Cos(\theta_0)-1)\right]}. \tag{4.6}$$

Or it can be simplified as

$$H_S(\theta_0) = {H_S}^0\frac{1}{[1+\beta(Cos(\theta_0)-1)]}, \tag{4.7}$$

where $$H_S{}^0 = \frac{4\sqrt{AK(L)}}{M_S(2L-l_D)}, \tag{4.8}$$

and $$\beta = \frac{L}{2L-l_D} \quad \text{or} \quad \beta = \frac{1}{2-(l_D/L)} \quad . \tag{4.9}$$

Eq. (4.7) is the same as the Eq. (4.2) ($H_S \sim H_{cr}$). So this is not a coincidence. $H_S{}^0$ is the same as seen in Eq. (4.1). The factor β has a physically meaning - it is a factor of the ratio of the domain-wall width to the width of graded region. The larger domain-wall width with respect to the graded region width, the larger β. The range of β is between 0.5 and 1.

β near 0.5 means the domain-wall width is infinite small compared to the graded region width, which might be achieved if a) very small domain-wall width due to ultra large Ku at the hard end (small l_D), or b) very wider transition region (large L). When β = 1, the Eq. (4.7) is exactly the same as the Kondorsky function ($H_{cr}(\vartheta) \sim 1/\cos(\vartheta)$). Fig. 4.9 plots the impact of β factor on the angular dependence of switching field in grade media.

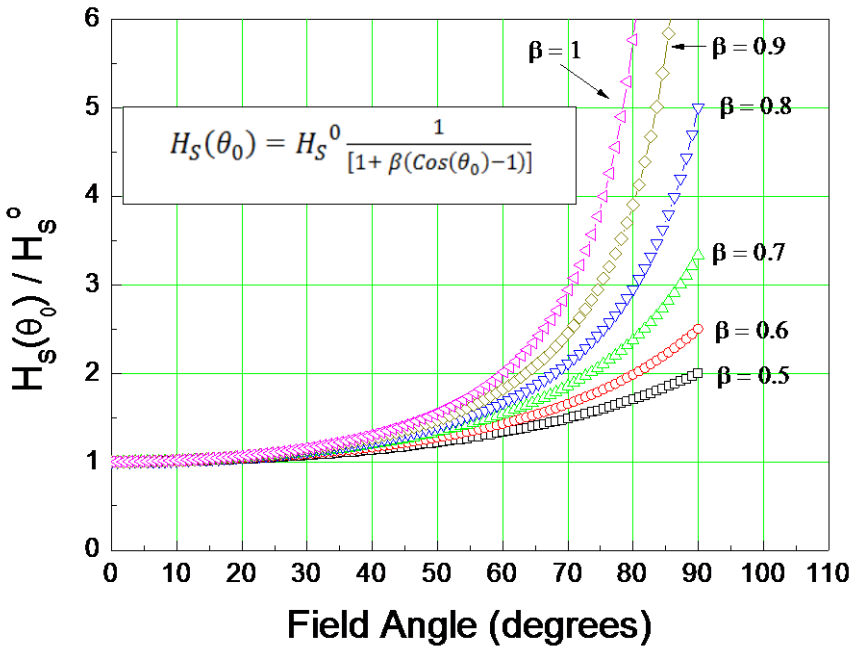

Figure 4.9 The impact of β on the angular dependence of switching field in graded media.

Given the physical interpretation of the factor β, we can analyze the angular dependence of remanence coercivity of $Sm(Co, Cu)_5$ thin films with different thickness. As shown in Fig. 4.10, β decreases first with an increase of thickness, up to 15 nm, which might be indicating a decreasing domain-wall width, or increasing anisotropy constant, while the graded region width is kept about same. For the increase of β at 20 nm w.r.t. to 15 nm, since it is not likely due to Ku decrease, it might be due to the decrease of graded region width, as the reduction of voids and grains become more densely packed which might lead to less composition/crystallization variations.

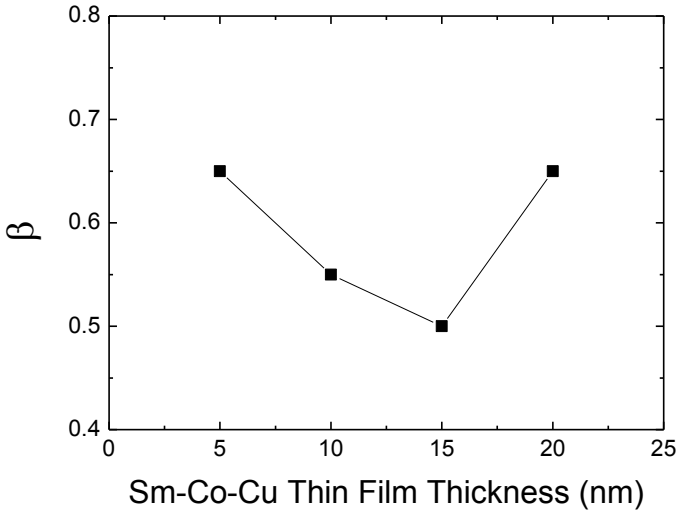

Figure 4.10 The β of $Sm(Co, Cu)_5$ thin films with different thickness.

4.4 **Conclusion**

Through the analyses of SEM, AFM, and TEM, various types of pinning sites in highly (0001) textured $Sm(Co, Cu)_5$ thin films have been identified. The major pinning type that could substantially affect the *Hc* is the composition gradient of Cu in the $Sm(Co, Cu)_5$ layer. TEM elemental mapping analysis showed that Cu atoms were rich in the inner part of $Sm(Co, Cu)_5$ grains or particles, instead of the outer part, such as grain boundaries or edges of voids. Cu served as an alloying element in $Sm(Co, Cu)_5$ grains, not as a doping element to form Cu-rich grain boundaries. A model of $Sm(Co, Cu)_5$ films with in-

plane graded anisotropy due to composition/crystallization variation can explain the huge difference between the *Hc* and H_K as well as the angular dependence of remanence coercivity of $Sm(Co, Cu)_5$ thin films. A simple analytical expression of the angular dependence of switching field for graded media has been derived and shown to match well with experimental results.

Chapter 5. Chemical Stability of $Sm(Co, Cu)_5$ (0001) Thin Films

Summary

With the highest magnetocrystalline anisotropy constant (Ku) among practical magnetic materials, $SmCo_5$ could be a very attractive candidate for future high areal density magnetic recording. However, its corrosion resistance is always a concern in recording media applications. In this Chapter, the chemical stability and microstructures of highly (0001) textured $Sm(Co, Cu)_5$ thin films with and without a 3 nm Ta capping layer were reported. For $Sm(Co, Cu)_5$ thin films without a capping layer, the coercivity decreases significantly (from 8kOe to 1kOe) within one month. $Sm(Co, Cu)_5$ thin films capped with a thin Ta layer (3 nm) behave differently. Even exposed to a laboratory environment (25 °C) over 3 years, the Ta-capped $Sm(Co, Cu)_5$ thin films are stable in terms of structural and magnetic properties, i.e. there were no changes in X-ray diffraction peaks and vibrating sample magnetometer hysteresis loops. Microstructure of Ta-capped $Sm(Co, Cu)_5$ thin films showed that $Sm(Co, Cu)_5$ formed a domelike particle assembly structure on a smooth Ru underlayer and were well covered by partially oxidized Ta capping layer, as shown by TEM cross-section micrographs. Accelerated corrosion treatment (130°C, 95% relative humidity, 6 h) was performed on Ta-capped $Sm(Co, Cu)_5$ thin films. X-ray photoelectron spectroscopy (XPS) results showed that no Co was detected on the sample surface before the corrosion treatment, but strong XPS signals of CoO_x and $Co(OH)_x$ were observed after treatment. Therefore, none of our $Sm(Co, Cu)_5$ thin films can pass the accelerated corrosion test. Hcp-phased CoPt-alloys with carbon overcoat are proposed as better capping materials for $Sm(Co, Cu)_5$ thin films in future high-density magnetic recording applications.

Introduction

The magnetocrystalline anisotropy constant (Ku) of $SmCo_5$ is the highest among practical magnetic materials (Weller et al. 2000), which makes it an attractive candidate for future high areal density magnetic recording media. Sm-Co thin film usually needs a thick capping layer such as Cr, to prevent it from oxidation and corrosion (Velu and Lambeth 1992). Some recent studies of Sm-Co-Cu thin film suggested that its corrosion resistance might be good enough for recording media applications (Sayama et al. 2005a). Therefore, there is no consensus so far on whether the high Ku $SmCo_5$ phase can be used as recording medium. In previous chapters, it was shown that highly (0001) textured $Sm(Co, Cu)_5$ thin films with high perpendicular magnetic anisotropy can be grown on Ru underlayer. To study the potential application of the highly (0001) textured $Sm(Co, Cu)_5$ thin films for future magnetic recording media, we need to investigate the chemical stability of the films. In this chapter, the chemical stability and microstructures of highly (0001) textured $Sm(Co, Cu)_5$ thin films with and without a 3 nm Ta capping layer are presented.

5.2 Experiment

All layers of the films were deposited by an eight-target dc magnetron sputtering system with a base pressure of better than 1×10^{-7} Torr. Thin films with structure Ta(4.2 nm)\Ru(20 nm)\Sm–Co–Cu(5–20 nm)\Ta(3 nm) were deposited onto glass substrates. The substrate temperature for the deposition of the Sm–Co–Cu layer and the Ta capping layer was 350°C, and all other layers were deposited at room temperature. Sm–Co–Cu layers were deposited by co-sputtering Sm, Co and Cu targets. All layers were deposited at an argon gas pressure of 3 mTorr, unless otherwise specified. The structural and magnetic properties of samples were characterized by Cu source x-ray diffractometer (XRD), vibrating sample magnetometer (VSM), and transmission electron microscopy (TEM), respectively. XPS was employed to study sample surface products after the accelerated corrosion test.

5.3 Results and Discussion

The chemical stability of $Sm(Co, Cu)_5$ thin films with or without the Ta capping layer were first investigated by studying the structural and magnetic properties of samples after exposure in a laboratory environment (1 atm, 25°C, < 50% humidity) for a long time. These results should be taken only as a qualitative estimation of the chemical stability because the laboratory environment is considered to be a normal air-conditioned atmosphere, which can vary a lot in terms of the humility and impurities present in the atmosphere.

$Sm(Co, Cu)_5$ thin films without a Ta capping layer degraded quickly. For example, the coercivity of a 15 nm $Sm(Co, Cu)_5$ thin film would decrease from 8 kOe to 1 kOe within one month, while the total magnetic moment of the film increased a little. A simple and direct explanation is that the products of the oxidation and corrosion of $Sm(Co, Cu)_5$ thin films, [including CoOx and Co(OH)x, as shown in later XPS results], are soft magnetic phases with larger magnetic moments per magnetic atoms. It is possible that in degraded $Sm(Co, Cu)_5$ thin films, oxygen diffused into the film, broke the symmetry of the $SmCo_5$ lattice by generating more defects, and led to more localized 3d electrons in Co atoms. Therefore, reduced magnetic anisotropy and enhanced magnetic moment could be achieved at the same time in degraded $Sm(Co, Cu)_5$ thin films, as results of oxidation and corrosion.

$Sm(Co, Cu)_5$ thin films with the Ta capping layer (3 nm) have totally different chemical stability. As shown in Fig. 5.1, the XRD spectrum of $Sm(Co, Cu)_5$ thin film (20 nm) after exposure in air for 18 months under normal laboratory environment (1 atm, 25°C, < 50% humidity), had no change compared to that of the as-prepared film. Comparison of hysteresis loops of the same samples is shown in Fig. 5.2. No clear degradation of magnetization or coercivity was observed. Surface morphology was also examined by atomic force microscopy (AFM). No corrosion spots were observed by AFM. Similar results were obtained in $Sm(Co, Cu)_5$ thin films with different thickness, as shown in Table 1.

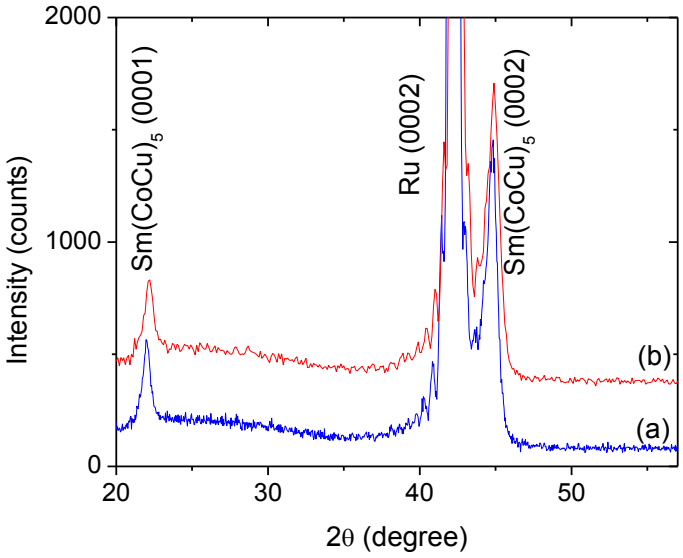

Figure 5.1 XRD spectra of $Sm(Co, Cu)_5$ thin film (20 nm): (a) as-deposited; (b) after exposure for 18 months in the laboratory environment.

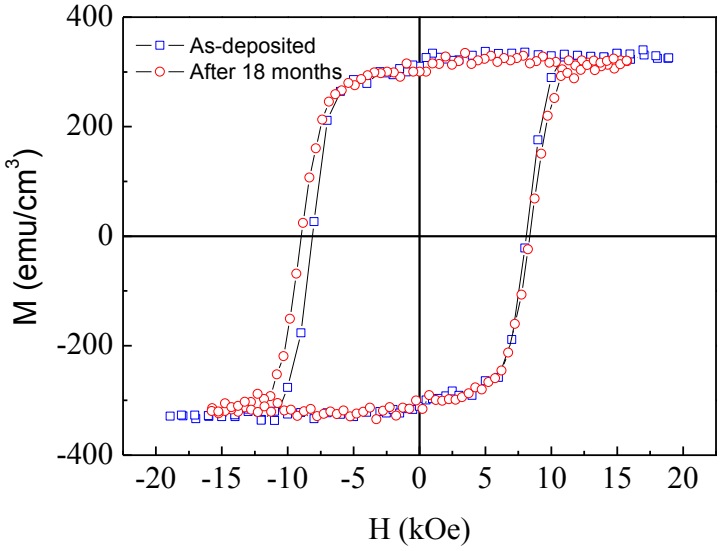

Figure 5.2 Hysteresis loops of $Sm(Co, Cu)_5$ thin film (20 nm) of as-deposited or after exposure for 18 months in the laboratory environment

Table 5.1 Crystal structure data and Curie temperatures of Sm-Co phases.

	Sm-Co-Cu film thickness							
	5 nm		10 nm		15 nm		20 nm	
Exposure time (months)	Ms (emu/cm^3)	Hc (kOe)	Ms (emu/cm^3)	Hc (kOe)	Ms (emu/cm^3)	Hc (kOe)	Ms (emu/cm^3)	Hc (kOe)
0	274	4.2	328	10.7	332	7.8	335	8.2
18	270	4.2	328	9.5	323	8.2	329	8.7
36			325	9.6	321	7.6	328	8.8

To understand the effect of 3 nm Ta capping layer on the chemical stability of $Sm(Co, Cu)_5$ thin films, the microstructure of a typical sample was examined by cross-section TEM imaging. Fig. 5.3 showed the layer structure of $Sm(Co, Cu)_5$ thin film and a typical cross-section TEM micrograph of the 10 nm $Sm(Co, Cu)_5$ thin film. $Sm(Co, Cu)_5$ thin film are found to consist of domelike particles grown on a relatively smooth Ru underlayer. $Sm(Co, Cu)_5$ particles were well covered by the Ta capping layer. The Ta capping layer appeared more transparent than the bottom Ta seed layer, which suggests that oxidation must have happened in the Ta capping layer. This is also consistent with the TEM observation that the actual thickness of Ta capping layer (~ 4nm) is larger than the nominal thickness (3 nm).

Chemically unstable $Sm(Co, Cu)_5$ thin films with 3 nm Ta capping layer were also observed in our experiments if the top part of Ru underlayer (about 4 nm) was prepared under higher pressure (e.g. 6 mTorr). For example, one sample prepared under this condition showed relatively fast degradation of coercivity, i.e. from 11 kOe to 8.8 kOe after one month, and to 2.6 kOe after 18 months under normal laboratory environment conditions. The Ru underlayer prepared under higher pressure will generate many void boundaries and its surface becomes rough (Shi et al. 2005). $Sm(Co, Cu)_5$ thin films grown on a rougher Ru underlayer should have a rougher surface as well. Here a rougher surface means a larger surface area. Therefore, with the same amount of Ta capping materials, Ta thickness would become thinner on a rough surface than on a smooth

surface. This is why we saw accelerated oxidation/corrosion in $Sm(Co, Cu)_5$ thin films grown on high-process-pressure Ru underlayer.

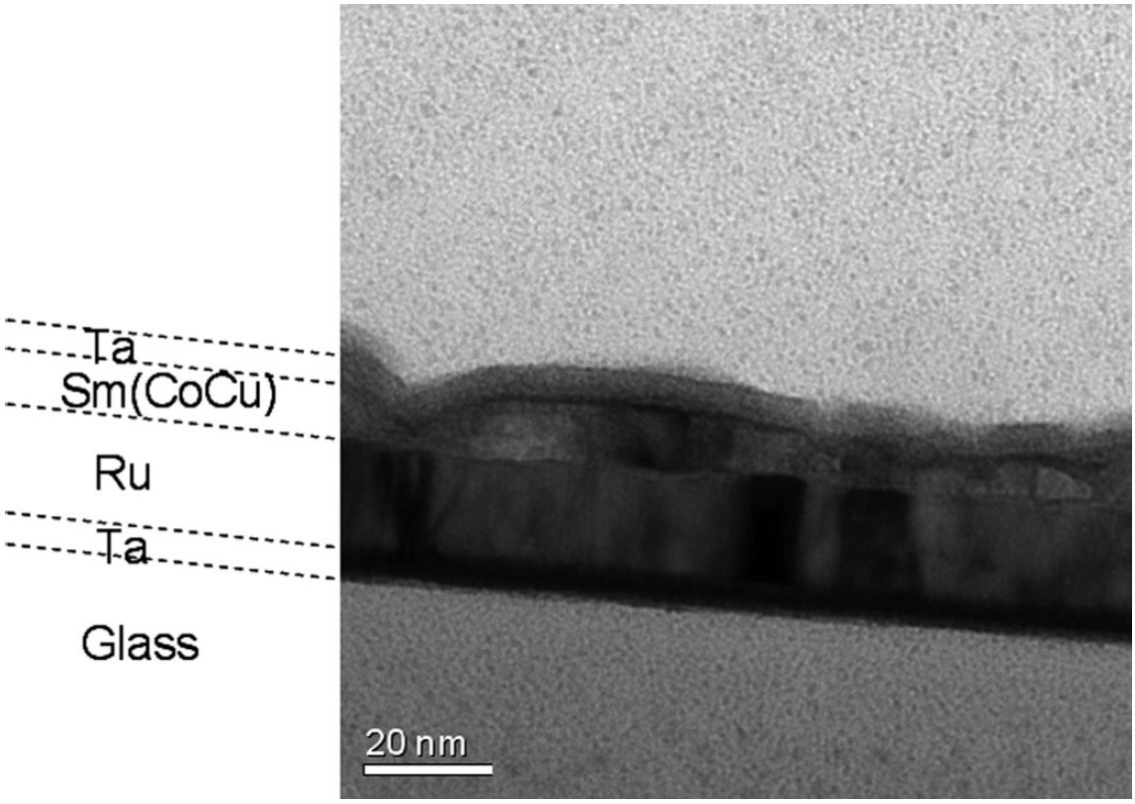

Figure 5.3 The layer structure and TEM micrograph of cross section view of Sm(Co, $Cu)_5$ thin film.

To further evaluate the quality of 3 nm Ta capping layer for oxidation/corrosion protection, an accelerated corrosion test on $Sm(Co, Cu)_5$ thin films (stable under normal conditions) was performed under constant temperature (130°C) and humidity (95%) for a long time (6 h). These parameters are chosen to meet the requirements of hard disk recording media, which can guarantee normal operation for three years under normal Hard Disk Drives (HDD) environment. XPS was employed to study the surface oxidation and corrosion. XPS results are shown in Fig. 5.4. No Co element was detected on the sample surface before the corrosion treatment, but strong XPS signals of CoOx and

Co(OH)x were observed after treatment. It is clear that a 3 nm Ta capping layer cannot make the $Sm(Co, Cu)_5$ thin film pass the corrosion test.

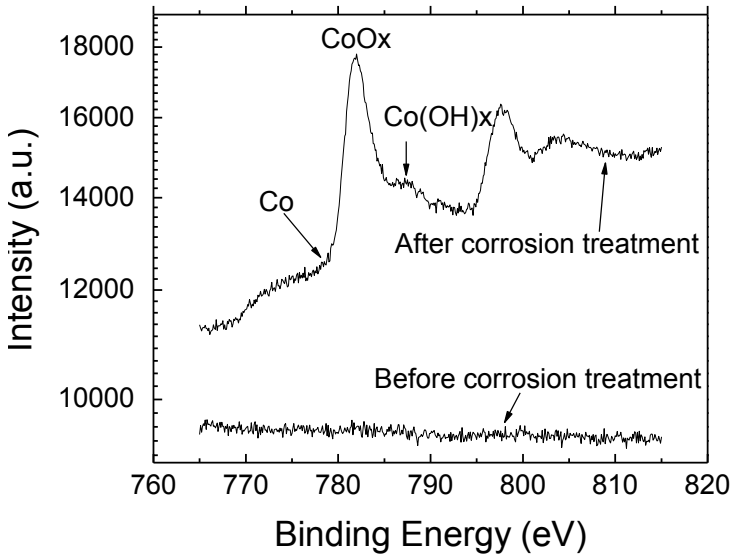

Figure 5.4 XPS spectra of SmCoCu thin film before and after corrosion treatment.

Our highly (0001) textured $Sm(Co, Cu)_5$ thin films seemed to be more chemically unstable comparing to the Sm-Co thin films reported by Sayama et al. (2005a), where their Sm-Co films were found to possess corrosion resistance equal to a $CoCr_{19}$ film. One possible reason is the composition difference between two types of films. The other possible reason could be due to the different microstructures. The Sm-Co films studied by Sayama et al. (2005a) were prepared by laminating Sm and Co sublayers alternatively, which may lead to better crystallinity of the Sm-Co films. In our highly (0001) textured $Sm(Co, Cu)_5$ thin films, however, there might exist many amorphous regions (Zhao et al. 2012) where oxidation and corrosion happen more easily.

In modern magnetic recording applications, a non-magnetic capping layer over magnetic recording media is one of the major components of head-media spacing, which leads to magnetic signal loss. A magnetic capping layer is necessary for $Sm(Co, Cu)_5$ thin films to be considered as a candidate for future high-density magnetic recording. Because

hcp-phased CoPt-alloy grains can be grown epitaxially on $CaCu_5$-type $Sm(Co, Cu)_5$ layer, a capping layer structure consisting of a hcp-phased CoPt-alloy sublayer and a carbon overcoat sublayer should protect $Sm(Co, Cu)_5$ thin films well to meet the requirements for magnetic recording media applications.

5.4 Conclusion

$Sm(Co, Cu)_5$ thin films without a capping layer showed fast degradation under normal conditions (1 atm, 25°C, < 50% humidity). $Sm(Co, Cu)_5$ thin films with a nominal 3 nm Ta capping layer but grown on high-process-pressure Ru underlayer also showed relatively fast degradation. Only those $Sm(Co, Cu)_5$ thin films with a nominal 3 nm Ta capping layer that were grown on a smooth Ru underlayer are stable under normal conditions in terms of magnetic and microstructural properties. However, no $Sm(Co, Cu)_5$ thin films can pass the accelerated corrosion test, which was designed for qualifying hard disk recording media in HDD applications. A capping layer consisting of a hcp-phased CoPt-alloy layer and a carbon overcoat would help $Sm(Co, Cu)_5$ thin films meet the requirements for future high-density magnetic recording applications.

Chapter 6. Exchange Coupled Composite (ECC) FePt Media

Summary

Ultra-thin exchange coupled composite (ECC) FePt granular recording media with different soft layer anisotropy were fabricated by controlling the soft layer deposition temperature. The sample structure is glass_sub/CrRu(30 nm)/MgO(3.6 nm)/FePt(3 nm, hard)/FePt-SiO_2(4 nm, soft). It was found that magnetic properties of the magnetically hard layer (FePt 3 nm) remained relatively stable under annealing up to 400 ^oC, 2 h in vacuum. As the soft layer (FePt-SiO_2) deposition temperature (T_{Soft}) increased, the overall FePt (001) texture of ECC FePt thin films was improved, while the saturation magnetization (Ms) and the thermal stability factor were also increased. The effect of soft layer anisotropy field on the coercivity (Hc) and the remanent coercivity (Hcr) of ECC FePt thin films showed a "V" shape relationship, with the minimums at T_{Soft} of 200 ^oC. These results are consistent with the theoretic prediction based on domain wall assisted magnetization reversal mechanism. The ECC FePt thin film with T_{Soft} of 200 ^oC may have a gain factor larger than 2.

6.1 Introduction

Exchange coupled composite (ECC) media was proposed and demonstrated to deal with the writability issue in high-density magnetic recording (Victora et al. 2005 and Wang et al. 2005), so as to extend the lifetime of current perpendicular magnetic recording technology. Co-alloy based ECC disk media has been demonstrated to show better recording performance than conventional perpendicular media (Wang et al. 2007). The replacement of Co alloy by $L1_0$-FePt alloy will reduce the recording layer thickness, which may improve the writing field gradient. In this chapter, the fabrication of $L1_0$-FePt based ECC media with ultra-thin recording layer is reported.

In ECC media, the gain factor, which is defined as $\xi \equiv 2\Delta E/(Hs \bullet Ms \bullet V)$ (Victora et al. 2005), determines the potential of the media. The initial theoretical calculations based on the two-layer approximation of ECC structure (Victora et al. 2005) suggested that the gain factor has a maximum value of 2. Further studies on ECC structure showed that the gain factor can be larger than 2, if the magnetization reversal mechanism is domain wall assisted switching (Robin et al. 2006 and Suess et al. 2008). Simulation results (Robin et al. 2006 and Hagedorn et al. 1970) predicted a unique feature of domain wall assisted switching in ECC structure: the dependence of the media switching field on the soft layer anisotropy field exhibits a "V" shape relationship, i.e. the switching field decreases at first and then increases after passing a minimum. In other words, there is an optimum value of the soft layer anisotropy field, which can achieve the lowest switching field, or the largest possible gain factor in the two-layer structured ECC media.

In this study, we investigated the influence of soft layer anisotropy field on the $L1_0$-FePt based ECC media. The sample structure is glass_sub/CrRu(30 nm)/MgO(3.6 nm)/FePt(3 nm)/FePt-SiO_2(4 nm). The FePt hard layer with granular structure was prepared on MgO layer (Zhao et al. 2006 and Chen et al. 2007). The prepared hard layer was cooled down to room temperature. Then a granular soft layer FePt-SiO_2 was deposited on top of the prepared hard FePt layer. SiO_2 grain boundaries were expected to be formed in voids of FePt hard layer. The variation of the soft layer anisotropy field was achieved by changing the deposition temperature. The effect of soft layer deposition temperature (or soft layer anisotropy field) of ECC FePt media was investigated systematically.

6.2 Fabrication of ECC FePt Media

All layers of the films were deposited by an eight-target DC/RF magnetron sputtering system with a base pressure of better than 1×10^{-7} Torr. Same underlayers ($Cr_{90}Ru_{10}$(30 nm)\MgO(3.6 nm)) were used for all samples. Soft layer deposition temperature (T_{Soft}) included room temperature (RT), 200 °C, 300 °C, and 400 °C.

Compositions of the hard and soft layers are: $Fe_{50}Pt_{50}$ [hard], $(Fe_{50}Pt_{50})$-SiO_2(20 vol%) [soft]. CrRu and FePt layers were deposited by co-sputtering elemental targets. The $(Fe_{50}Pt_{50})$-SiO_2 layer was deposited by co-sputtering FePt alloy and SiO_2 targets.

Unless specified, all ECC FePt samples were cooled down to RT after the hard layer deposition and then re-heated for about 2 hours to elevated temperatures for the soft layer deposition. Annealing of the hard layer samples was conducted in the same sputtering system.

The structural and magnetic properties of samples were characterized by Cu source x-ray diffractometer (XRD), vibrating sample magnetometer (VSM), and transmission electron microscopy (TEM), respectively.

6.3 Structural and Magnetic Properties of ECC FePt Media

Fig. 6.1 (a) showed the out-of-plane magnetic hysteresis loops of the hard layer samples annealed at different temperatures in vacuum. The saturation magnetization (Ms) and the squareness remained the same if considering experimental errors, while the coercivity (Hc) increased slightly with the annealing temperature (RT → 200 ^oC → 400 ^oC: +5.8%, +9.4%, respectively). This might be due to improved ordering parameter of $L1_0$ FePt grains after annealing. Fig. 6.1 (b) showed the XRD spectra of the soft layer samples with different deposition temperatures. FePt (111) peak was the only FePt peak at the temperature of 200 ^oC and below, but it disappeared at 400 ^oC. FePt (001) peak (characteristic peak of $L1_0$ ordered FePt) was seen only at 400 ^oC. Both FePt (111) and (002) peaks were seen at 300 ^oC. It is clear that the texture of soft layer samples evolved gradually from FePt (111) to FePt (001) as the deposition temperature increased. It also suggested that the soft layer anisotropy might change its direction from in-plane to out-of-plane at 300 ^oC and above, when using the CrRu\MgO underlayers. Fig. 6.1 (c) and (d) showed the magnetic properties of the soft layer samples with different deposition temperatures. The soft layer anisotropy changed from in-plane (300 ^oC and below) to out-of-plane (400 ^oC), which is consistent with the XRD results. The Ms of soft layers

increased slightly from RT to 200°C (+7%), and then more rapidly at higher temperatures (+12%). These results confirmed the feasibility of controlling the soft layer anisotropy by changing its deposition temperature.

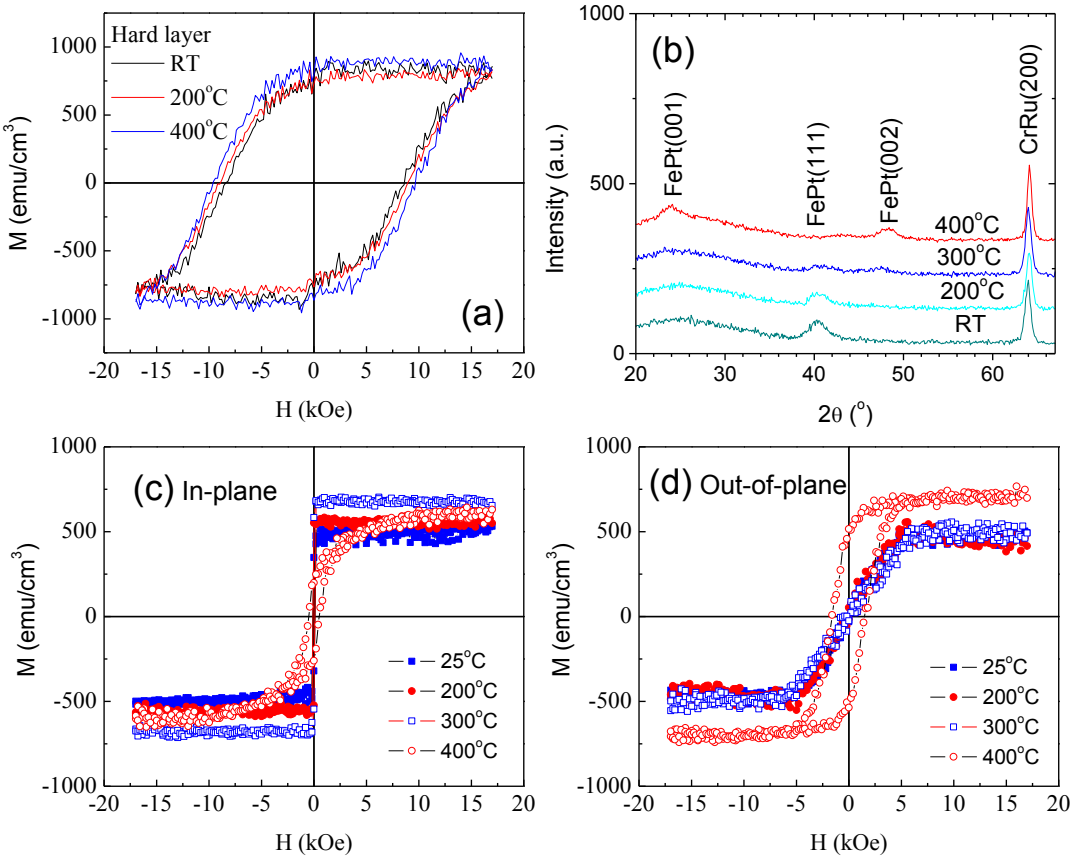

Figure 6.1 Structural and magnetic properties of the hard layer and soft layer samples: (a) Hysteresis loops of hard layer samples annealed at different temperature; (b) XRD spectra of the soft layer samples; (c) In-plane and (d) Out-of-plane loops of the soft layer samples.

Fig. 6.2 (a) showed the XRD spectra of the ECC FePt samples with different soft layer deposition temperatures. First, comparing to the soft layer samples' results, there was no FePt (111) peak for ECC FePt samples at all temperatures, which means that there could be an epitaxial growth relationship between the hard FePt layer and the soft FePt layer. Therefore, in our ECC FePt samples, the soft layer can be considered as the soft

region with perpendicular (out-of-plane) anisotropy in the ECC structure where the hard region also has perpendicular anisotropy. The effect of the change of easy axis direction in the soft layer can be ignored in our discussion. Secondly, it is seen that the overall FePt (001) texture of ECC FePt samples was improved as the soft layer deposition temperature increased, as evidenced by the peak intensity ratio of FePt (001)/(002). This is also a reasonable result due to thermodynamic considerations.

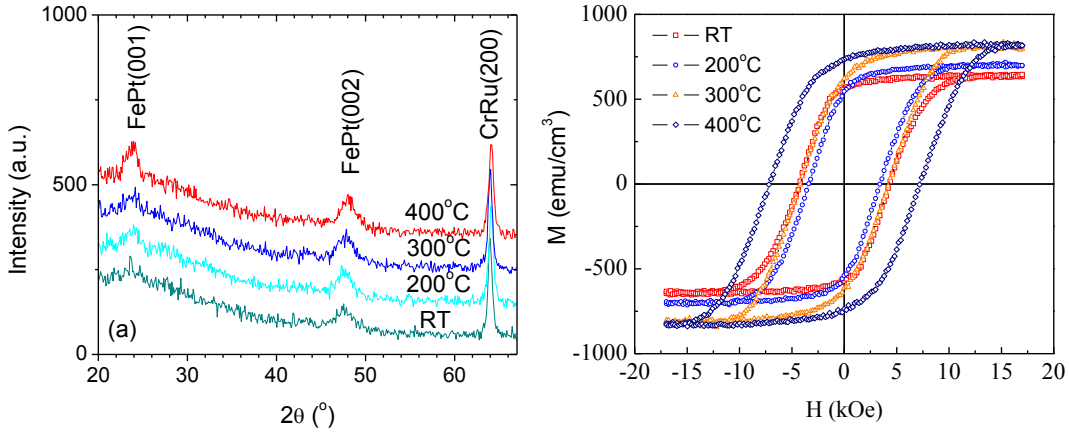

Figure 6.2 XRD spectra (a) and out-of-plane magnetic hysteresis loops (b) of the ECC FePt samples with different soft layer deposition temperatures.

The $\Delta\theta_{50}$ values of FePt (001) peak of the FePt hard layer sample and ECC FePt samples are given in Table 1. They are relatively large compared to current commercial perpendicular magnetic recording media (~ 3°). Except the sample with T_{Soft} at 25 °C, the difference of $\Delta\theta_{50}$ values between the FePt hard layer sample and ECC FePt samples is about 5 – 10%, which suggested that the FePt (001) texture of our ECC FePt thin films was mainly determined by the bottom FePt hard layer. Therefore, improvements on the (001) texture of FePt hard layer by optimizing deposition processes or using different underlayers can lead to better texture in ECC FePt media.

Fig. 6.2 (b) showed the out-of-plane magnetic hysteresis loops of the ECC FePt samples. The Ms of ECC FePt samples increased with the soft layer deposition temperature, up to 300 °C, and then showed not much change at 400 °C. The larger Ms of

FePt grains at higher temperature can be attributed to lower defect concentration (mostly Si and O), because the soft layer was prepared by co-sputtering FePt with SiO_2, and the exclusion of Si and O from FePt grains needs thermal energy, although this process is thermodynamically favorable. The most important result is that the coercivity (Hc) showed a minimum at the soft layer deposition temperature of 200 ^{o}C. The remanence coercivity (Hcr) also showed a minimum at 200 ^{o}C, as seen in Fig. 6.3. These results are consistent with the theoretic prediction (Robin et al. 2006 and Hagedorn et al. 1970) based on domain wall switching mechanism that the switching field will be reduced at first with a soft layer anisotropy when the soft layer anisotropy is low, and will increase again after passing a minimum when the soft layer anisotropy is high enough. This is a unique feature of the domain wall switching mechanism, which is not predicted by the two-layer approximation (Victora et al. 2005 and Robin et al. 2006). Therefore, there exists an optimum value of the soft layer anisotropy field in the two-layer ECC structured media. Domain wall assisted switching is indeed the dominant magnetization reversal mechanism in these ECC FePt samples. It also implied that these ECC FePt samples have the potential of achieving high gain factor (e.g. > 2).

Table 6.1 Summary of structural and magnetic properties of the FePt hard layer sample and ECC FePt thin film samples with different soft layer deposition temperature. Switching field distributions (D(Hs)) were obtained using the ΔH(M, ΔM) method (Berger et al. 2005).

	FePt hard layer	ECC FePt thin film with different soft layer deposition temperature			
		25 ℃	200 ℃	300 ℃	400 ℃
$\Delta\theta_{50}$ of FePt (001) (°)	10.58	13.27	11.19	11.18	11.61
Ms (emu/cm^3)	850	642	700	819	830
H_0 (Oe)	13542	6834	5459	5843	8678
Ku_e (10^6 erg/cm^3)	5.76	2.19	1.91	2.39	3.60
Hc (Oe)	8577	4298	3402	4254	7194
ΔH_{50} of D(Hs) (Oe)	7458	4175	3539	5274	6854
[ΔH_{50} of D(Hs)]/Hc	87%	97%	104%	124%	95%

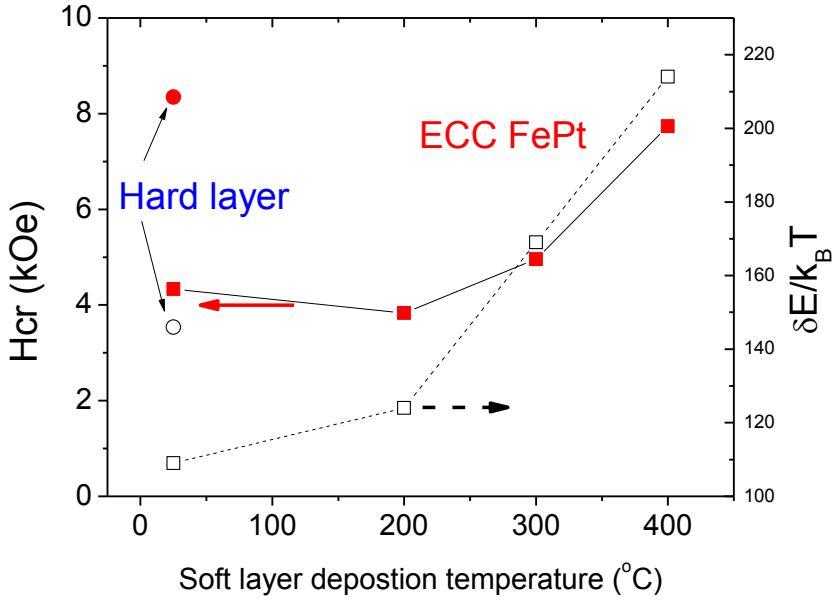

Figure 6.3 The effect of soft layer deposition temperature on the remanence coercivity (solid symbols) and thermal stability factor (hollow symbols) of the ECC FePt samples.

Fig. 6.3 also showed the effect of soft layer deposition temperature on the thermal stability factor of the ECC FePt samples. The thermal stability factors were obtained from thermal decay measurements on VSM, and by fitting the dynamic coercivity vs. decay time using the Shamrock equation (Sharrock et al. 1999). The parameters used in the fitting are: $f_0 = 10^{10}$ (Hz), $\gamma = 1.5$. Compared to the thermal stability factor of the hard layer sample, the ECC FePt sample at RT showed a much lower thermal stability factor. This is because the magnetization reversal mechanism changed from coherent switching in the hard layer sample to ECC switching (soft layer assisted switching) in the ECC FePt samples. It is also seen that the thermal stability factor of ECC FePt samples increased monotonically with the soft layer deposition temperature. This is consistent with the XRD results that showed better FePt (001) texture at higher soft layer deposition temperature. Therefore, the magnetic harder soft layer at higher deposition temperature should contribute partially to the higher thermal stability factor of the ECC FePt samples. Another possibility is grain growth in the hard layer of ECC FePt samples when the

substrate temperature was ramping up and during the deposition of the soft layer. The grain growth effect will be much more significant at higher temperatures (e.g. 300 ^{o}C and 400 ^{o}C). With the experimental values of Ms and fitting results of the switching fields with the discount of thermal decay effect (H_0), an equivalent anisotropy constant (Ku_e) for ECC media can be estimated as $Ku_e = (Ms \times H_0)/2$, and the calculated results are listed in Table 1. It is not a surprise to see that the ECC FePt with T_{Soft} at 200 ^{o}C showed the lowest Ku_e.

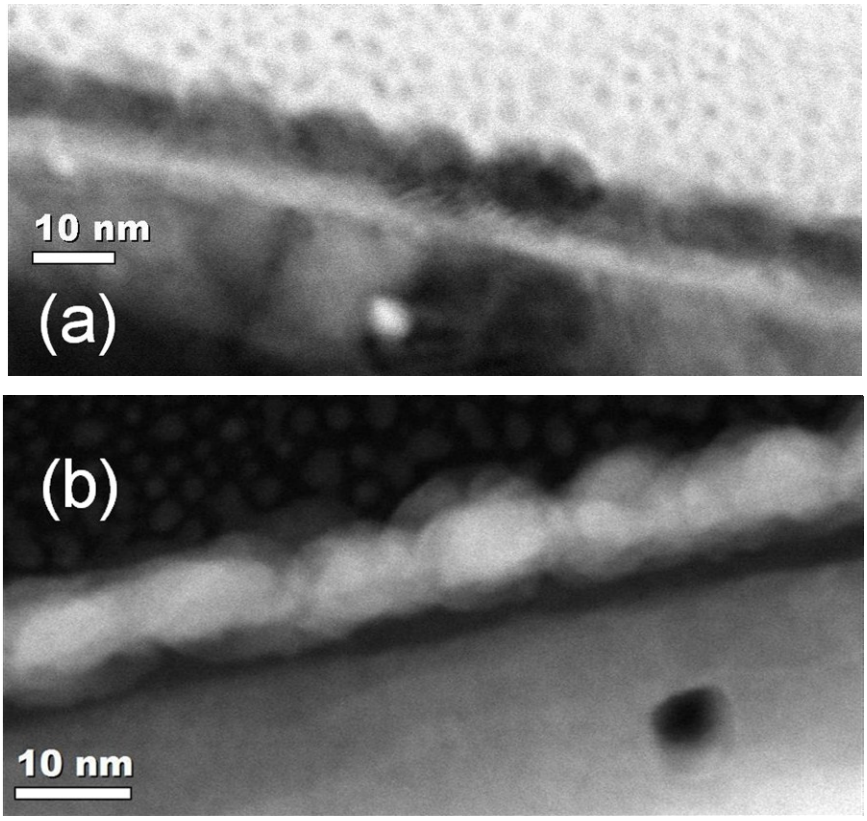

Figure 6.4 TEM micrographs of the ECC FePt sample with the soft layer deposition temperature of 200 ^{o}C. (a) bright field image, (b) high angle annular dark field (HAADF) image.

Fig. 6.4 showed the TEM cross-sectional micrographs of the microstructure of ECC FePt sample with the soft layer deposition temperature of 200 ^{o}C. Both the bright field (BF) image and high angle annular dark field (HAADF) image showed that FePt grains

with curved surfaces were closely packed. The average height of FePt grains is about 8 nm, which is slightly larger than the nominal film thickness (7 nm). Besides the experimental errors such as calibrations of sputter deposition rates, this difference of film thickness might also be due to the curved grain surfaces. Based on the curved grain surfaces in the BF image and the core regions with brighter Z-contrast in the DF image, the average grain diameter is estimated to be about 13 nm, which is comparable to the grain size (14 nm) of FePt of similar film thickness grown on MgO single crystalline substrate (Ma et al. 2010). No clear/wide grain boundaries consisting of SiO_2 can be identified. Therefore, the exchange coupling between FePt grains might not be small. To achieve better inter-grain exchange de-coupling, more SiO_2 doping in the soft layer will be needed.

If we assume the average magnetic switching volume is the average grain volume, i.e. ignoring the inter-grain exchange coupling, we can calculate the gain factor of the ECC FePt sample (200 ^oC) (Victora et al. 2005). Using the following parameters obtained in our experiments: Ms – 700 emu/cm^3, Hcr – 3830 Oe, and $\Delta E/K_bT$ – 124, and assuming the average grain volume of 1150 nm^3, the gain factor is estimated to be 3.3, which is larger than 2, the maximum value under two-layer approximation of ECC switching (Victora et al. 2005). However, due to inter-grain exchange coupling, the average magnetic switching volume might be much larger than the average grain volume, so the actual gain factor for this ECC FePt sample could be much smaller.

Fig. 6.5 showed the switching field distributions (D(Hs)) of the FePt hard layer and ECC FePt thin films. The D(Hs) values were determined by the $\Delta H(M, \Delta M)$ method (Berger et al. 2005). ECC FePt samples generally showed smaller Full Width at Half Maximum (FWHM, or ΔH_{50}) of D(Hs) than FePt hard layer sample. But the $\Delta H_{50}/Hc$ ratio is much larger for ECC FePt samples with intermediate T_{Soft} (200 ^oC and 300 ^oC). The D(Hs) curve of ECC FePt with T_{Soft} at 200 ^oC showed visible asymmetry with a bigger high-end tail that could contribute most the overwrite value of recording media and the overall reliability of multiple recording (Berger et al. 2005). The reason for the

increased ΔH_{50}/Hc ratio and the D(Hs) asymmetry is not clear and worth of further investigation.

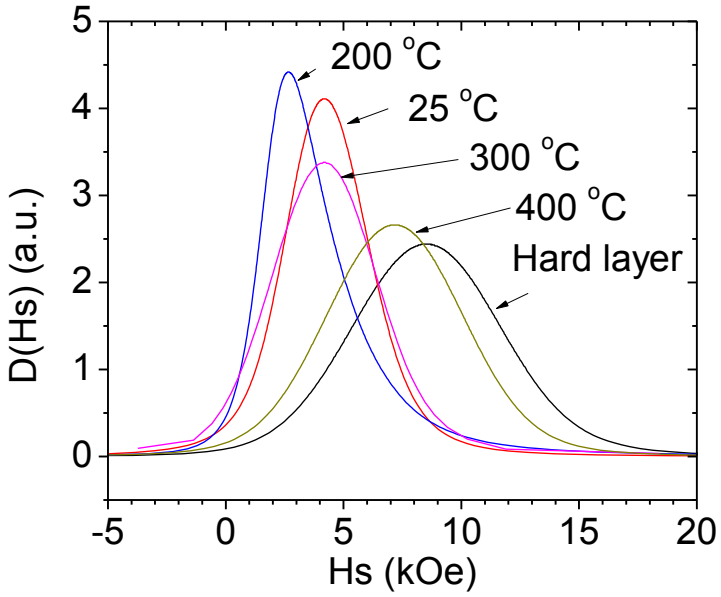

Figure 6.5 The switching field distributions (D(Hs)) of the FePt hard layer and ECC FePt thin films with different soft layer deposition temperatures (labeled next to each curve), obtained by using the ΔH(M, ΔM) method.

6.4 **Conclusion**

Ultra-thin ECC FePt granular recording media with different soft layer anisotropy were fabricated by controlling the soft layer deposition temperature. TEM analysis confirmed the total FePt film thickness is about 8 nm, close to the nominal thickness of 7 nm. It was found that magnetic properties of the magnetically hard layer (FePt 3 nm) remained relatively stable under annealing up to 400 °C, 2 h in vacuum. The structural and magnetic properties of soft layers (FePt-SiO_2) confirmed the feasibility of controlling the soft layer anisotropy by changing its deposition temperature. As the soft layer (FePt-SiO_2) deposition temperature increased, the overall FePt (001) texture of ECC FePt thin films was improved, while the saturation magnetization (Ms) and the thermal stability factor were also increased. The effect of soft layer anisotropy field on the coercivity (Hc)

and the remanent coercivity (Hcr) of ECC FePt thin films showed a "V" shape relationship, with the minimums at T_{Soft} of 200 ^{o}C. These results are consistent with the theoretic prediction based on domain wall assisted magnetization reversal mechanism. The ECC FePt thin film with T_{Soft} of 200^{o}C may have a gain factor larger than 2.

Chapter 7. **Conclusions and Suggestions to Future Work**

7.1 **Conclusions**

In this thesis work, the two most-promising candidates of high Ku materials, i.e. $CaCu_5$-type $Sm(Co, Cu)_5$ and $L1_0$-type FePt thin films, have been systematically studied for their potential application as magnetic recording media.

Polycrystalline Sm–Co–Cu films consisting mainly of highly (0001) textured $CaCu_5$-type $Sm(Co, Cu)_5$ grains have been fabricated successfully on highly (0002) textured and smooth Ru or Ru(Cr) underlayers which were grown on glass substrates with a Ta seed layer. Strong perpendicular magnetic anisotropy of $Sm(Co, Cu)_5$ thin films was achieved, such as the out-of-plane coercivity of 11 kOe, the nearly zero in-plane coercivity, the squareness ratio of 1. The estimated perpendicular magnetic anisotropy constants of $3.3\sim5.8 \times 10^7$ erg/cm^3 are consistent with that of bulk $Sm(Co, Cu)_5$ material with a similar composition. It was found that increasing Cu is like increasing deposition temperature - both could improve the $SmCo_5$ phase formation and the crystallinity of $Sm(Co, Cu)_5$ (0001) films. The thickness dependence of coercivities of Sm-Co-Cu films showed a maximum at 10 nm, which can be explained by combining the effects of the formation of misoriented grains in thicker films and more defects in thinner films, such as the magnetic dead layer formed at the interface between Sm–Co–Cu layer and Ru underlayer. The median composition of nanocrystalline $Sm(Co, Cu)_5$ grains estimated from structural unit volume and Curie temperature matches reasonably well with each other. Instead of tensile strain, in-plane compressive strain in $Sm(Co, Cu)_5$ grains is inferred from the differences of lattice constants (*a* and *c*) between $Sm(Co, Cu)_5$ films and bulk $Sm(Co, Cu)_5$. The use of Ru(Cr) underlayer with a proper Cr doping could improve the perpendicular anisotropy of $Sm(Co, Cu)_5$ films. But it is not clear if this improvement is due to a slight strain in grains or the pinning effect of Cr atoms in grain boundaries.

Chapter 7. Conclusions and outlook

Magnetization reversal is dominated by domain wall pinning mechanism as revealed by the shape of initial magnetization curves and the angular dependence of remanence coercivity. Through the analyses of SEM, AFM, and TEM, various types of pinning sites in highly (0001) textured $Sm(Co, Cu)_5$ thin films have been identified. The major pinning type that could substantially affect the *Hc* is the composition gradient of Cu in the $Sm(Co, Cu)_5$ layer. TEM elemental mapping analysis showed that Cu atoms were rich in the inner part of $Sm(Co, Cu)_5$ grains or particles, instead of the outer part, such as grain boundaries or edges of voids. Cu served as an alloying element in $Sm(Co, Cu)_5$ grains, not as a doping element to form Cu-rich grain boundaries. Since the Cu concentration inside a $Sm(Co, Cu)_5$ grain is closely related to the crystallinity of that grain, which in turn determines its magnetic anisotropy, Cu composition variations will lead to magnetic anisotropy variations. A model of $Sm(Co, Cu)_5$ films with in-plane graded anisotropy due to composition/crystallization variations is proposed to explain the huge difference between the *Hc* and H_K, as well as the angular dependence of remanence coercivity of $Sm(Co, Cu)_5$ thin films. A simple analytical expression of the angular dependence of switching field for anisotropy graded media has been derived and shown to match well with experimental results in $Sm(Co, Cu)_5$ thin films.

Chemical stability of $Sm(Co, Cu)_5$ thin films has been studied. $Sm(Co, Cu)_5$ thin films without a capping layer showed fast degradation under normal conditions (1 atm, 25°C, < 50% humidity). $Sm(Co, Cu)_5$ thin films with a nominal 3 nm Ta capping layer but grown on high-process-pressure Ru underlayer also showed relatively fast degradation. Only those $Sm(Co, Cu)_5$ thin films with a nominal 3 nm Ta capping layer that were grown on a smooth Ru underlayer are stable under normal conditions in terms of magnetic and microstructural properties. However, no $Sm(Co, Cu)_5$ thin films can pass the accelerated corrosion test, which was designed for qualifying hard disk recording media in HDD applications. A capping layer structure consisting of a hcp-phased CoPt-alloy layer and a carbon overcoat should help $Sm(Co, Cu)_5$ thin films meet the requirements for future high-density magnetic recording applications.

$L1_0$-type FePt thin films were studied as perpendicular ECC media with potentially high gain factor due to domain-wall assisted magnetic switching. Ultra-thin ECC FePt granular recording media with different soft layer anisotropy were fabricated by controlling the soft layer deposition temperature. TEM analysis confirmed the total FePt film thickness is about 8 nm, close to the nominal thickness of 7 nm. It was found that magnetic properties of the magnetically hard layer (FePt 3 nm) remained relatively stable under annealing up to 400 ^{o}C, 2 h in vacuum. The structural and magnetic properties of soft layers (FePt-SiO2) confirmed the feasibility of controlling the soft layer anisotropy by changing its deposition temperature. As the soft layer (FePt-SiO_2) deposition temperature increased, the overall FePt (001) texture of ECC FePt thin films was improved, while the saturation magnetization (*Ms*) and the thermal stability factor were also increased. The effect of soft layer anisotropy field on the coercivity (*Hc*) and the remanent coercivity (*Hcr*) of ECC FePt thin films showed a "V" shape relationship, with the minimums at T_{Soft} of 200 ^{o}C. These results are consistent with the theoretical prediction based on domain wall assisted magnetization reversal mechanism. The ECC FePt thin film with T_{Soft} of 200 ^{o}C may have a gain factor larger than 2.

7.2 Suggestions to Future Work

7.2.1 $Sm(Co, Cu)_5$ thin film media

A. New underlayers for the $Sm(Co, Cu)_5$ (0001) thin films

Lattice constants (*a* and *c*) of $Sm(Co, Cu)_5$ thin films on Ru (0002) underlayer are different from those of bulk $Sm(Co, Cu)_5$ with the same composition: smaller *a* and larger *c* are seen in films. This difference can be explained by the heteroepitaxial relationship between Sm-Co sub-layer of $Sm(Co, Cu)_5$ (0001) and Ru (0002) underlayer, instead of that between Co-Co sub-layer of $Sm(Co, Cu)_5$ (0001) and Ru (0002). It could also be the reason that we saw poorer magnetic properties of $Sm(Co, Cu)_5$ thin films on Ru(Cr) underlayers than Ru underlayer. Following the above understanding, we might see better magnetic properties of $Sm(Co, Cu)_5$ thin films on new underlayers with similar

surface structure as the Ru underlayer but also with a slightly larger atom-to-atom distance (*a*-*a*) in the film plane. Re and Pt underlayer might be good candidates because their *a*-*a* values are 0.276 and 0.2774 nm, respectively, which are slightly larger than that of Ru (0.2706 nm). Re has another potential advantage over Ru: higher melting point (3186 ºC for Re, and 2330 °C for Ru), which implies smaller grain size in Re underlayer than Ru underlayer at same deposition/annealing temperature. Prior studies on Pt underlayer (Morisako et al. 2006b and Takahashi et al. 2006) failed to grow $SmCo_5$ thin films with perpendicular anisotropy. It is mostly probably because their Pt underlayer did not have a good (111) texture since no proper seed layer was employed in their studies. It is expected that highly (0001) textured $Sm(Co, Cu)_5$ thin films can be grown on Ta\Re or Ta\Pt underlayers at a substrate temperature of ~400 °C.

B. Better crystallization and homogeneity of the $Sm(Co, Cu)_5$ (0001) thin films

As seen in previous discussions, even in the highly (0001) textured $Sm(Co, Cu)_5$ thin films grown on Ta\Ru (0002) underlayer, there are amorphous matrix and regions with inhomogeneous composition. Optimizing the sputtering parameters, such as deposition pressure (lower) and temperature (higher), should help improve the crystallization. Using a composite target of Sm-Co-Cu instead of co-sputtering of three elemental targets may help with the homogeneity. Additionally, biasing sputtering may be combined to improve the film quality.

C. Magnetic cluster control for conventional magnetic recording

For the magnetic cluster control, the general requirements are small and uniform grain size of magnetic grains, which are largely exchanged-decoupled, and with a narrow distribution of perpendicular anisotropy. The key is to find a proper material, which can segregate from $Sm(Co, Cu)_5$ phase during co-sputtering with the main elements (Sm, Co, and Cu) to form non-magnetic boundaries. A natural candidate could be Zr, which has been widely used in Sm-Co magnets and is known to form a boundary phase. Common oxides (such as SiO_2, Ta_2O_5, etc.) may have adverse effect on the magnetic properties of

Sm-Co thin films, as reported by Sugiyama et al. (2010), probably due to the large enthalpy of formation of Samarium oxide (Sm_2O_3). In this sense, the Sm_2O_3 itself may be considered as the boundary material. Doping boundary materials may affect the crystallization of main $Sm(Co, Cu)_5$ phase. Therefore, proper deposition parameters for each boundary material may be different.

D. Anti-corrosion control

In principle, there are two means that can help improve the corrosion resistance of $SmCo_5$-based thin film media, without increasing the magnetic spacing between the recording head and recording media. One is to use a magnetic overcoat which has a stronger intrinsic corrosion resistance, such as CoCrPt-based materials used in current perpendicular recording media. An intermediate Pt may be used between the $Sm(Co, Cu)_5$ layer and the CoCrPt layer to promote epitaxial growth.

Another way is to improve the intrinsic corrosion resistance of $SmCo_5$ by doping with the proper element(s), which would not adversely affect the anisotropy constant, or at least would not cause too much of the decrease of the anisotropy constant. A potential candidate is Ni, because $Sm(Co, Ni)_5$ is known to have comparable anisotropy field as $Sm(Co, Cu)_5$ for the same amount of Ni or Cu doping, both at cryogenic temperature (e.g. Foner et al. 1978 and Oesterreicher 1978) and room temperature (Pratos and Hadjipanayis 1999). Ni is known to have excellent corrosion resistance in most environments. So the corrosion resistance of $Sm(Co, Ni)_5$ is expected to be better than that of $Sm(Co, Cu)_5$. How much improvement that $Sm(Co, Ni)_5$ can provide should be verified. Note that $Sm(Co, Ni)_5$ or Ni may be considered as the magnetic overcoat as well. Another candidate is Cr, as it is being used in current CoCrPt-based perpendicular media for better corrosion resistance. Cr has been used as the capping layer of Sm-Co thin films in many studies. The Cr underlayer had been shown to grow $SmCo_5$ thin films with large in-plane coercivity and anisotropy (e.g. Fullerton et al. 1997 and Zhang et al. 2009). In addition, as discussed in Chapter 3, proper Cr doping in Ru underlayer led to larger switching field in the $Sm(Co, Cu)_5$ (0001) films, which implies that it may reduce the

exchange-coupling between $Sm(Co, Cu)_5$ grains. Proper doping of Cr into $Sm(Co, Cu)_5$ thin films may have little impact on magnetization and anisotropy, but a large improvement in corrosion resistance and exchange-decoupling of the magnetic films.

7.2.2 The site preference of Cu doping in $Sm(Co, Cu)_5$ (0001) thin films

Single-crystalline $SmCo_4Cu$ and $SmCo_3Cu_2$ thin films grown on Ru buffered Al_2O_3 (0001) substrate should be good samples to revisit the investigation of site preference of Cu doping in $Sm(Co, Cu)_5$ (0001) thin films by the extended x-ray absorption fine structure (EXAFS) spectroscopy.

7.2.3 Ultra-thin ECC FePt granular recording media with large gain factor

The gain factor of our ultra-thin ECC FePt is estimated to be 3.3, which is larger than 2, the maximum value under two-layer approximation of ECC switching. However, due to inter-grain exchange coupling, the average magnetic switching volume might be much larger than the average grain volume, so the actual gain factor for this ECC FePt sample could be much smaller. A well exchange-decoupled FePt hard layer is needed to confirm the benefit in our design of ultra-thin ECC FePt. It can be achieved by doping Ag and C into the FePt hard layer at slightly higher deposition temperature.

Bibliography

Asahi, T., I. Koizumi, Y. Kikuchi, M. Yoshino, A. Sugiyama, J. Hokkyo, and T. Osaka, *J. Magn. Magn. Mater.* **320,** 3075 (2008).

Baibich, M. N., A. Fert, et al., Phys. Rev. Lett. 61, 2472 - 2475 (1988).

Berger, A., et al., IEEE Trans. Magn., 41, 3178 (2005).

Binasch, G., P. Grünberg, et al., Phys. Rev. B 39, 4828 - 4830 (1989).

Bodak, O., and Fabrichnaya, *Cobalt-Copper-Samarium*, SpringerMaterials, The Landolt-Bornstein Database, New Series IV/11C2, 2007. (Materials Science International Team MSIT®, and Bodak, Oksana, Fabrichnaya, Olga: Co-Cu-Sm (Cobalt-Copper-Samarium). Effenberg, G., Ilyenko, S. (ed.). (http://www.springermaterials.com). DOI: 10.1007/978-3-540-47000-7_15).

Burzo, E., A. Chelkowski, and H. R. Kirchmayr, (1990) Landolt-Bornstein New Series Group III, vol 19d2, ed. O Madelung (Berlin: Springer) table 38c on p 86.

Buschow, K. H. J., and A. S. Van der Goot, *Acta Cryst. B* **27**, 1085 (1971).

Cataldo, L., A. Lefevre, F. Ducret, M. -Th. Cohen-Adad, C. Allibert, and N. Valignat, *J. Alloys Comp*., **241**, 216 (1996).

Chen, J. S., L. N. Zhang, J. F. Hu, and J. Ding, *J. Appl. Phys.* **104**, 093905 (2008).

Chen, J. S., et al., Appl. Phys. Lett. 90, 042508 (2007).

Chen, K., H. Hegde, S. U. Jen, and F. J. Cadieu, *J. Appl. Phys.* **73,** 5923 (1993).

Cheng, W., S. Zhao, X. Cheng, and X. Miao, *J. Supercond. Nov. Magn.* **25**, 1947 (2012a).

Cheng, W., W. Liu, X. Wang, Y. Dai, X. Cheng, and X. Miao, *J. Magn. Magn. Mater.* **324,** 3658 (2012b).

Cheng, W., Y. Dai, H. Hu, X. Cheng, and X. Miao, *J. Electron. Mater.* 41, 2178 (2012c).

Cromer, D. T., and A. C. Larsson, *Acta Cryst.* **12**, 855-859 (1959).

de Campos, M. F., and F. J. G. Landgraf, *J. Phase Equilib.* **21**(5), 443-446 (2000).

E. Lectard, C. H. Allibert, and R. Ballou, J. Appl. Phys., vol. 75, p. 6277, 1994.

Foner, S., E. J. McNiff Jr., H. Oesterreicher, F. T. Parker, and M. Misroch, *J. Appl. Phys.* **49**, 2061 (1978).

Frerichs, R., *J. Appl. Phys.* **33**, 1898 (1962).

Fullerton, E. E., J. S. Jiang, C. Rehm, C. H. Sowers, S. D. Bader, J. B. Patel, and X. Z. Wu, *Appl. Phys. Lett.* **71**, 1579 (1997).

Gabay, A. M., P. Larson, I. I. Mazin, and G. C. Hadjipanayis, *J. Phys. D: Appl. Phys.* **38,** 1337 (2005).

Bibliography

Ge, W. Q., C. H. Wu, and Y. C. Chuang, *Z. Metallkd.* **84**, 165-169 (1993).

Hagedorn, F. B., J. Appl. Phys. 41, 2491 (1970).

Hofer, F., *IEEE Trans. Magn.* **6**, 221 (1970).

Hummler, K., and M. Fähnle, *Phys. Rev. B* **53**, 3272 (1996).

K. Hayashi et al., *J. Phys. Soc. Jpn.*, vol. 73, no. 9, pp. 2550–2553 (2004).

Kamino, K., Y. Kimura, T. Suzuki, Y. Itayama, *Trans. Jpn. Inst. Met.* **14**, 135 (1973).

Katayama, T., T. Shibata, *Jpn. J. Appl. Phys.* **12**, 319 (1973).

Kato, I., S. Takei, X. Liu, and A. Morisako, *IEEE Trans Magn.* **42**, 2366 (2006).

Kawaji, J., T. Osaka, J. Sayama, and A. Sugiyama, *International Symposium on Physics of Magnetic Materials (ISPMM)* (2005), Singapore, Presentation 3E-2, "Creation of High Bs and High Ku Materials for Ultra High Density Magnetic Recording".

Khan, Y., *Acta Crystallogr. B* **30**, 861-864 (1974a).

Khan, Y., *Phys. Status Solidi A* **23**, 425–434 (1974b).

Khmelevskyi, S., and P. Mohn, *J. Phys.: Condens. Matter* **12**, 9453–9464 (2000).

Kirchmayr, H. R., and E. Burzo,: 2.4.1.1 General. Wijn, H.P.J. (ed.). SpringerMaterials - The Landolt-Bornstein Database (http://www.springermaterials.com). DOI: 10.1007/10333633_1.

Kronmüller, H., and D. Goll, *Physica B: Condensed Matter* **319**, 122 (2002).

Kullmann, U., E. Koester, and C. Dorsch, *IEEE Trans. Magn*., **20**, 420 (1984).

Kumar, K., *J. Appl. Phys.* **63**, R13 (1988).

Larson, P., I. I. Mazin, and D. A. Papaconstantopoulos, *Phys. Rev. B* **67**, 214405 (2003).

Lectard, E., C. H. Allibert, and R. Ballou, *J. Appl. Phys.* **75**, 6277 (1994).

Li, Y., J. Shen, and Y. Chen, *Solid State Sci.* **12**, 33 (2010).

Liu, X. H., L. Y. Cui, S. X. Zhou, C. Y. Wang, B. Y. Quan, L. J. Wang, W. Zheng, A. L. Wang, and J. C. Chen, *Materials Science and Engineering A* **304–306**, 1043–1045 (2001).

Liu, X., H. Zhao, Y. Kubota, J. P. Wang, *IEEE Trans Magn.* **44,** 3550 (2008a).

Liu, X., H. Zhao, Y. Kubota, J. P. Wang, *J. Phys. D: Appl. Phys.* **41,** 232002 (2008b).

Liu, Y., B. W. Robertson, Z. S. Shan, S. Malhotra, M. J. Yu, S. K. Renukunta, S. H. Liou, and D. J. Sellmyer, *IEEE Trans. Magn.* **30**, 4035 (1994).

Ma, B., et al., IEEE Trans. Magn. 46, 2345 (2010).

Maissel, L. I., and P. M. Schaible, *J. Appl. Phys.* **36**, 237 (1965).

Malhotra, S. S., Y. Liu, Z. S. Shan, S. H. Liou, D. C. Stafford, and D. J. Sellmyer, *J. Appl. Phys.* **79**, 5958 (1996).

Meyer-Llautaud, F., S. Derkaoui, C. H. Allibert, R. Castanet, *J. Less-Common Met.* **127**, 231 (1987).

Miyazaki, T., and N. Tezuka, J. Magn. Magn. Mater. 139, L231–234 (1995).

Bibliography

Momma, K., and F. Izumi, "VESTA 3 for three-dimensional visualization of crystal, volumetric and morphology data," *J. Appl. Crystallogr.*, **44**, 1272-1276 (2011).

Moodera, J. S., et al., Phys. Rev. Lett. 74, 3273 - 3276 (1995).

Moreau, J. -M., and D. Paccard, *Acta Crystallogr. B* **32**, 1654-1657, (1976).

Morisako, A., and X. Liu, *J. Magn. Magn. Mater.* **304,** 46 (2006a).

Morisako, A., I. Kato, S. Takei, and X. Liu, *J. Magn. Magn. Mater.* **303,** e274 (2006b).

Neu, V., J. Thomas, S. Fähler, B. Holzapfel, L. and Schultz, *J. Magn. Magn. Mater.* **242–245,** 1290 (2002).

Nukaga, Y., M. Ohtake, F. Kirino, and M. Futamoto, *IEEE Trans Magn.* **44**, 2891 (2008).

Oesterreicher, H., *Appl. Phys.* **15**, 341 (1978).

Ohring, M., *The Materials Science of Thin Films*, Academic, New York, 1992.

Ohtake, M., Y. Nukaga, F. Kirino, and M. Futamoto, *J. Appl. Phys.* **105**, 07C315 (2009b).

Ohtake, M., Y. Nukaga, F. Kirino, and M. Futamoto, *J. Appl. Phys.* **107**, 09A706 (2010).

Ohtake, M., Y. Nukaga, F. Kirino, and M. Futamoto, *J. Cryst. Growth* **311**, 2251 (2009a).

Okamoto, H., *J. Phase Equilib.* **19**, 183 (1998).

Okamoto, H., *J. Phase Equilib. Diffus.* **32**(2), 165-166 (2011).

Okumura, Y., H. Fujimori, O. Suzuki, N. Hosoya, X. B.Yang, and H. Morita, *IEEE Trans Magn.* **30**, 4038 (1994).

Osaka, T., Y. Yamashita, J. Sayama, T. Asahi, J. Ariake, K. Harada, and K. Ouchi, *IEEE Trans Magn.* **43**, 2109 (2007).

Perry, A. J., *J. Less-Common Met.* **51**, 153 (1977).

Petrov, I., L. Hultman, U. Helmersson, J. E. Sundgren, and J. E. Greene, *Thin Solid Films* **169**, 299 (1989).

Prados, C., and G. C. Hadjipanayis, *Appl. Phys. Lett.* **74**, 430 (1999).

Prados, C., and G. C. Hadjipanayis, *J. Appl. Phys.* **83**, 6253 (1998).

Richter, M., P. M. Oppeneer, H. Eschrig, and B. Johansson, *Phys. Rev. B* **46**, 13919 (1992).

Robin, A., et al., Appl. Phys. Lett. 89, 062512 (2006).

Rossnagel, S. M., J. J. Cuomo, and W. D. Westwood, *Handbook of Plasma Processing Technology*, Noyes, New York, 1990.

Sabirianov, R. F., A. Kashyap, R. Skomski, S. S. Jaswal, and D. J. Sellmyer, *Appl. Phys. Lett.* **85**, 2286 (2004).

Sato, K. , I. Umeharaa, N. Fujimoria, M. Hamanoa, K. Nakanoa, T. Fukuharab, and K. Maezawab, *Physica B* **199-200**, 651 (1994).

Sayama, J., K. Mizutani, T. Asahi, and T. Osaka, *Appl. Phys. Lett.* **85**, 5640 (2004b).

Bibliography

Sayama, J., K. Mizutani, T. Asahi, J. Ariake, K. Ouchi, and T. Osaka, *J. Magn. Magn. Mater.* **301**, 271 (2006a).

Sayama, J., K. Mizutani, T. Asahi, J. Ariake, K. Ouchi, S. Matsunuma, and T. Osaka, *J. Magn. Magn. Mater.* **287**, 239 (2005a).

Sayama, J., K. Mizutani, Y. Yamashita, T. Asahi, and T. Osaka, *IEEE Trans Magn.* **41**, 3133 (2005b).

Sayama, J., T. Asahi, and T. Osaka, *J. Magn. Soc. Jpn.* **30**, 662 (2006c).

Sayama, J., T. Asahi, K. Mizutani, and T. Osaka, *J. Phys. D: Appl. Phys.* **37**, L1 (2004a).

Sayama, J., T. Asahi, Y. Yamashita, J. Ariake, K. Ouchi, and T. Osaka, *J. Magn. Soc. Jpn.* **30**, 423 (2006b).

Scientific Group Thermodata Europe (SGTE), and Franke, P., Neuschütz, D.: Co-Cu. Franke, P., Neuschütz, D. (ed.). SpringerMaterials - The Landolt-Börnstein Database (http://www.springermaterials.com). DOI: 10.1007/10757405_65

Seifert, M., V. Neu, and L. Schultz, *Appl. Phys. Lett.* **94**, 022501 (2009).

Sharrock, M. P., IEEE Trans. Magn., 35, 4414(1999).

Shen, W. K., Ph.D. Dissertation, University of Minnesota (2006).

Shi, J. Z. S. N. Piramanayagam, C. S. Mah, H. B. Zhao, J. M. Zhao, and Y. S. Kay, *Appl. Phys. Lett.* **87**, 222503 (2005).

Shi, J., D. Kojima, and M. Hashimoto, *J. Appl. Phys.* **88**, 1679 (2000).

Steinbeck, L., M. Richter, and H. Eschrig, *J. Magn. Magn. Mater.* **226-230**, 1011 (2001).

Strnat, K. J., Ferromagnetic Materials, edited by E. P. Wohlfarth and K. H. J. Buschow, Eds. Amsterdam, The Netherlands: North-Holland, 1988, vol. 4, ch. 2, pp. 131–209.

Suess, D., et al., *Appl. Phys. Lett.* **92**, 173111, (2008).

Sugiyama, A., I. Koizumi, Y. Egawa, M. Yoshino, J. Hokkyo, T. Asahi, and T. Osaka, *IEEE Trans Magn.* **46,** 1699 (2010).

Sun, C. J., H. Zhao, S. M. Heald, X. Liu, H. Wang, and J. P. Wang, 55th MMM Conference, CE-15, unpublished manuscript, (2010).

Takahashi, Y. K., T. Ohkubo, and K. Hono, *J. Appl. Phys*. **100** 053913 (2006).

Takei, S., A. Morisako, and M. Matsumoto, *J. Magn. Magn. Mater.* **272-276**, 1703 (2004).

Takei, S., S. Shomura, A. Morisako, M. Matsumoto, and T. Haeiwa, *J. Appl. Phys.* **81**, 4674 (1997).

Téllez-Blanco, J. C., R. Grossinger, R. Sato Turtelli, *J. Alloys. Compd.* **281**, 1 (1998).

Tsai, J. L., M. Y. Chen, G. B. Lin, and C. L. Ou, *Thin Solid Films* **517**, 4942 (2009).

Velu, E. M. T., and D. N. Lambeth, *IEEE Trans. Magn.* **28**, 3249 (1992).

Verhagen, T. G. A., Ph.D. Dissertation, Leiden University (2014).

Bibliography

Victora, R. H., and X. Shen, *IEEE Trans. Magn.* **41**, 537 (2005).

Victora, R. H., J. Xue, and M. Patwari, *IEEE Trans. Magn.*, **38**, 1886 (2002).

W. Si et al., *J. Appl. Phys.*, vol. 97, p. 10N901, (2005).

Wang, H., Ph.D. Dissertation, the University of Minnesota (2013).

Wang, J. P., et al., IEEE Trans. Magn. 41, 3181 (2005a).

Wang, J. P., et al., IEEE Trans. Magn. 43, 682 (2007).

Wang, J. P., W. K. Shen, J. M. Bai, R. H. Victora, J. H. Judy, W. L. Song, *Appl. Phys. Lett.* **86**, 142504 (2005b).

Wang, J. Y., M. K. Ghantasala, and R. J. Mclean, *Thin Solid Films* **517**, 656 (2008).

Weller, D., et al., IEEE Trans. Magn. 36, 10 (2000).

Xu, Y., et al., *J. Nanosci. Nanotechno*. **7**, 206-224 (2007).

Yin, S., H. Wang, H. Zhao, Y. Jiang, J. P. Wang, *J. Appl. Phys.* **114**, 213908 (2013).

Yuan, Y., J. Yi, G. Borzone, and A. Watson, *CALPHAD* **35**, 416 (2011).

Yuan, Y., S. Delsante, J. Yi, and G. Borzone, *J. Alloys Compd.* **508**, 309-314 (2010).

Zana, I., and G. Zangari, *J. Vac. Sci. Technol. A* **19**, 1203 (2001).

Zhang, L. N., J. F. Hu, J. S. Chen, and J. Ding, *J. Appl. Phys.* **105**, 07A743 (2009a).

Zhang, L. N., J. F. Hu, J. S. Chen, and J. Ding, *Proc. of SPIE* **7125**, 71250M-1 (2009b).

Zhang, L. N., J. S. Chen, J. Ding, and J. F. Hu, *J. Appl. Phys.* **103**, 113908 (2008).

Zhang, W. Y., X. D. Zhang, Y. C. Yang, and B. G. Shen, *J. Alloy. Compd.***353**, 274 (2003).

Zhao, H., H. Wang, and J.P. Wang, *J. Appl. Phys.* **111**, 07B730 (2012).

Zhao, H., H. Wang, X. Liu, T. Zhang, and J.P. Wang, *J. Appl. Phys.* **109**, 07B715 (2011).

Zhao, Z. L., et al., Appl. Phys. Lett. 88,052503(2006).

Conference presentations

H. Zhao, H. Wang, and J. P. Wang, "*A General Method to Fabricate Exchange Coupled Composite Media with Graded Structure for Energy Assisted Magnetic Recording*". Intermag 2008 Conference, ED-09, Madrid, Spain, 2008.

H. Zhao, X. Liu, H. Wang, and J. P. Wang, "*Exchange Coupled Composite (ECC) Media with an $L1_0$ FePt Hard Layer*". 52nd Annual Conference on Magnetism & magnetic Materials, FC-05, Tampa, USA, 2007.

W. Shen, H. Zhao, and J. P. Wang, "*Design and Optimization of Soft and Hard Regions of Exchange Coupled Composite Grains for Future ECC Media*". 10th Joint MMM/Intermag Conference, AB-02, Baltimore, USA, 2007.

H. Wang, **H. Zhao**, T. Rahman, Y. Isowaki, Y. Kamata, T. Maeda, H. Hieda and A. Kikitsu, H.-H. Guo, B. Ma, Y. Chen, W. Li, J. Ding, and J. P. Wang, "*Fabrication and Characterization of FePt Exchange Coupled Composite and Graded Bit Patterned Media*", 23rd The Magnetic Recording Conference(TMRC), F-6 (invited), San Jose, 2012.

H. Wang, W. Li, T. Rahman, **H. Zhao**, J. Ding, Y. Chen, and J. P. Wang, "*Characterization of $L1_0$-FePt based exchange coupled composite bit pattern media*". 56th Annual Conference on Magnetism & magnetic Materials, DQ-08, Scottsdale, USA, 2011.

H. Wang, T. Rahman, **H. Zhao**, Y. Isowaki, Y. Kamata, A. Kikitsu, and J. P Wang, "*Fabrication of FePt Type Exchange Coupled Composite Bit Patterned Media by Block-copolymer Lithography*". 55th Annual Conference on Magnetism & magnetic Materials, AR-13, Atlanta, USA, 2010.

Conference presentations

H. Wang, **H. Zhao**, A. Das, M. Racine, M. Imakawa, and J. P. Wang, "*A Nature Method to Fabricate Exchange Coupled Composite Media*", 53rd Annual Conference on Magnetism & magnetic Materials, CC-09, Austin, USA, 2008.

J. P. Wang, H. Wang and **H. Zhao**, "*FePt type exchange coupled composite media and multi-level recording*", 19th Magnetic Recording Conference(TMRC), BB-3 (invited), Singapore, 2008

Patent

J. P. Wang, H. Wang, **H. Zhao**, “Embedded mask patterning process for fabricating magnetic media or other structures," U.S. Appln. No. 61/691,681

Publications

H. Zhao, H. Wang, X. Liu, T. Zhang, and J.P. Wang, "Chemical Stability of Highly (0001) Textured Sm(Co, Cu)$_5$ Thin Films with a Thin Ta Capping Layer", J. Appl. Phys. **109**, 07B715 (2011).

H. Zhao, H. Wang, and J.P. Wang, "Microstructure Study of Pinning Sites of Highly (0001) Textured Sm(Co, Cu)$_5$ Thin Films Grown on Ru Underlayer", J. Appl. Phys., **111**, 07B730 (2012).

H. Zhao, H. Wang, and J.P. Wang, "Fabrication of Ultra Thin $L1_0$-FePt Based Exchange Coupled Composite Media", J. Appl. Phys. **111**, 07B732 (2012).

H. Zhao, and J.P. Wang, "Review of Studies on $SmCo_5$-Based Thin Films for Magnetic Recording Media Applications", J. Phys. D: Appl. Phys., to be submitted.

H. Zhao, and J.P. Wang, "Magnetization Reversal of Highly (0001) Textured Sm(Co, Cu)$_5$ Thin Films Grown on Ru Underlayer", in preparation.

X. Liu, **H. Zhao**, Y. Kubota, J. P. Wang, "Film Composition, Substrate Temperature, and Thickness Dependence of Sm(Co, Cu)$_5$/Ru Thin Films With Perpendicular Anisotropy", IEEE trans. Magn. **44**, 3550 (2008).

X. Liu, **H. Zhao**, Y. Kubota, J. P. Wang, "Polycrystalline Sm(Co, Cu)$_5$ films with perpendicular anisotropy grown on (0002) Ru(Cr)", J. Phys. D: Appl. Phys. **41**, 232002 (2008).

H. Wang, **H. Zhao**, P. Quarterman, and J. P. Wang, "Embedded Mask Patterning: A Nanopatterning Process to Fabricate FePt Magnetic Media", Appl. Phys. Lett. **102**, 052406 (2013).

H. Wang, **H. Zhao**, O. Ugurlu, and J.P. Wang, "Spontaneously-formed FePt graded granular media with a large gain factor", IEEE Magn. Lett. **3**, 450014 (2012).

H. Wang, **H. Zhao**, T. Rahman, Y. Isowaki, Y. Kamata, T. Maeda, H. Hieda and A. Kikitsu, and J. P. Wang, *"Fabrication and Characterization of FePt Exchange Coupled*

Publications

Composite and Graded Bit Patterned Media", (invited), *IEEE trans. Magn.* **49**, 707 (2013).

H. Wang, T. Rahman, **H. Zhao**, Y. Isowaki, Y. Kamata, A. Kikitsu, and J.P. Wang, "Fabrication of FePt Type Exchange Coupled Composite Bit Patterned Media by Block-copolymer Lithography", J. Appl. Phys. **109**, 07B754 (2011).

S. Yin, H. Wang, **H. Zhao**, Y. Jiang, J. P. Wang, "The effects of Cu doping on crystalline structure and magnetic properties of SmCo5-xCux thin films grown on Ru (0002)", J. Appl. Phys. **114**, 213908 (2013).

B. Ma, H. Wang, **H. Zhao**, C. Sun, R. Acharya, and J.P. Wang, "$L1_0$ FePt/Fe Exchange Coupled Composite Structure on MgO Substrates", IEEE Trans. Magn. **46**, 2345 (2010).

B. Ma, H. Wang, **H. Zhao**, C. Sun, R. Acharya, and J.P. Wang, "Structural and magnetic properties of a core-shell type $L1_0$ FePt/Fe exchange coupled nanocomposite with tilted easy axis", J. Appl. Phys. **109**, 083907 (2011).

H. Wang, W. Li, T. Rahman, **H. Zhao**, J. Ding, Y. Chen, and J.P. Wang, "*Characterization of $L1_0$-FePt based exchange coupled composite bit pattern media*", *J. Appl. Phys.*, **111**, 07B914 (2012).